# Leading Neutron Physics at HERA using the Forward Neutron Detector at ZEUS

by

Thorsten Koop

A thesis submitted in conformity with the requirements
for the degree of Doctor of Philosophy
Graduate Department of Physics
University of Toronto

# Abstract

Leading neutrons produced in high energy electron-proton collisions at a center-of-momentum energy of 318 GeV$^2$ are studied with the Forward Neutron Detector of the ZEUS experiment at the HERA collider. The Forward Neutron Detector consists of the Forward Neutron Calorimeter and the newly implemented Forward Neutron Tracker. The detectors and their calibration are presented. The transverse momentum squared, $p_T^2$, distributions of leading neutrons in bins of $x_L$, the fraction of the proton energy carried by the neutron, have been measured using the Forward Neutron Tracker. The measurements were made using data samples in deep inelastic scattering and photoproduction, corresponding to integrated luminosities of 21 pb$^{-1}$ and 9.3 pb$^{-1}$, respectively. The distributions are fitted with an exponential, and the slopes are presented as a function of $x_L$. The results are compared to models of one pion exchange and to leading proton measurements. The $x_L$ distributions of the photoproduced neutrons are measured for different bins of $t$, the invariant momentum transfer squared. The $(1 - x_L)$ distributions satisfy a power law $dN/dx_L \propto (1 - x_L)^{a(t)}$ with the powers $a(t)$ lying on a linear trajectory in $t$: $a(t) = 1.08 \pm 0.08^{+0.40}_{-0.42} - (2.78 \pm 0.32^{+0.31}_{-0.41}$ GeV$^{-2})t$. This result is consistent with that expected from pion exchange and with previous measurements. The neutron energy distributions are compared for different values of momentum transfer squared between the electron and the proton and the results are discussed in the context of models of absorption.

# Dedication

***For Claudia Koop.***

# Acknowledgements

The years I worked in the ZEUS collaboration were a wonderful experience for me.

My special thanks goes to my supervisor Dr. John F. Martin whose steady support, knowledge and humor made my work so much easier. I am very grateful to Dr. David Bailey and Dr. Mike Luke for their support and help.

I thank Dr. Garry Levman for his help, friendship and so many fruitful conversations throughout our work. My thank goes to Dr. Bill Schmidke, his friendship always made it a pleasure to work together with him. Thank you. I thank Dr. Sampa Bhadra for her encouragement, support and help.

Dr. Mauricio Barbi and Dr. Mara Senghi-Soares, your friendship and support made my life cheerful and happy. Thank you very much.

It was a pleasure to work together with so many talented student/postdocs and fabulous characters like Michael Riveline, Raphael Galea, Peter Fagerstroem, Mohsen Khazad, Ali Sabetfahkri, Jeff Standage, Cui Ying, Andreas Ochs, Sanjay Spadhi, Jerome Whyte, Marc St. Laurent, Dr. Corinna Catterall, Dr. Gerd Hartner and Dr. Alessandro Bertolin. I thank all my fellow students at University of Toronto, with whome I spend so many great moments. Special thanks goes to Ian Vollrath, Stan Lai, Simon Sabik, Bernd Stelzer, Oliver Stelzer, Kalen Martens, Shabnaz Pashapour, Jean-Francois Arguin, Pascal Vaudrevange, Johannes Martin, Tim Chan and Amit Ghosh. To those people I have forgotten, or not mentioned individually by name, I apologize.

I am deeply grateful to my mother, my family and to Cathy who brought so much joy into my life.

Finally I am deeply grateful to my late wife Claudia. I dedicate this thesis to her.

## Contributions to the ZEUS Experiment

My work on the ZEUS experiment at DESY started in 1998 as a member of the Forward Neutron Calorimeter (FNC) group. I was involved in the design of the Forward Neutron Tracker (FNT) in order to improve the position measuring capability of the FNC. I built the FNT and successfully installed it in the spring of 1998. I also performed a radiation damage study on scintillators taken out of the FNC to make room for the FNT.

In 1999 I became involved in the construction of the ZEUS Straw Tube Tracker. I assisted in building and testing parts of this new forward tracking detector, which was installed in ZEUS in 2001.

I participated and assisted in a meeting of the ZEUS collaboration in Toronto in June, 2000. I was involved in the design and management of the meeting web page. Since the year 2000 I assisted in the system administration of the Canadian PC cluster at DESY. I implemented the Forward Neutron Tracker into the GEANT Monte Carlo detector simulation of ZEUS and was the FNC Monte Carlo representative. As such I was responsible for modifying and testing the software.

From 1998 to 1999 I was on shift as safety officer for the ZEUS data taking. Since 2000 I was involved in the ZEUS data taking as deputy shift leader.

My physics focus has been the analysis of forward neutron data. I calibrated the FNC and FNT for the run years 1998 to 2000. This calibration is used by the entire ZEUS collaboration. Results of my analysis were presented at the $31^{st}$ International Conference on High Energy Physics 2003 and the $11^{th}$ International Workshop on Deep Inelastic Scattering 2002. I represented ZEUS at the International Europhysics Conference on High Energy Physics 2003 and presented an invited talk entitled "*Open Charm Contribution to $F_2^{D(3)}$ in DIS and Leading Baryon Production at HERA*". Currently three papers for publication based on results in this thesis are making their way through the ZEUS editorial process.

# Contents

# List of Tables

# List of Figures

# Chapter 1

# Introduction

Scattering experiments give the possibility of examining the structure of matter and, in particular, of nucleons. A probing particle is scattered off a target and the energy and angular distributions are measured. The size of an object that can be resolved in scattering experiments is determined by the momentum transferred from the probe to the target. To probe smaller objects a higher momentum transfer is needed. Experiments which can probe to much smaller distances than the size of the target are called deep inelastic scattering experiments.

The structure of the nucleon is directly accessible in leptoproduction experiments, in which the probing particle is a lepton, either an electron or neutrino. In contrast to the nucleon, mesons like the pion are poorly understood, since it is difficult to make a pion target. The pion can, however, be probed in "leading neutron" production at HERA [1], [2], [3], where a proton exchanges a pion with the probing electron, giving rise to a neutron at close to zero degrees with respect to the proton direction. This production mechanism of leading neutrons is not completely understood. It is of interest because it gives insight into the short and long distance structure of hadrons, specifically the proton, and therefore provides information on the relationship between the "soft" (low momentum transfer from the proton to the neutron) and "hard" (high momentum transfer from the electron probe) aspects of the strong interaction. It can give insight into the correlation between the quarks themselves and not only the measured single quark momentum densities. The long range structure of

hadrons remains a puzzle of quantum chromodynamics (QCD), the microscopic theory of the strong interaction, and is closely related to the problem of the transition from perturbative to non-perturbative physics. A non-perturbative approach to the strong interaction, such as Regge theory, is needed to calculate the production rate of leading neutrons. This thesis provides needed input to theories like Regge theory and QCD, which cannot yet predict the structure of hadrons and mesons satisfactory and cannot yet explain the production mechanism of leading neutrons completely .

Leading neutrons have been measured with the ZEUS experiment at the electron-proton collider HERA using a calorimeter installed at zero degrees in the HERA tunnel some 100 m from the $ep$ interaction point. In 1992 a first version of the Forward Neutron Calorimeter (FNC), a small test calorimeter, proved the feasibility of measuring leading neutrons. Using the test FNC, a first study of leading neutrons in photoproduction at a center-of-mass energy of 180 GeV was performed [4], [5]. The one pion exchange (OPE) model was found to be consistent with the data, in agreement with previous hadroproduction experiments [6].

Data taken in 1995 with the much improved final FNC were used to measure the cross section for photoproduction with two jets of high transverse momentum and a leading neutron in the final state [7], [8]. A major study of leading neutrons in deep inelastic scattering was undertaken using data taken from 1995 to 1997 [9], [10]. The angular dependence of leading neutrons was determined with large errors and the differential cross section relative to the inclusive process $ep \to eX$ in deep inelastic scattering was measured. Under the assumption of a simple OPE model, the pion structure function was extracted.

In 1998 the FNC was upgraded by installing the Forward Neutron Tracker (FNT). The FNT greatly improved the position resolution of the detector. Furthermore, a new photoproduction trigger allowed the simultaneous data taking of deep inelastic scattering and photoproduction events.

In this thesis, the production of leading neutrons by scattering positrons (or elec-

trons) off protons is studied using data taken from 1998 to 2000 with the FNC and FNT. Chapter 2 is devoted to the ZEUS detector components which were needed to perform the data taking and analysis reported here. In Chapter 3 the improved forward neutron detector is presented and its calibration and performance are described. Chapter 4 gives a brief outline of the underlying theory and explains the basic kinematic concepts. A review of the methods used for reconstruction of the kinematic variables is given in Chapter 5. The data samples which are analyzed are described in Chapter 6, as well as the methods of event selection. Chapter 7 describes the alignment and finding of the center point of the neutron distribution. Chapter 8 describes the systematic uncertainties. The angular distributions of neutrons in photoproduction, deep inelastic scattering and photoproduced dijet events are studied in Chapter 9. The angular distributions are fitted using an exponential parameterization and compared to theoretical predictions. Chapter 10 analyses the data in the frame work of Regge theory and provides further evidence for the dominance of pion exchange in the neutron production mechanism. In Chapter 11, a measurement of absorptive effects in leading neutron production is presented. Chapter 12 is a summary.

# Chapter 2

# The HERA Accelerator and the ZEUS Detector

## 2.1 Accelerators at DESY

The Hadron Electron Ring Anlage (HERA) (Fig. 2.1) is the world's only electron-proton collider. HERA is located at the Deutsches Elektronen Synchrotron, DESY, Hamburg, Germany. The HERA tunnel has a circumference of 6.3 km and is located 10 m to 25 m below the surface. The configuration of the facility is shown in Fig. 2.2.


Figure 2.1: Aerial view of the HERA site at DESY in Hamburg, Germany. The accelerators PETRA (the injector for HERA) and HERA are marked by dashed lines.

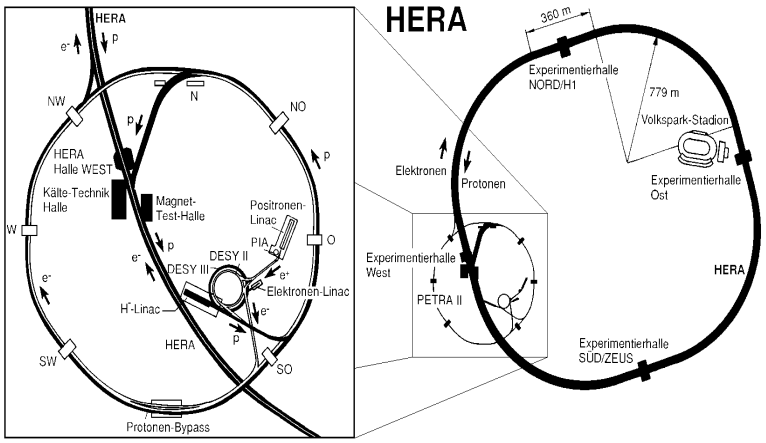


Figure 2.2: The accelerators used for HERA at DESY. The four experiments ZEUS (South hall), HERA-B (West hall), H1 (North hall) and HERMES (EAST hall) are indicated.

Protons are accelerated in two smaller rings, DESY II to 7.5 GeV, and PETRA to 40 GeV, before injection into HERA. Three injections of 70 bunches are needed to fill HERA, which has 220 radio frequency buckets separated by 96 ns. The protons are accelerated to 920 GeV in HERA.

Electrons or positrons are accelerated to 500 MeV in a linear accelerator, LINAC II. They are then cooled in a storage ring, PIA, and segmented into a bunch structure. In the DESY II ring they are accelerated to 7 GeV, in PETRA to 14 GeV and finally in HERA to 27.5 GeV. The collisions of electrons or positrons of 27.5 GeV and protons of 920 GeV result in a center-of-momentum energy of 317 GeV. Fig. 2.3 shows the integrated luminosity since the start of HERA in 1992. From 1994 to 1997 the HERA proton energy was 820 GeV. Since 1998 the proton energy has been 920 GeV. The data used in this thesis were taken during the run periods in the years 1998 to 2000. The total integrated luminosity in this period was $125\,\mathrm{pb}^{-1}$.

## 2.2 The ZEUS Detector at HERA

At HERA, there are two halls for colliding electrons or positrons and protons, the north hall (H1 experiment) and the south hall (ZEUS experiment). The data used in

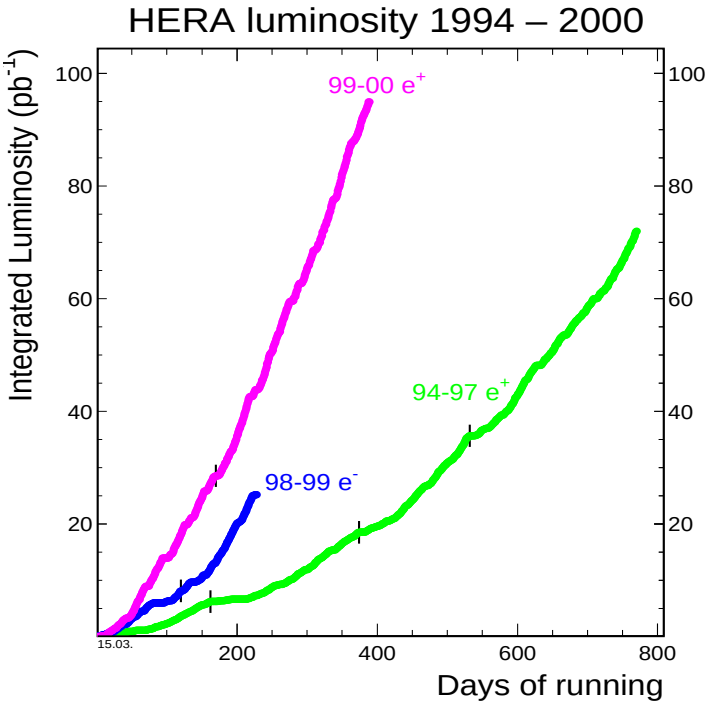


Figure 2.3: Integrated luminosity delivered by HERA 1994-2000. From 1994 to 1997 the final energy of the protons was 820 GeV. Since 1998 the proton energy has been 920 GeV.

this thesis were collected using the ZEUS detector.

The ZEUS detector is a multi-purpose detector which allows the study of final state particles produced by $ep$ collisions. It is an asymmetrical detector, to account for the momentum imbalance between the colliding beams. A detailed description of the ZEUS detector can be found in the technical status reports [11] and subsequent status reports [12]. Throughout this thesis, the ZEUS coordinate system is used (Fig.

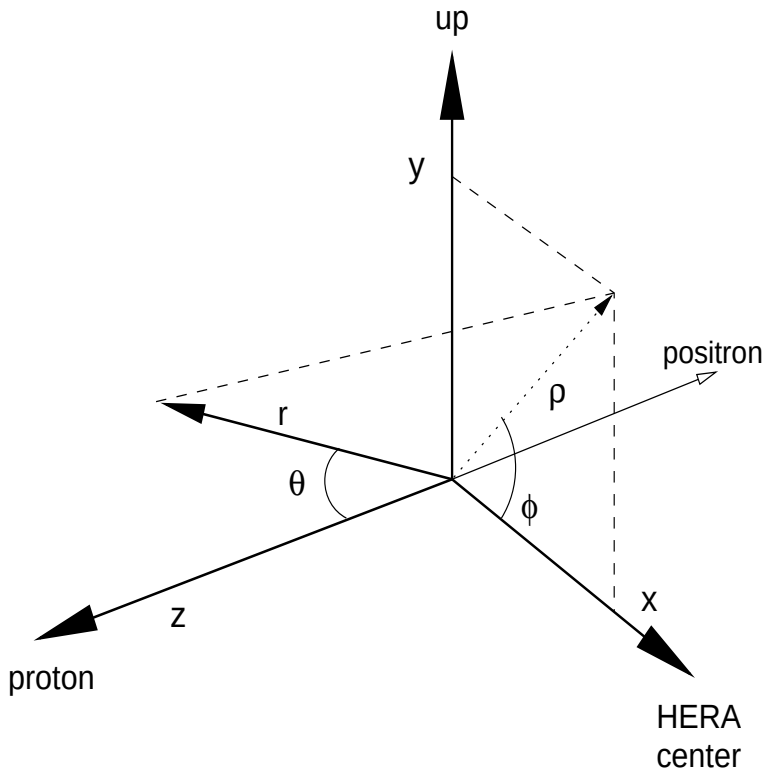


Figure 2.4: The ZEUS coordinate system.

2.4). The $z$ axis points along the so-called forward direction, the direction of the proton beam. The direction of the positron beam defines the rear direction. The $x$ axis points towards the center of the HERA ring, the $y$ axis points up. The nominal interaction point is at $(x, y, z) = (0, 0, 0)$. The polar angle is measured with respect to the positive $z$ axis and the azimuthal angle relative to the positive $x$ axis. Thus, the polar angles of the proton and electron beam are 0 and 180 degrees, respectively.

The detector components which are essential for this analysis are described in the following sections.

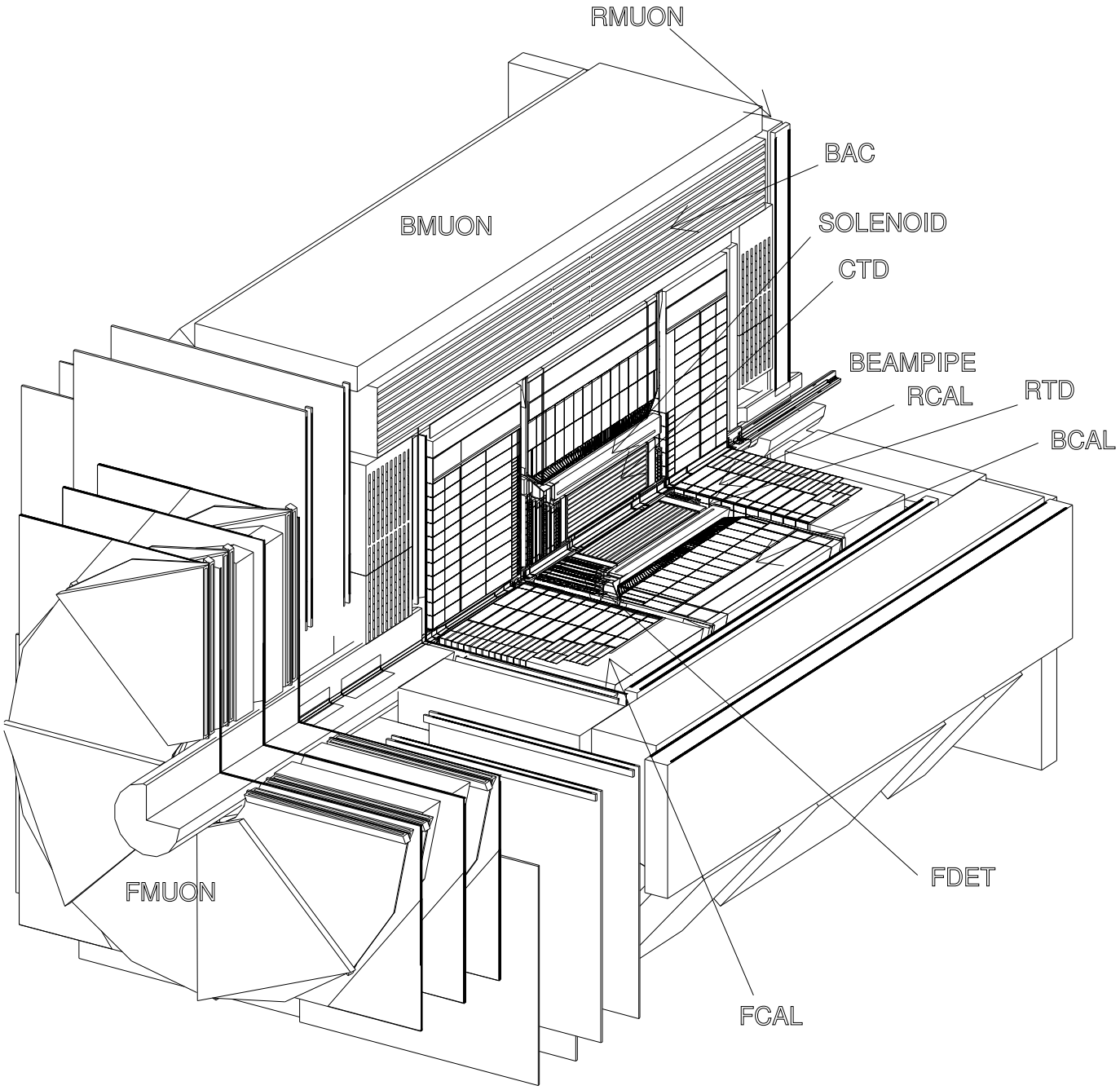


Figure 2.5: Cut away view of the ZEUS detector.

### 2.2.1 The Central Tracking Detector

The Central Tracking Detector (CTD) ([13],[14],[15]) is located inside a superconducting solenoid, which provides a uniform magnetic field of 1.93 T. It is a cylindrical drift chamber providing momentum and direction information of charged particles, and also energy loss ($dE/dx$) information to help identify particles. The CTD has an inner radius of 18.2 cm, an outer radius of 79.4 cm and a length of 205 cm. Radially, the CTD is subdivided into 9 superlayers as seen in Fig. 2.6. Odd numbered superlayers have sense wires parallel to the CTD axis. Even numbered superlayers are stereo layers with wires inclined by $\pm 5^{o}$ to the chamber axis. The transverse momentum resolution is $\sigma(p_t)/p_t = 0.0058p_t \oplus 0.0065 \oplus 0.0014/p_t$ ($p_t$ in GeV), where $\oplus$ means taken in quadrature [16].

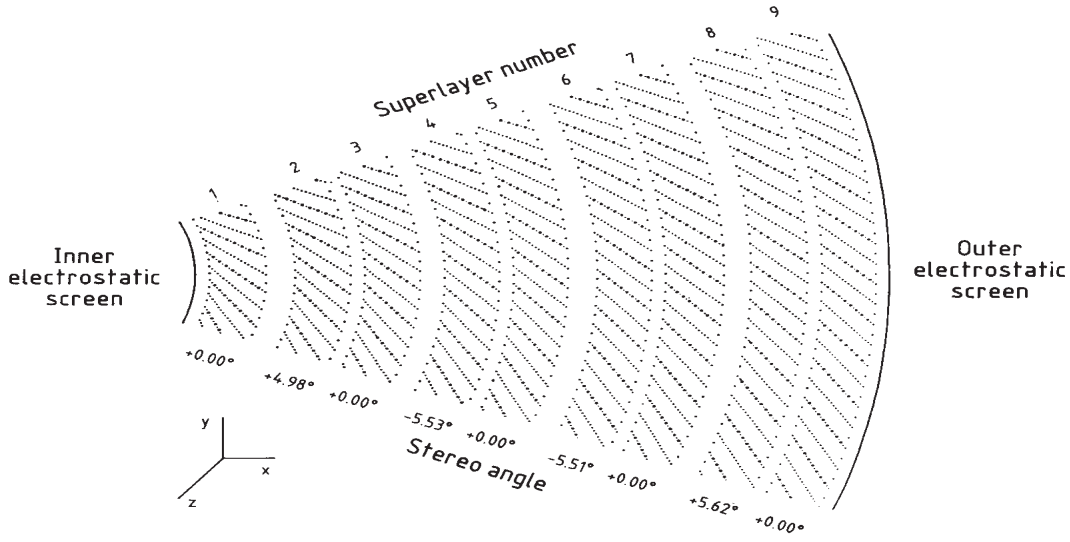


Figure 2.6: View of the ZEUS CTD superlayers.

### 2.2.2 Uranium Calorimeter

A calorimeter measures the total energy deposited by incident particles. The absorbed energy is transformed into a measurable signal, which is proportional to the energy of the incident particle. An incident particle interacts with the materials in the calorimeter, producing secondary particles. These secondary particles interact in turn, causing the development of a particle shower. There are two types of showers,

electromagnetic showers and hadronic showers.

Electromagnetic showers are induced by an incident $e^-$, $e^+$ on $\gamma$. Electromagnetic showers at energies higher than 1 GeV are dominated by bremsstrahlung and pair production. Bremsstrahlung is the radiation of a photon $\gamma$ by an electron or a positron in the presence of the nuclear electric field. Pair production is the production of an electron and a positron by a photon with enough energy in the nuclear electric field. An electromagnetic shower is characterized by its radiation length, $X_0$, which is material dependent. $X_0$ is the mean distance over which a high energy electron loses 1/e of the initial energy by bremsstrahlung. This energy loss is given by

$$(\frac{dE}{dx})_{Bremsstrahlung} \approx -\frac{E}{X_0}, \tag{2.1}$$

where $x$ is the thickness of the material and $E$ the energy of the electron. A material thickness of 20 radiation lengths is enough to contain more than 99% of the electromagnetic shower. The characteristic length of electromagnetic showers is smaller than that of hadronic showers.

Incident hadrons undergo electromagnetic and nuclear interactions. Hadronic showers are made up of a large variety of processes. Secondary particles are produced in inelastic collisions with nuclei. The main contributions to hadronic shower development are the production of charged hadrons. The charged hadrons lose energy by ionization until a new strong interaction occurs. Neutral hadrons are also produced, which can interact strongly. Neutrinos are produced, which escape undetected by the calorimeter. Photons are produced as well, from the decay of neutral pions. The photons give rise to electromagnetic showers within the hadronic shower. Furthermore, the excited nuclei produced can either release lower energy photons or nucleons or undergo fission. A hadronic shower can be characterized by the nuclear absorption length, $\lambda$, which is the mean free path before a particle interacts inelastically,

$$\lambda = \frac{A}{\rho N_A \sigma_i}, \tag{2.2}$$

.

where A is the mass number of the absorber, $\rho$ the density of the material, $N_A$ is Avogadro's number and $\sigma_i$ is the inelastic cross section [17].

A homogeneous calorimeter is build entirely of an active (signal producing) medium. This type of calorimeter is a solution at low particle energies and for purely electromagnetic showers. As particle energies increase, the size of the calorimeter necessary to contain the hadronic shower becomes more and more uneconomical in a totally active calorimeter. A solution to this problem is the sampling calorimeter. A sampling calorimeter is composed of layers of active material which alternate with layers of a dense absorber. The active materials measure the energy flow as a function of depth.

The active and absorbing materials and their thicknesses can be chosen to achieve an electron/hadron ($e/h$) signal response ratio close to unity, which is the definition of a compensating calorimeter, in which the average energy lost to binding energy and neutrinos is compensated by other processes. A compensating calorimeter has the best possible hadronic energy resolution.

The most important detector component in ZEUS to reconstruct $ep$ scattering events is a high resolution uranium calorimeter (UCAL). The UCAL is a sampling calorimeter [18], [19], [20]. It is made of depleted uranium (the absorber material) and scintillator (the active material) in a sandwich structure. The thickness of the plates of uranium and scintillator has been chosen to achieve compensation ($e/h = 1.00 \pm 0.03$) for a wide energy range. The energy resolution is $\sigma(E)/E = 0.35/\sqrt{E(\mathrm{GeV})}$ for hadrons and $\sigma(E)/E = 0.18/\sqrt{E(\mathrm{GeV})}$ for electrons/positrons, as determined under test beam conditions.

The UCAL has three segments, the rear (RCAL), barrel (BCAL) and forward (FCAL) calorimeter, where forward is in the proton beam direction. The RCAL covers a polar angle region of $128.1^\circ < \theta < 176.9^\circ$, the BCAL a region of $36.7^\circ < \theta < 129.1^\circ$ and the FCAL a region of $2.2^\circ < \theta < 39.9^\circ$. FCAL and RCAL are each segmented into 24 vertical modules. Each FCAL module is subdivided into $20 \times 20$ cm$^2$ towers. The towers contain an electromagnetic (EMC) and two hadronic (HAC) sections. Each

hadronic section of a tower is called a calorimeter cell. The EMC section has a subdivision into four $20 \times 5$ cm$^2$ cells. RCAL has only one hadronic section and the cell size of the EMC is $20 \times 10$ cm$^2$. BCAL has 22 wedge-shaped modules with two HAC sections and one EMC section. The wedges are tilted 2.5° in $\Phi$ with respect to a radial line from the interaction point in the $x - y-$plane. It has 14 towers along the $z$ axis.

The calorimeter cells are read out by photomultiplier tubes (PMTs) on opposite sides which are coupled to the scintillators via wavelength shifters. The energy calibration of the calorimeter was originally done in a test beam, and is followed in time on a channel-by-channel basis using the radioactive decay of $^{238}$U, which provides a stable and time independent reference signal. This calibration tracking is good to 1%. The PMT light efficiency and linearity is checked periodically using LED and laser light. Radiation damage to the scintillator near the beam is checked once a year using $^{60}$Co sources along the sides of the calorimeter modules. The electronic readout is calibrated via charge injection test pulses. The calorimeter time resolution is better than 1 nsec for energy deposits above 4.5 GeV.

### 2.2.3 The Luminosity Monitor

In order to measure cross sections, an accurate measurement of the time integrated luminosity is crucial. At HERA, $ep$ luminosity is measured using the rate of hard bremsstrahlung photons from the Bethe-Heitler process $ep \to ep\gamma$ [21]. This process has a high cross section and is theoretically understood to an accuracy of 0.5%. The luminosity monitor (LUMI) consists of two calorimeters, an electron calorimeter (LUMI-e) and a photon calorimeter (LUMI-$\gamma$)[22], as seen in Fig. 2.7. LUMI-e is a lead scintillator calorimeter, located at $z$ = –35 m. It measures small angle ($\Theta$ < 4 mrad) scattered electrons, which are deflected from the nominal orbit by the HERA magnets, whose energy is in the range of $(0.2 - 0.8)E_{Beam}$. LUMI-$\gamma$ is a lead-scintillator calorimeter as well. It is located at $z$ = –104 m in the HERA tunnel. A 3.5 $X_0$ carbon/lead filter protects LUMI-$\gamma$ against synchrotron radiation.

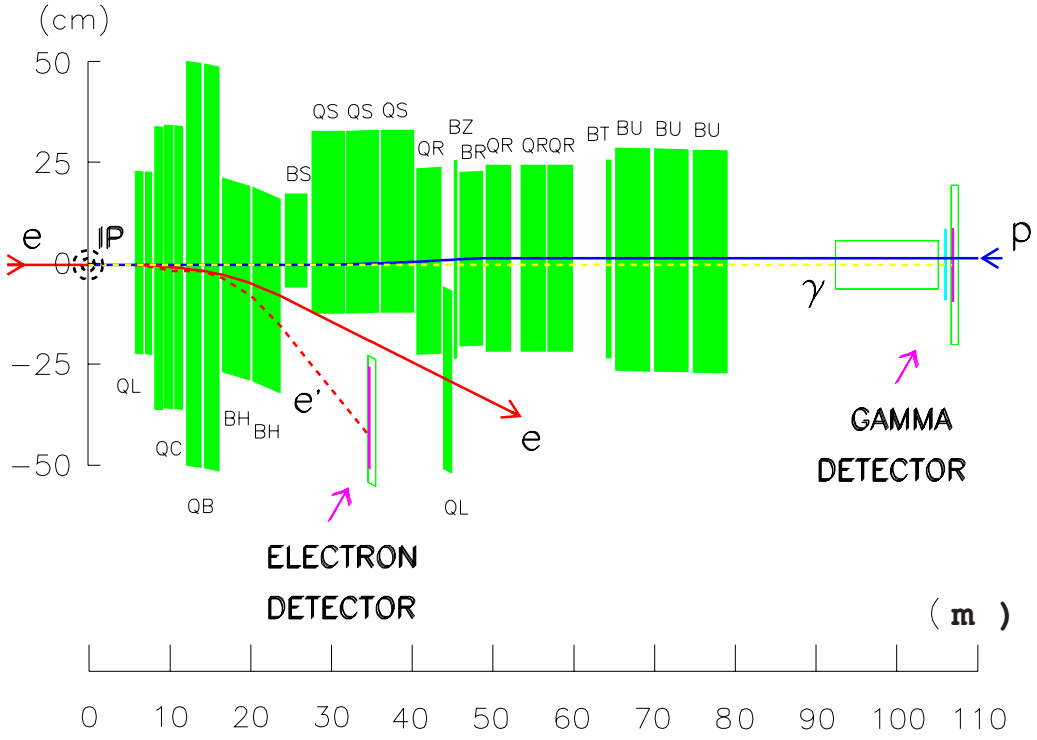


Figure 2.7: The Layout of the ZEUS luminosity monitor as well as some of the HERA quadrupole (Q) and dipole (B) magnets.

### 2.2.4 The Small Angle Rear Tracking Detector

The Small Angle Rear Tracking Detector (SRTD) is a scintillator strip detector at the face of RCAL. It covers $68 \times 68$ cm$^2$ around the RCAL beam-pipe hole, as seen in Fig. 2.8. The task of the SRTD is to improve the position measurement of electrons scattered at small angles, to correct for electron energy loss in inactive material in front of RCAL and to provide a timing-based rejection of background at the First Level Trigger (see Section 2.2.6).

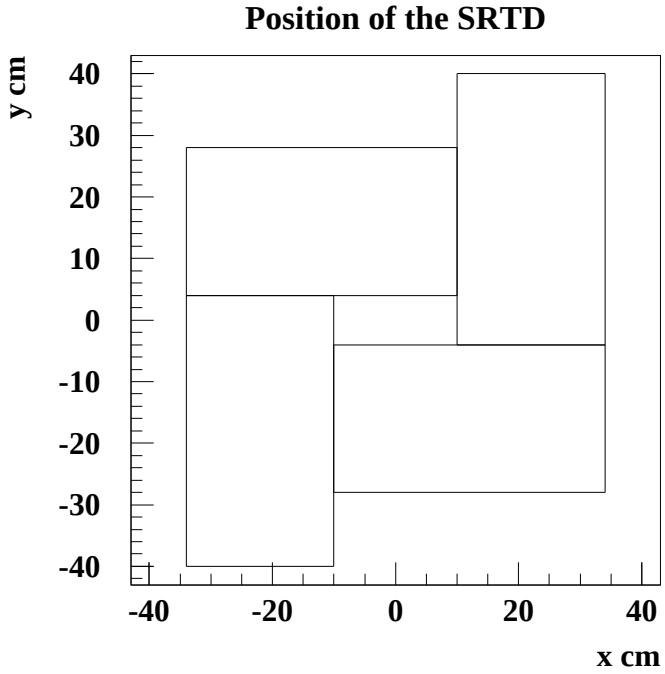


Figure 2.8: View of the SRTD Detector around the RCAL beam-pipe hole. There are two layers with horizontal and vertical scintillator strip orientation.

### 2.2.5 The Leading Proton Spectrometer

Scattered protons with a large fraction of the initial momentum of the proton are measured by the Leading Proton Spectrometer (LPS) [23],[24]. The LPS consists of six stations downstream in the HERA tunnel, located between $z = +24$ m and $z = +90$ m. At each station, six planes of silicon detectors can be moved from top and bottom or left to right, to position the detectors as close as 10 proton beam diameters to the beam axis. The detectors measure scattered protons in an azimuthal plane with the HERA magnets acting as the spectrometer magnets. The LPS (especially station LPS 6) is situated within the geometric acceptance of the Forward Neutron Calorimeter (FNC) and obscures the path of scattered neutrons.

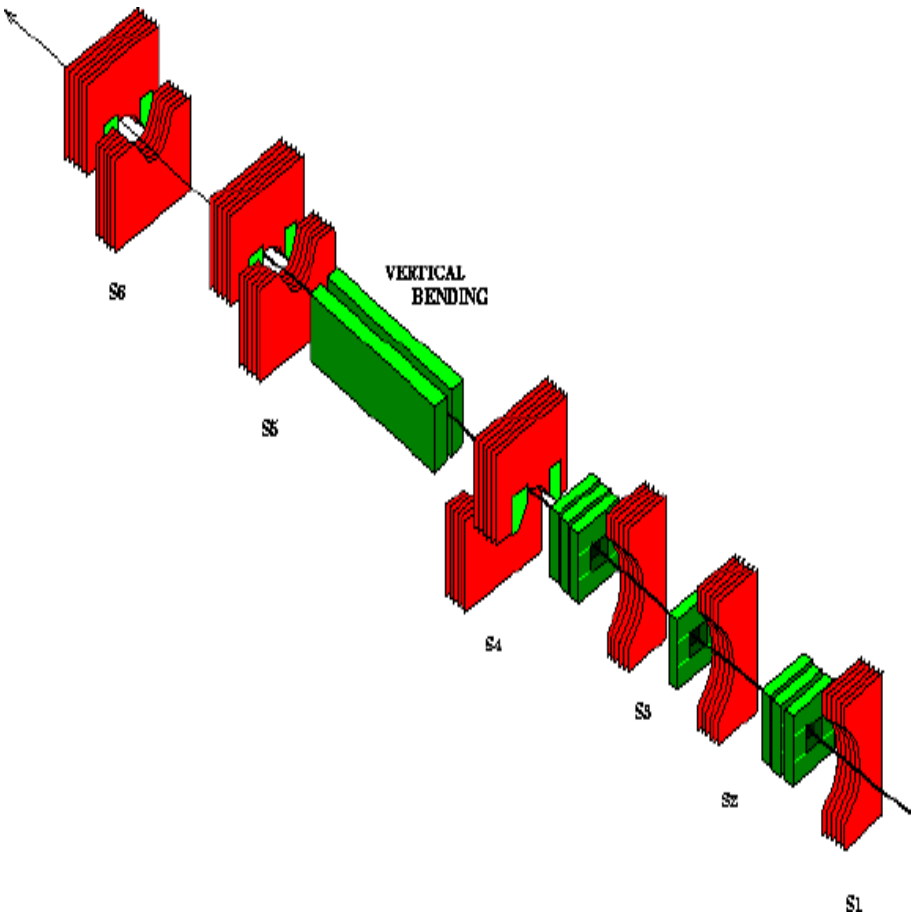


Figure 2.9: View of the LPS Stations in the HERA tunnel.

### 2.2.6 ZEUS Trigger and Data Acquisition System

The bunch crossing time at HERA is 96 ns, which is equivalent to a rate of $\approx$ 10MHz. ZEUS has developed a sophisticated three level trigger system to efficiently select $ep$ events. Both the data and trigger information are pipelined at the front end, since the decision time of the first level trigger is about 4 $\mu$sec, much longer than the bunch spacing. A schematic diagram of the ZEUS trigger system is shown in figure 2.10.

The First Level Trigger (FLT) reduces the input rate to 1 kHz or below. It is solely a hardware trigger. Each component has its own FLT. The information from the local FLTs are passed on to the Global First Level Trigger (GFLT). There, the trigger information is combined into 64 trigger decisions (so called FLT slots) and combined to an overall decision per event. If the decision is positive, the pipelines are stopped and the data for the appropriate bunch crossing are read out. This introduces dead-time in the experiment of 1 to 2 percent.

The Second Level Trigger (SLT) reduces the rate of accepted FLT events below 100 Hz. It is software based and runs on a network of microprocessors. Again each SLT component passes a trigger decision to the Global Second Level Trigger (GSLT), which rejects or accepts an event. An accepted event is passed on to the Event Builder (EB). The EB combines data from all detector components into a single event structure. This information is passed on to the Third Level Trigger (TLT).

The TLT reduces the rate to a few Hz. The TLT is software based and uses offline reconstruction code. About 80 sophisticated trigger algorithms run at the TLT to identify interesting classes of physics events. Events accepted by the TLT are written to tape via a fiber link connection to DESY computing center. The typical event size is 100 kBytes.

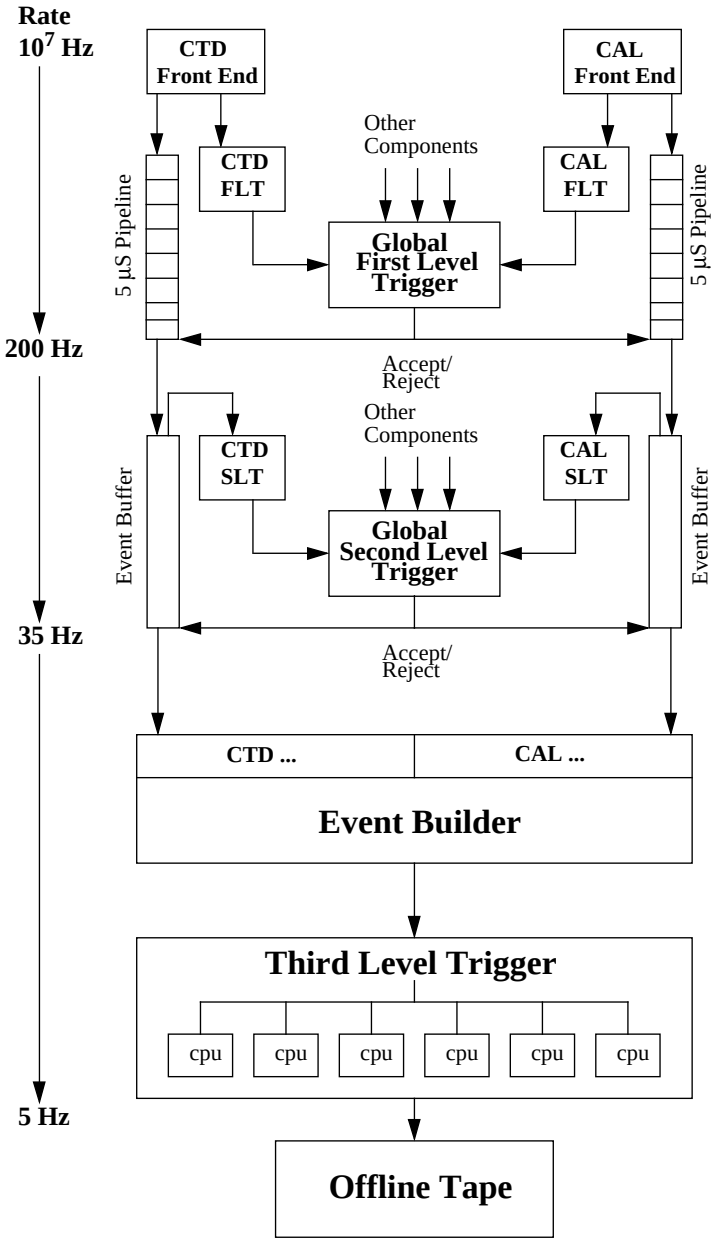


Figure 2.10: View of the ZEUS trigger and data flow.

# Chapter 3

# The Forward Neutron Detector

## 3.1 The Forward Neutron Detector

The Forward Neutron Detector (FND) is an essential component in this analysis. It consists of two components, the Forward Neutron Calorimeter (FNC) and the Forward Neutron Tracker (FNT). The FNT is positioned inside the FNC.

### 3.1.1 The Forward Neutron Calorimeter

The FNC in its current version was installed in 1995. It is situated 105.6 m downstream from the ZEUS interaction point, in the proton direction, in the HERA tunnel. Its purpose is to detect leading neutrons (LN) which are produced at very small angles in $ep$ collisions at ZEUS. It is a compensating sampling calorimeter, composed of a lead-scintillator layered structure in four sections, front and rear, each subdivided into top and bottom. The dimensions and materials of each layer can be found in table 3.1.1. The FNC is pictured in Fig. 3.1.

The FNC is located in the only space available in the HERA tunnel sufficiently far downstream that the positron and proton beams are well separated. The proton beam line passes through a $10 \times 10$ cm$^2$ hole in the top part of the calorimeter, due to the upward trajectory of the beam line after vertical bending magnets. The electron beam line passes by the side of the FNC. The FNC has lead shielding against

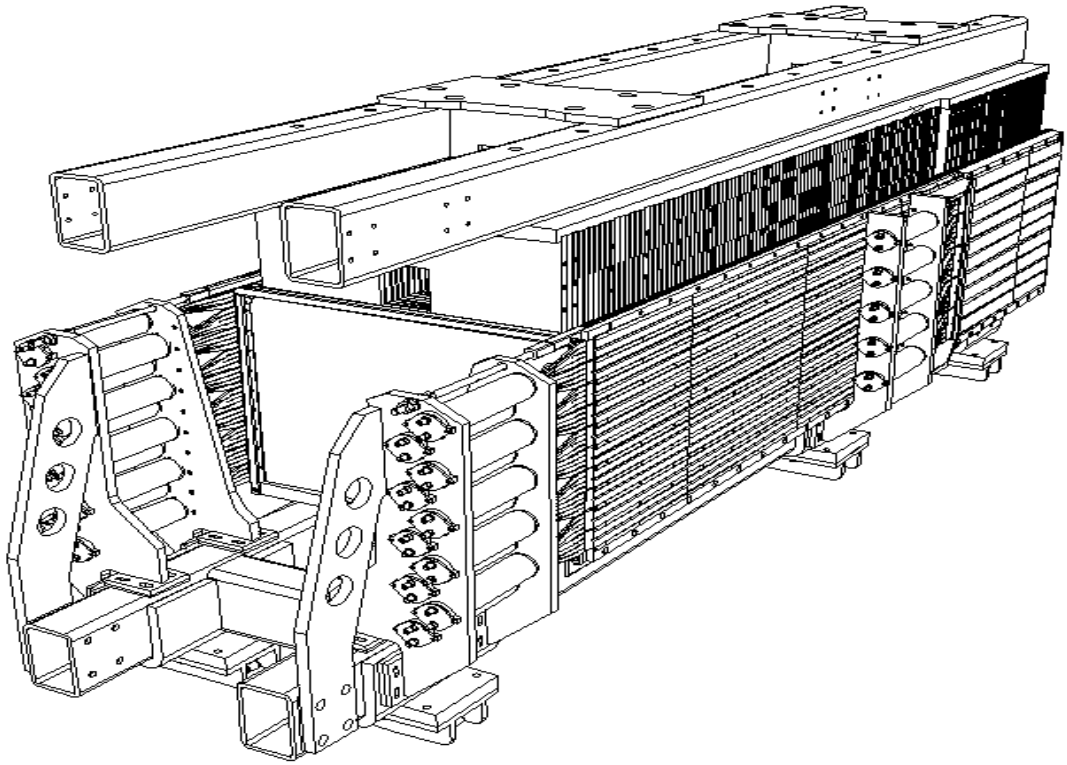

Figure 3.1: An isometric view of the FNC.

| Material | Depth (cm) | Absorption lengths $\lambda_A$ |
|---|---|---|
| Pb | 1.25 | 0.073 |
| Scintillator | 0.26 | 0.003 |
| Paper | 0.04 | 0 |
| Air | 0.1 | 0 |
| Total | 1.65 | 0.076 |
| 134 layers | 222.1 | 10.2 |

Table 3.1: The structure of a FNC cell.

synchrotron radiation originating from the electron beam line.

| Section | Layers | Length (cm) | Depth $\lambda_A$ | Height x width (cm x cm) | Tower size (cm) | PMT channels |
|---|---|---|---|---|---|---|
| Bottom front | 95 | 156.75 | 7.2 | 50 x 70 | 5 | 20 |
| Bottom rear | 39 | 64.35 | 3.0 | 50 x 74 | 10 | 10 |
| Top front | 95 | 156.75 | 7.2 | 20 x 60.5 | 5 | 8 |
| Top rear | 39 | 64.35 | 3.0 | 20 x 64.5 | 10 | 4 |

Table 3.2: The size of the different FNC sections.

The scintillators in each section are further subdivided into vertical towers. The front section has altogether fourteen towers (4 towers in the top section and 10 towers in the bottom section) with a height of 5 cm each. The scintillator strips have a height of 4.94 cm, and are wrapped in TYVEC [25], which is a white paper. TYVEC is highly reflective in the wavelength range of the light produced by the scintillating material. The top and bottom rear sections have 7 towers (2 towers in the top section and 5 towers in the bottom section) with a height of 10 cm each. The scintillators are read out by PMTs via wavelength shifters on opposite sides of each tower.

The FNC is a compensating calorimeter with a signal ratio of electromagnetic to hadronic signal $e/h \approx 1$. In a 120 GeV test beam at CERN, the hadronic energy resolution of the FNC was measured [26], to be

$$\frac{\sigma(E)}{E} = \frac{65\%}{\sqrt{E(\mathrm{GeV})}}. \tag{3.1}$$

In addition, there are three veto counter planes of scintillator at positions of 70 cm, 78 cm and 198.5 cm in front of the FNC (see Fig. 3.2). Their purpose is to reject charged particles. Due to the bending magnets in front of the FNC, any charged particle entering the FNC must be produced downstream of the magnets. Each veto plane has a size of $50 \times 70 \times 2$ cm$^3$ covering the entire front bottom of the FNC.

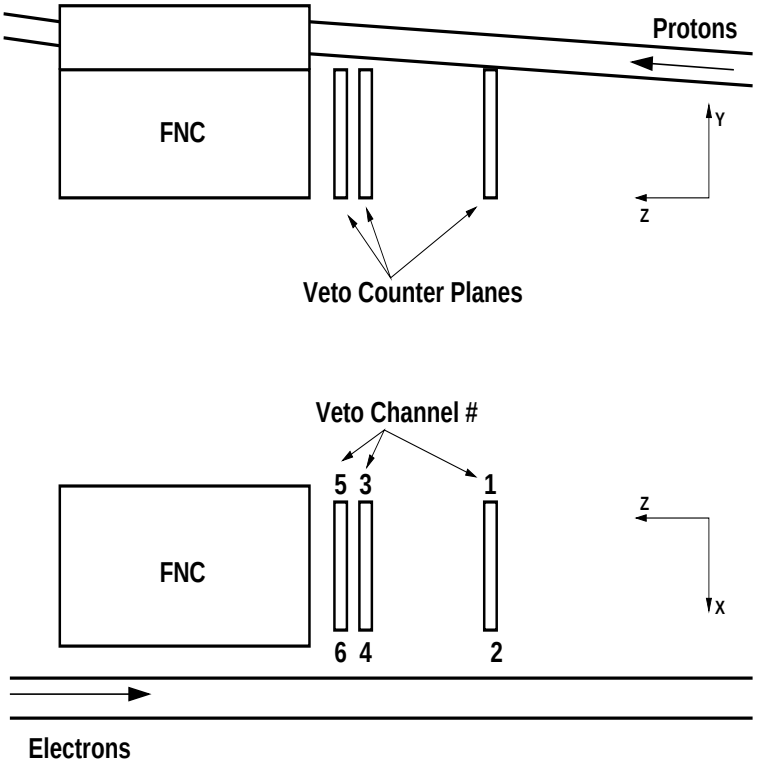


Figure 3.2: The veto counter positions and numbering scheme in front of the FND. Side view (upper) and top view (lower).

### 3.1.2 The Design of the FNT

The second component of the FND is the Forward Neutron Tracker (FNT). The FNT was installed in the spring of 1998. It consists of a hodoscope of 17 scintillator fingers for the $x$ position reconstruction and 15 scintillator fingers for the $y$ position reconstruction. They are held together by two 1 mm thick aluminum plates and separated from each other by another aluminum plate. Each scintillator finger has a size of 168 mm in length, 11 mm in width and is 5 mm in thickness. Along the finger length is a groove in which a wavelength shifting fiber of 1.6 mm diameter is glued. One end of the fiber is metallised as a reflecting mirror. The other end is glued to a clear optical fiber which guides the scintillator signal to a PMT. Each scintillator finger is wrapped in TYVEC paper. An example finger can be seen in Fig. 3.3. The clear read-out fibre is surrounded by a light blocking heat shrink tube, to eliminate cross-talk between the fibres.

Fig. 3.4 shows the two layers of the FNT hodoscope during assembly. The brass tubing visible is used to guide a radioactive source into the FNT while a source scan is performed for calibration purposes. To ensure showering of most of the incoming neutrons before the FNT, the FNT is situated approximately one interaction length deep into the FNC, replacing layer 16 of the FNC. It was positioned transversely to cover the geometric aperture for neutrons. Fig. 3.5 shows the position of the FNT hodoscope in the FNC. The geometry outline in the FNT shows the geometric acceptance as a result of material (magnets, beam pipes, etc.) which absorb the neutron beam.

### 3.1.3 The Position Resolution of the FNT

In order to measure the spatial resolution of the FNT, a slit collimator was placed in front of the outer veto counter of the FNC. The slit collimator consisted of 2 layers of lead blocks which were separated by a 1.0 mm slit.

The collimator was placed on a table which was moved vertically by a stepping motor. By controlling the position of the table, the collimator slit could be placed in front of

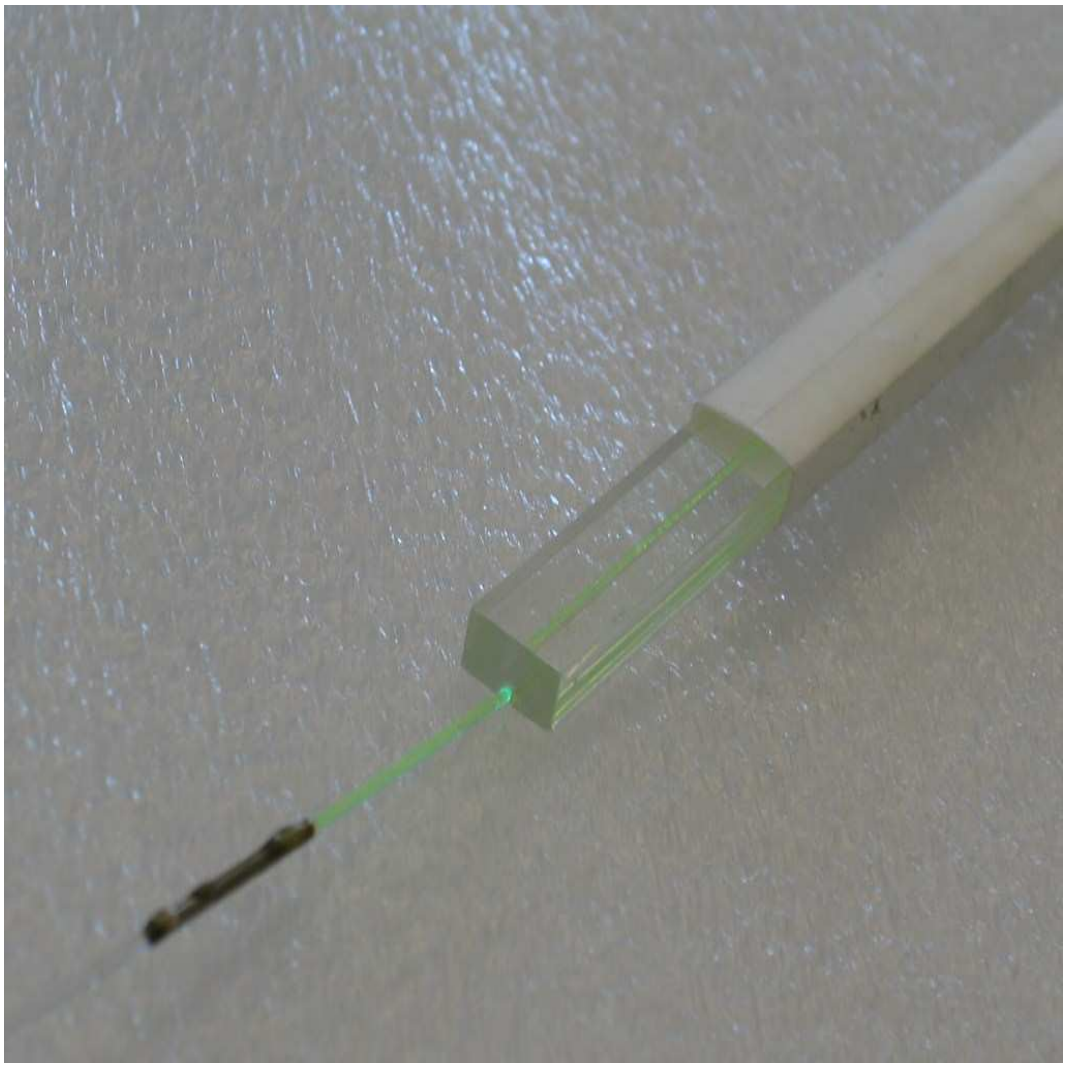

Figure 3.3: One FNT scintillator finger. The green wavelength shifter in the groove is visible. The white TYVEC paper has been partly cut. To the left the connection from the wavelength shifting fibre to the clear optical fibre can be seen.

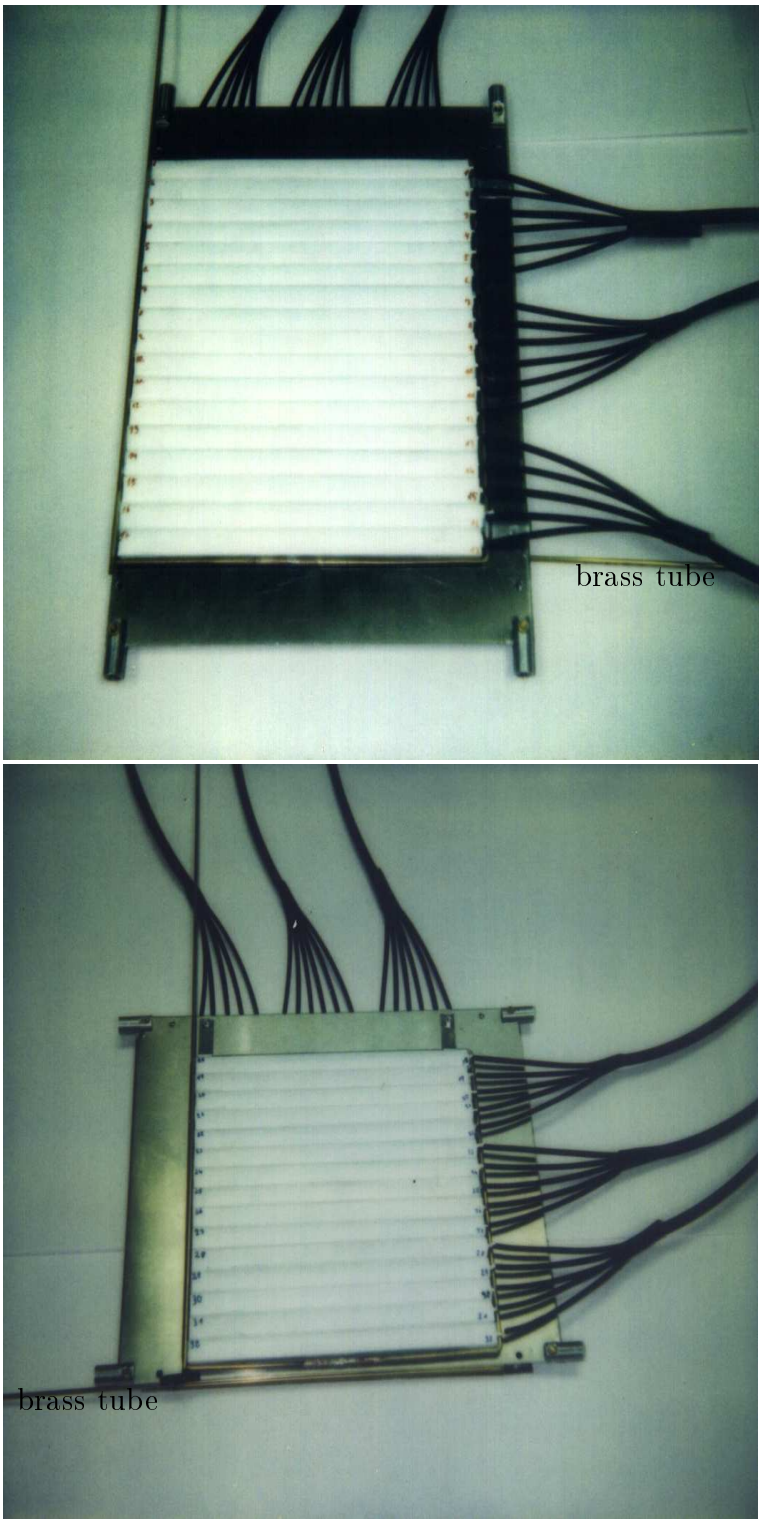


Figure 3.4: View of the two planes of the FNT hodoscope. The aluminum support plates are visible behind the scintilator fingers. The black cables are the optical fibres which connect to the PMTs.

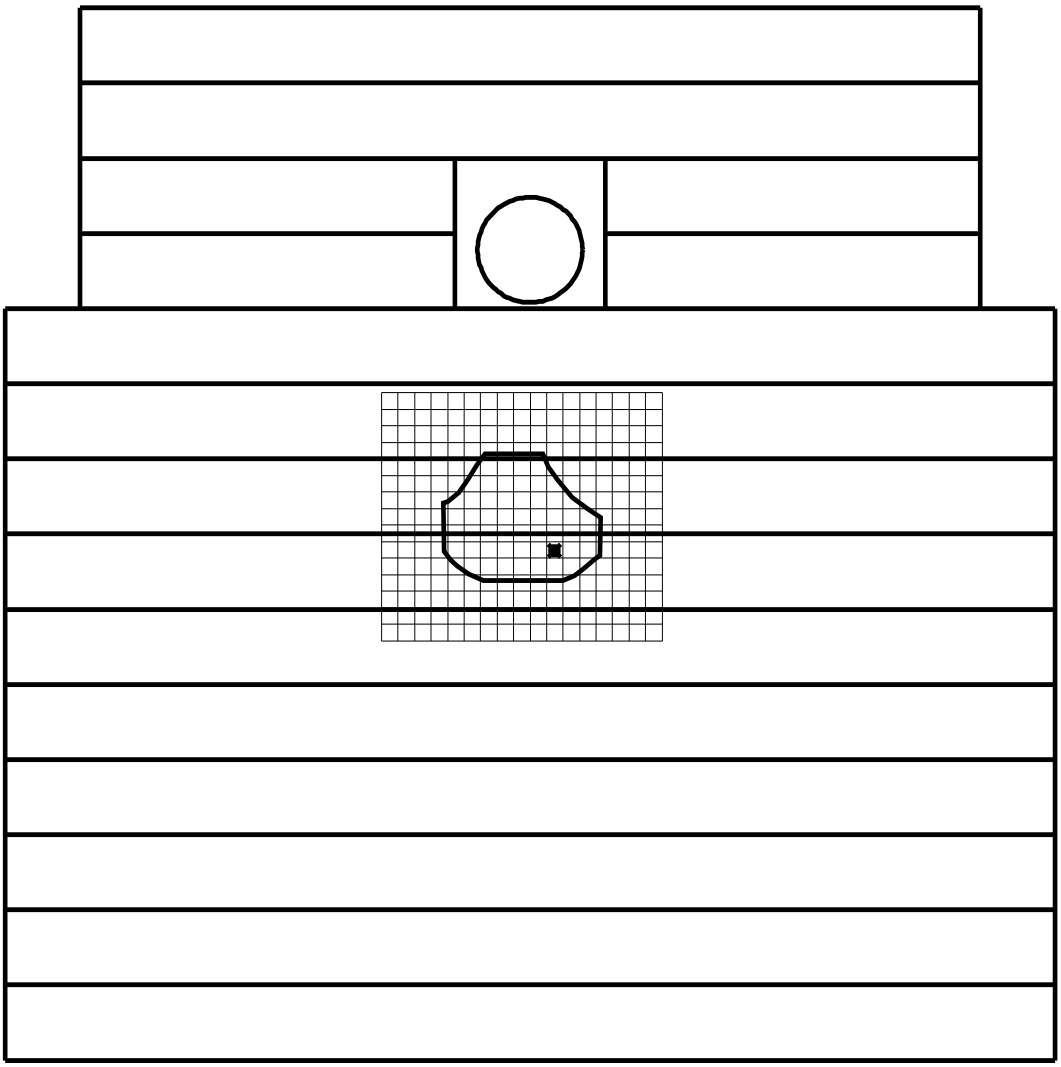

Figure 3.5: The transverse position of the FNT relative to the FNC as seen looking towards the ZEUS interaction point. The proton beam pipe and the outline of the neutron acceptance aperture due to beam line elements are shown.The dot marks the position of the beam spot.

every horizontal strip of the FNT. Figure 3.6 shows an example of the reconstruction of the $y$ measurement in the FNT with the collimator in front. It provides a measurement of the spatial resolution of the FNT. The resolution of the FNT is $\delta y = 2.3$ mm, independent of position.

Because the FNT is located approximately one interaction length deep in the FNC only 1-$e^{-1}$ of the events should shower in front of the FNT. Fig. 3.7 shows the number of events entering the FNC as a function of the $y$ plane energy in the FNT. About 63 % of the events have energy above the pedestal, as expected.

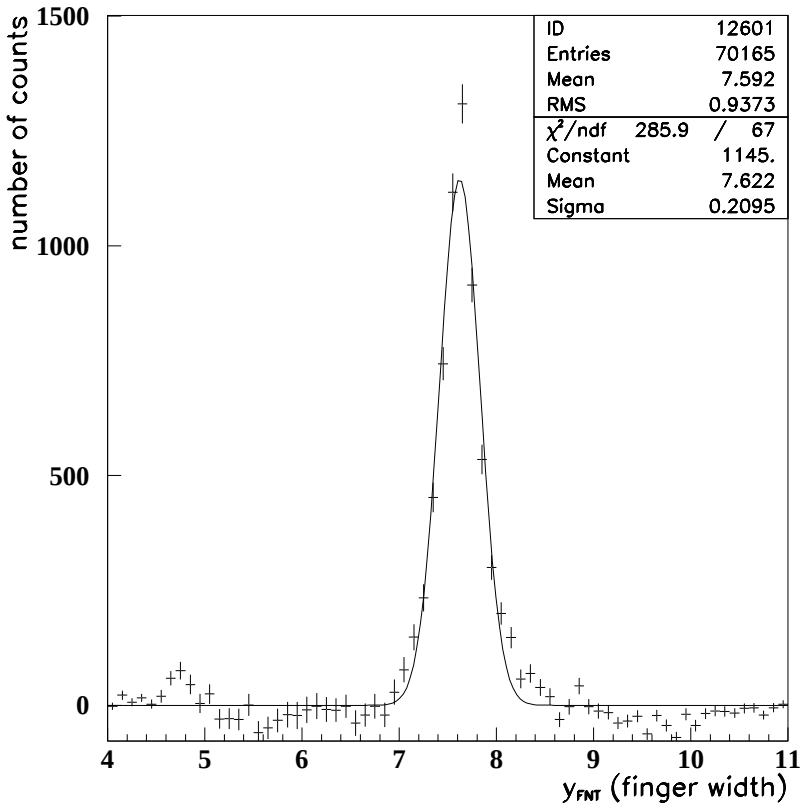


Figure 3.6: Reconstruction of y using the slit collimator in front of the FND. The mean, RMS and $\sigma$ are in units of finger separation (1.17 cm).

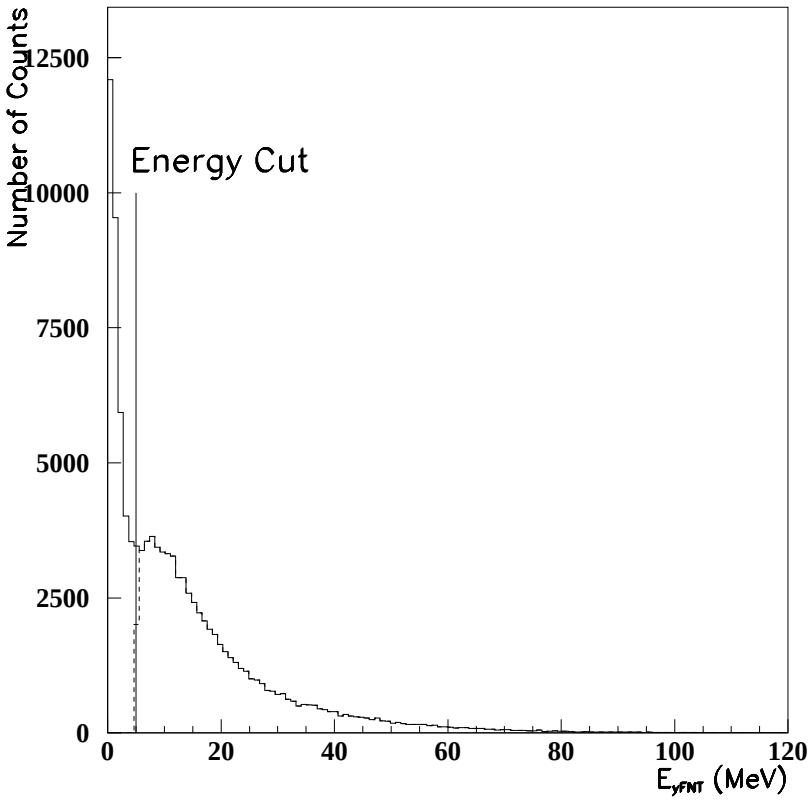


Figure 3.7: Energy in the FNT $y$ plane. A simple energy cut has been made above the pedestal.

## 3.2 The Calibration and Monitoring of the FNC and FNT

The calibration and monitoring of the FNC and FNT consist of three steps. First the gains of the PMTs are measured with a $^{60}$Co source. Secondly, the drift of the gains over time is followed with beam gas data and a time dependent correction is made. In the third step, the overall energy scale is determined using a comparison of the beam gas neutron energy spectrum to Monte Carlo simulation.

### 3.2.1 $^{60}$Co Source Scan to Calibrate Photomultiplier Gains

The relative gains of the PMTs in the FNC and FNT are obtained by scanning with a radioactive $^{60}$Co source. The method was developed for the ZEUS main calorimeter [27]. The source excites scintillators within the FNC or FNT, which leads to a signal in the PMTs. The basic principle of the FNC source scan is demonstrated in Fig. 3.8. Fig. 3.9 shows the response of the PMTs. There is a peak as the source passes each scintillator layer. The dip at layer 16 is due to the FNT. Fig. 3.10 shows the result of a scan of the FNT.

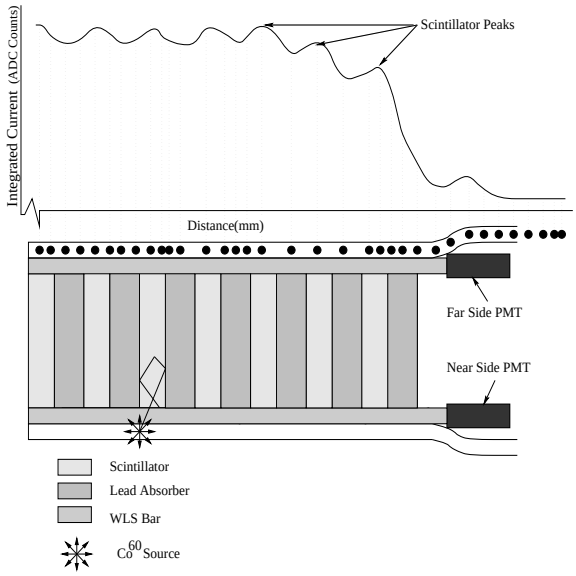


Figure 3.8: Principle of the setup of a FNC $^{60}$Co source scan to measure relative FNC PMT gains.

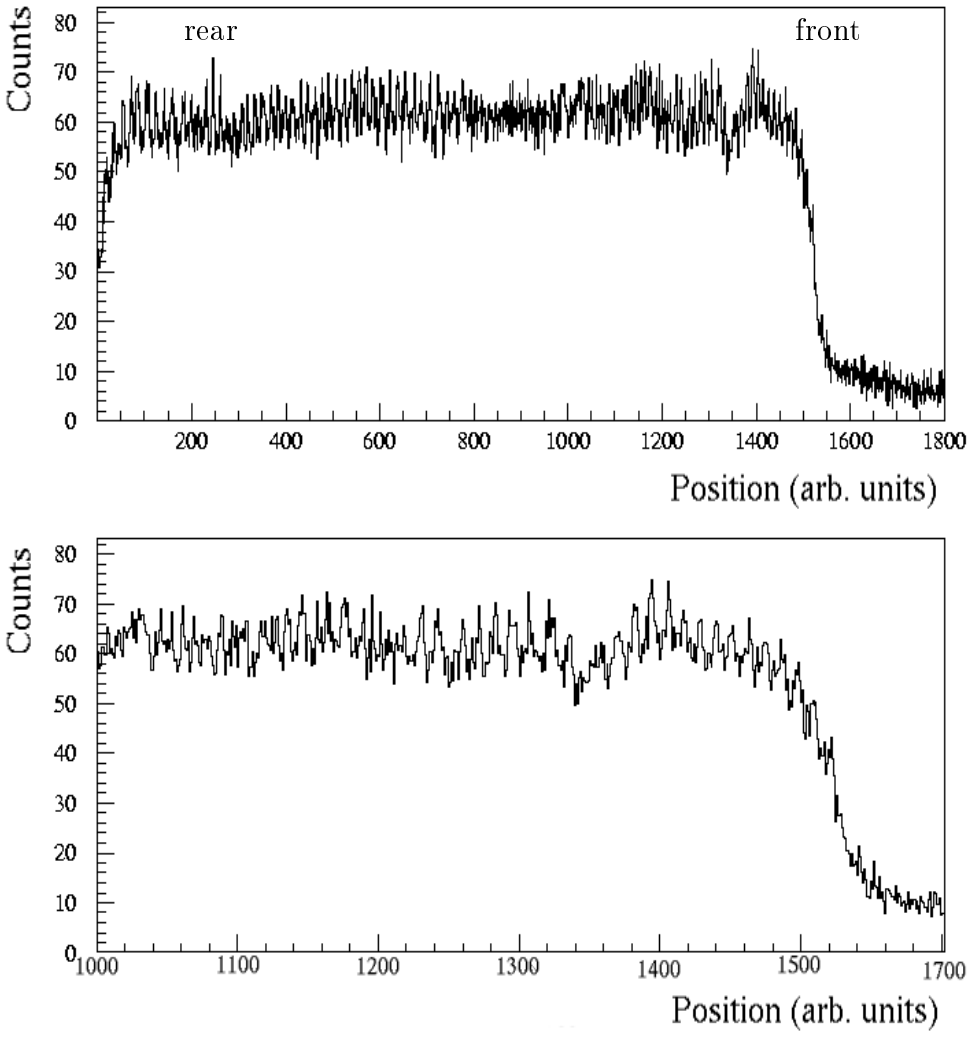


Figure 3.9: The signal (arbitrary units) of one source scan along the length of a FNC tower and a zoom of a part of it. The dip marks the position of the FNT detector in the FNC. The zoom shows the peak structure of the layers. The FNT dip is at layer 16. The front of the FNC is at the right.

The source scan signal is proportional to the amount of energy deposited. The

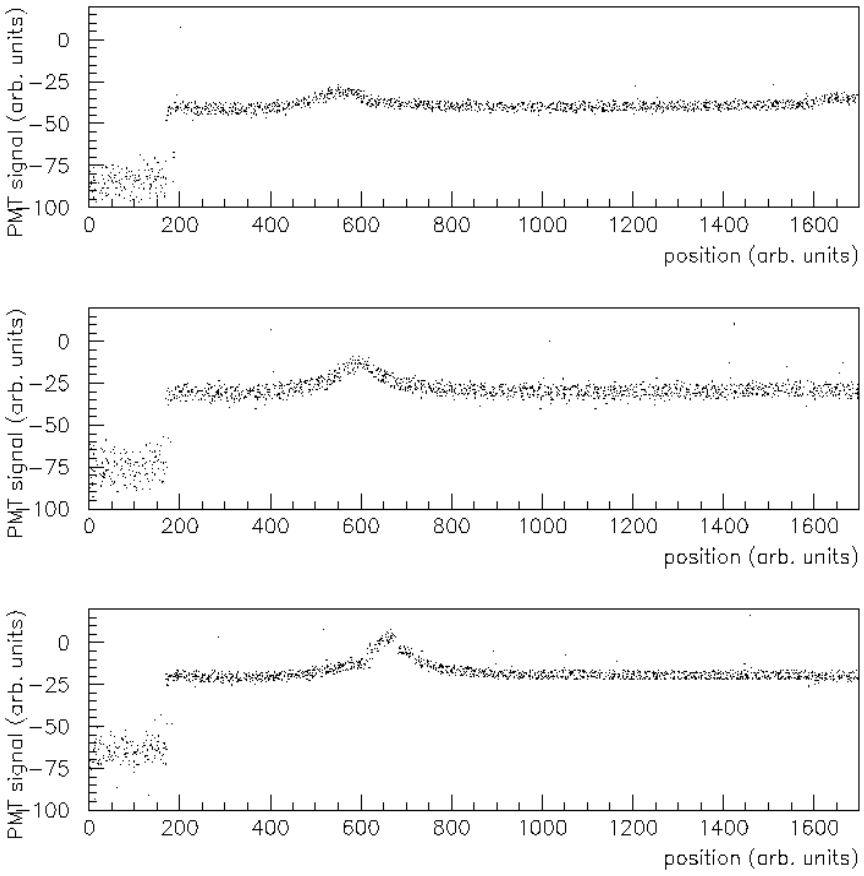


Figure 3.10: The signal (arbitrary units) of three adjacent FNT scintillators in a $^{60}$Co source scan. Each peak marks the position of a FNT scintillator.

differences in the signal height of different PMTs in the FNC or FNT are due to differing PMT gains. This method does not give absolute gains but does give the relative gains, i.e., gains relative to an average signal. For each channel $i$ the signal $a_i$ is measured. The relative gain of channel $i$ is defined as

$$g_{i,s} = N \cdot \frac{a_{i,s}}{\sum_{i=1}^{N} a_{i,s}}, \tag{3.2}$$

where N is the number of channels in the calorimeter (N=42 for the FNC. The FNT has 32 fingers, which are subdivided into two layers, N=15 or N=17) and the subscript $s$ is a particular source scan.

The $^{60}$Co source scans were performed as often as possible. The number of scans was limited, however, by the infrequent times when there was access to the HERA tunnel. Source scans were performed on average three times a year.

### 3.2.2 Beam Gas Runs

In order to monitor the gain drifts between source scans, so-called "beam gas runs" were taken at the beginning of each HERA refill when the proton beam had reached its final beam energy, but before the positrons or electrons were injected. These runs involve neutron production by the interaction of the proton beam with residual gas in the vacuum pipe. The beam gas neutron energy spectrum is well understood from hadron-hadron experiments measuring $pn \to Xp$ ($pp \to Xn$). A typical beam gas run has about 50 K events. The readout is triggered by energy deposits in the FNC. The run-to-run conditions are assumed to be stable, so the calorimeter energy spectrum shape should not change. Each change in the mean energy in a tower is therefore due to a drift in PMT gain and slowly degrading scintillators due to radiation damage, and a correction is made to the relative gains.

### 3.2.3 Energy Scale Calibration

The beam gas runs are also used to determine the FNC energy scale. The energy for each event is calculated as:

$$E(\mathrm{pC}) = \sum_{i=1}^{42} \frac{E_i(\mathrm{pC})}{g_i} \tag{3.3}$$

with the sum running over all 42 channels of the FNC. $E_i$ is the energy deposited in each tower. The energy scale is now extracted by a comparison of the energy spectrum (in units of pC) of all the events in the sum with the predicted spectrum from a Monte Carlo simulation (in units of GeV) by fitting the region of the kinematical end point of beam gas data to the Monte Carlo simulation. The Monte Carlo simulation is based on one pion exchange (OPE) and takes detector effects like resolution and the proton beam divergence into account. By fitting the kinematical end-point region, the dependencies on which particular form of OPE in the Monte Carlo simulation

is used to fit the measured beam gas data to Monte Carlo simulation is very small. The end point fit of the measured data to the predicted Monte Carlo simulation data gives in a scale factor in pC/GeV (which is determined in the fit by minimizing $\chi^2$). Fig. 3.11 shows such a fit. For each new $^{60}$Co source scan there is a new set of relative gains. One source scan fixes the calibration of a single beam gas run, the closest one in time. The extension to the whole run period is done by using the average energy deposition values from the beam gas runs between source scans as described in section 3.2.2. The whole run time is divided into approximately one week long intervals in order to reduce the amount of calibration constant information required and to average over small run to run background and beam variations. These divisions each have a corresponding calibration version. In each calibration version, the $< \mathrm{pC} >_i$ are averaged over the corresponding beam gas runs. There is a set of 42 calibration constants for each calibration version for the FNC and 32 for the FNT.

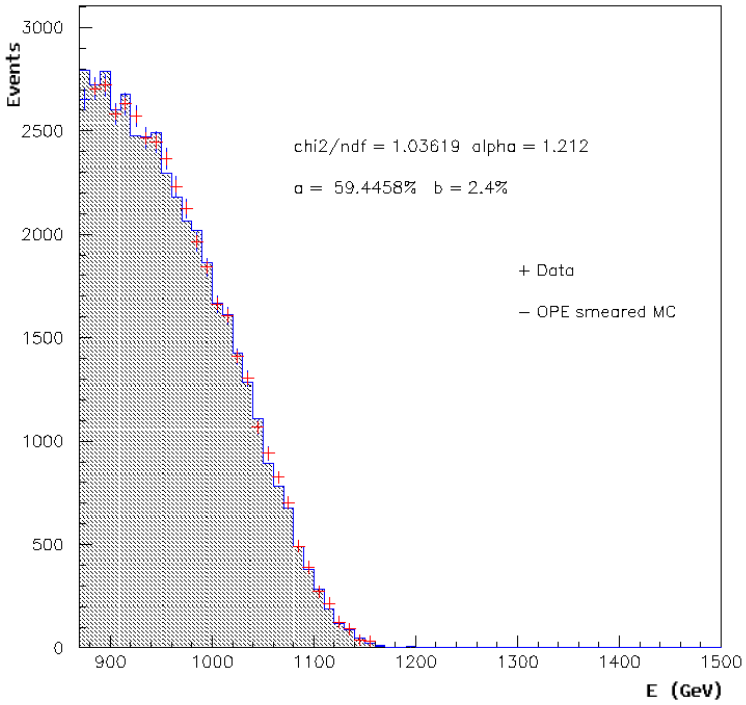


Figure 3.11: The FNC energy spectrum is fitted to a MC simulation which included the detector resolution.

### 3.2.4 Tower Balancing

After the calibration was finished, there was a depletion of high $x_L$ neutrons found in the upper part (i.e. the upper tower) of the FNC aperture. The reason for this depletion is that the calibration of the upper tower (tower 8) is off with respect to the lower tower (tower 7) of the FNC aperture. The reason for this is unknown. Expected would be a smooth distribution of energy sharing between the towers, symmetric across the boundary between the towers. This means that

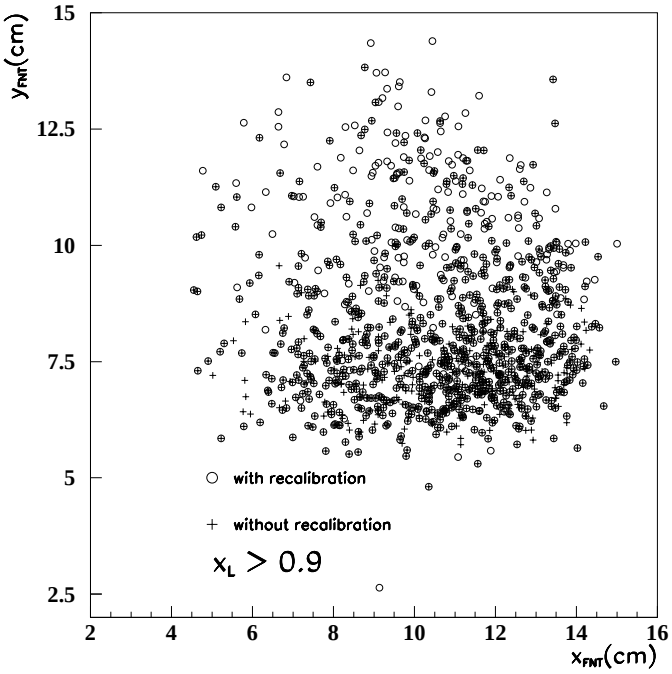


Figure 3.12: The result of the calibration correction. At high $x_L$ events populate both towers 7 and 8 uniformly in $\phi$ after the recalibration.

$$\frac{e8}{e7+e8} = F(y) = \frac{1}{2} + bf(\frac{(y-y_0)}{L}) \tag{3.4}$$

where $e8$ and $e7$ are the energies distributed in tower 7 and 8 and $f(y)$ is a 'switching' function with the limits

$$f(y) \to \pm\frac{1}{2} \tag{3.5}$$

as $y$ goes to $\pm\infty$, e.g. $1/\pi tan^{-1}(y)$. Free parameters are the boundary $y_0$, a length scale L and an amplitude b. Suppose the calibration of tower 8 is degraded by a factor $d$. Equation 3.4 changes to

$$\frac{e8/d}{(e7+e8)/d} = \frac{F(y)}{d+(1-d)F(y)} \tag{3.6}$$

and a simultaneous fit of the data is done to all four parameters. The parameter $d$ is largely independent of $x_L$. The FNT information was used to select events to balance the calibration across the tower boundaries 6/7, 7/8 and 8/9. Towers 6 to towers 9 carry approximately 90% of the overall deposited energy. After balancing the towers, the end point fit of section 3.2.3 was redone so that the overall energy scale does not change. The result of the calibration correction is that high $x_L$ events populate both towers 7 and 8 uniformly in $\phi$. Fig. 3.12 shows the change in the event population of tower 7 and 8 for $x_L > 0.9$ before and tower balancing. Note that this recalibration does not affect the FNT. The results in this thesis were compared before and after the recalibration and were not significantly different.

### 3.2.5 Energy Scale Time Stability

In the 95-97 data it was observed that the energy scale of the FNC differed from year to year even after calibration due to uncontrolled changes in the beam injection conditions. The effect was removed by rescaling the energy spectra using the Kolmogorov test. For the 98-2000 data the same procedure was followed using a sample of dijet photoproduction events in coincidence with a leading neutron. All run periods from 1998 to 2000 were used in this procedure in order to track the rescaling. The results are shown in Fig. 3.13. Data in the anomalous peak at the end of the 1999 run period are not used in the analysis. This procedure corrects each run period to an average overall energy scale. The distribution of Kolmogorov probability is almost flat, as expected. It has a peak at probabilities close to one due to the slight over-correction entailed by the method. The final energy scale was determined by matching the average overall scale of 98-2000 DIS data to the final 95-97 DIS data. The difference in energy scale between the two data sets was 1.1%, as seen in Fig. 3.14.

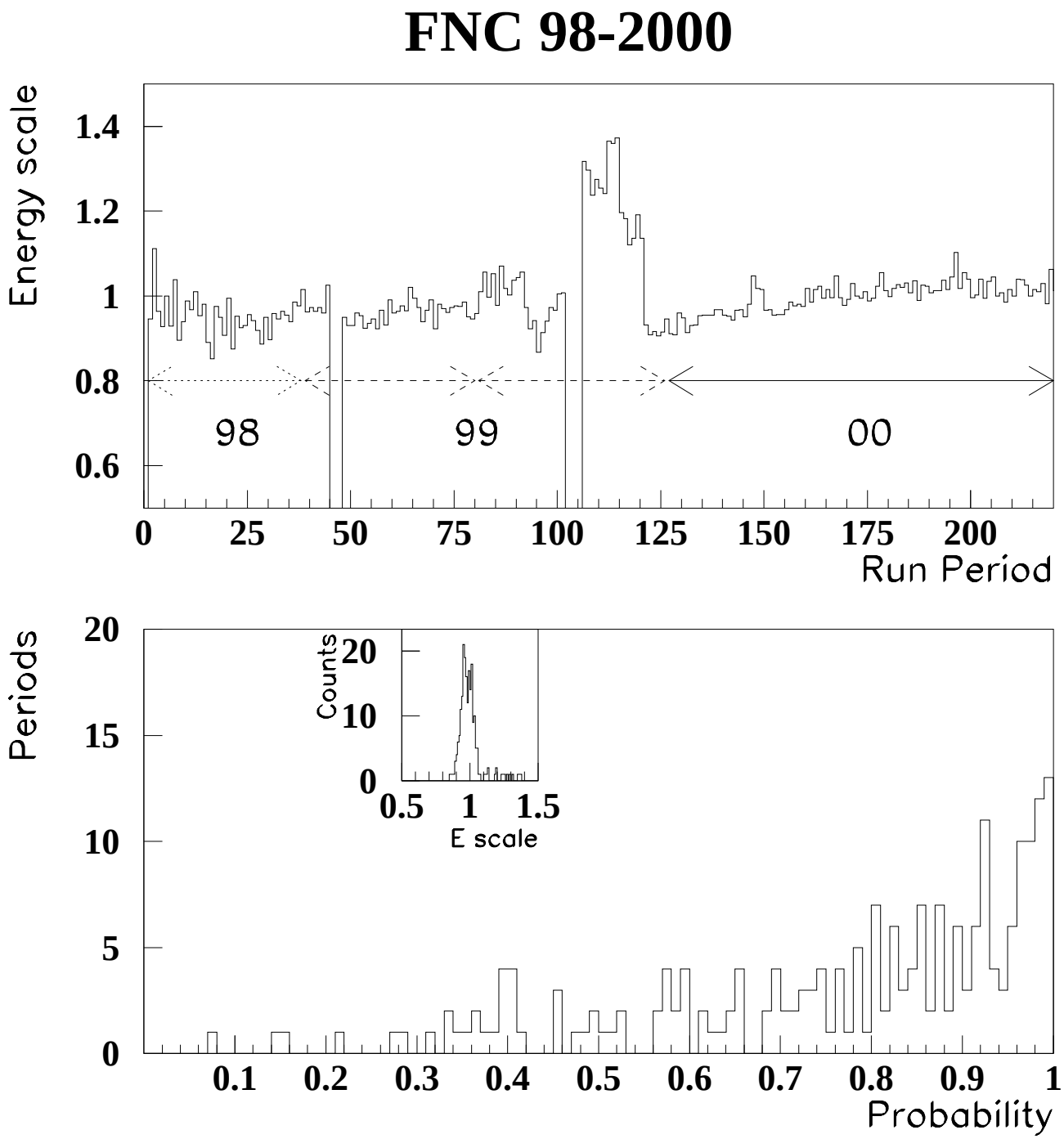


Figure 3.13: (top) The energy scale adjustment as a function of run period for the 1998 to 2000 data. The arrows indicate the run years. (bottom) The distribution of Kolmogorov probability for each run period. The inset shows a histogram of the energy scale adjustment factors.

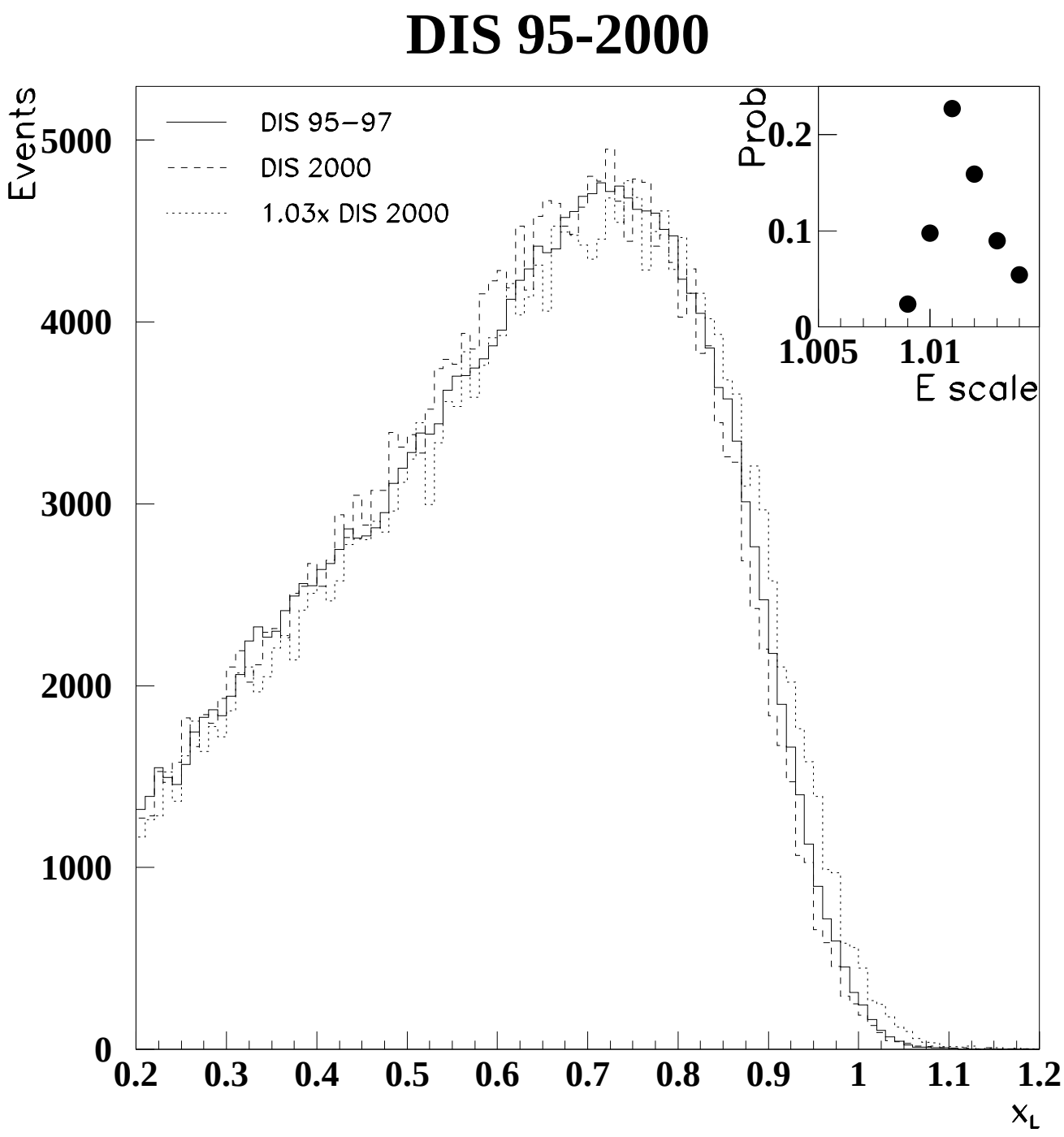


Figure 3.14: A comparison of the neutron energy spectrum in 1995-1997 (uncorrected for acceptance) to that of 1998-2000, in units of $x_L = E\,(\mathrm{GeV})/920$. The inset shows the Kolmogorov probability as a function of relative energy scale.

## 3.3 Veto Counters

There are three planes of veto counters each read out by a pair of PMTs in front of the FNC. The calibration of the veto counters has been extended from earlier FNC calibrations to include a veto counter calibration for each calibration version. The energy scale of the veto counters has been calibrated in units of minimum ionizing particle (MIP). A photon in the beam can convert to an $e^+e^-$ pair in the inactive material in front of the veto counters or in the veto counters themselves. These are used to identify a 2-MIP peak, which is seen in Fig. 3.15.

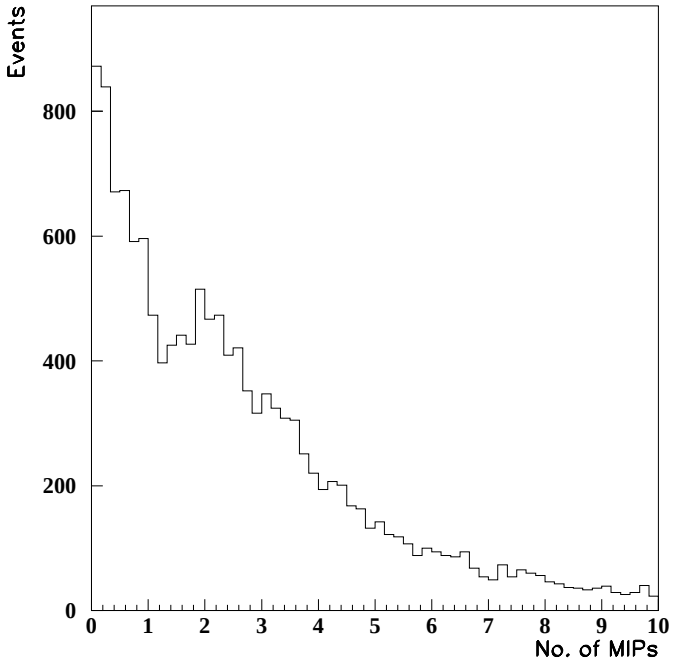


Figure 3.15: A 2 MIPs peak produced in a veto counter by pair production.

## 3.4 Position Measurement with the FND

The position of a shower in the FND can be measured using the FNC or the FNT.

### 3.4.1 Position Measurement with the FNC

In principle it is possible to make a neutron position measurement with the FNC. As described in the detector section, the FNC is read out on both sides. The ratio of energy shared between them provides the feasibility to measure the horizontal position of an incident particle as follows:

$$x = \frac{\lambda}{2} \ln(\frac{E_L}{E_R}), \tag{3.7}$$

where $\lambda$ is the scintillator attenuation length and $E_L$ and $E_R$ are the energies measured on the left and right sides of the FNC towers. The resolution is $\delta x = 22.3\,\mathrm{cm}/\sqrt{\mathrm{E}}$, as measured at 120 GeV [26]. The $y$ (vertical) position measurement of the FNC can be determined using the centroid method by taking an energy weighted average of the tower positions:

$$y = \frac{\sum_{i=1}^{10} w_i y_i}{w_i}. \tag{3.8}$$

The sum covers the front towers of the FNC. The weights, $w_i$ are functions of the energy deposits, $E_i$, in each tower. Weights are discussed further in the position reconstruction of the FNT. The large FNC tower width of 5 cm limits the resolution to $\approx 1.5\,\mathrm{cm}$ and biases the measurement to the tower center. An improved measurement of the position of the shower can be made using the FNT.

### 3.4.2 Position Reconstruction in the FNT

The $x$ or $y$ position measurement of an incident particle in the FNT can be reconstructed, using a log-weighted centroid, in the following way:

$$x_{rec} = \frac{\sum_i w_i x_i}{\sum_i w_i}, \tag{3.9}$$

where the weight $w_i$ is a function of the energy.

Two possible choices are the reconstruction with linear weights

$$w_i = E_i \tag{3.10}$$

and the reconstruction with logarithmic weights

$$w_i = \ln \frac{E_i}{f_E E_{tot}} \tag{3.11}$$

for $E_i > f_E E_{etot}$ and $w_i = 0$ otherwise. The position reconstruction is done the same way for the $x$ and $y$ positions. The value of $f_E = 0.03$ results in the smoothest distribution as seen in Fig. 3.16.

The linear reconstruction shows a bias towards the center of the scintillator finger when the shower width is of the same size as the width of the scintillator. Due to this, the logarithmic position reconstruction in $x$ and $y$ is used for the analysis.

### 3.4.3 FNT Coordinate System

The FNT reconstruction is done within its own coordinate system. The FNT coordinate system translates as follows into the ZEUS coordinate system:

$$x_{ZEUS} = (x_{FNT} - 11.3)\,\text{cm} \tag{3.12}$$

and

$$y_{ZEUS} = (y_{FNT} - 7.2)\,\text{cm}. \tag{3.13}$$

The ZEUS coordinate point (-11.3 cm, -7.2 cm) is the lower left corner of the FNT hodoscope looking towards the interaction point. It is the (0 cm, 0 cm) coordinate of the FNT coordinate system. This was determined by a survey when the FNT was installed and verified by a comparison of data to Monte Carlo. In this comparison, the number of events in the geometric acceptance is maximized by moving an outline of the geometric acceptance across the events and the events inside are counted. The maximum event position is the position as determined by the survey within $\approx$ 1mm. The geometric acceptance outline is defined by the apertures of the HERA beam line elements.

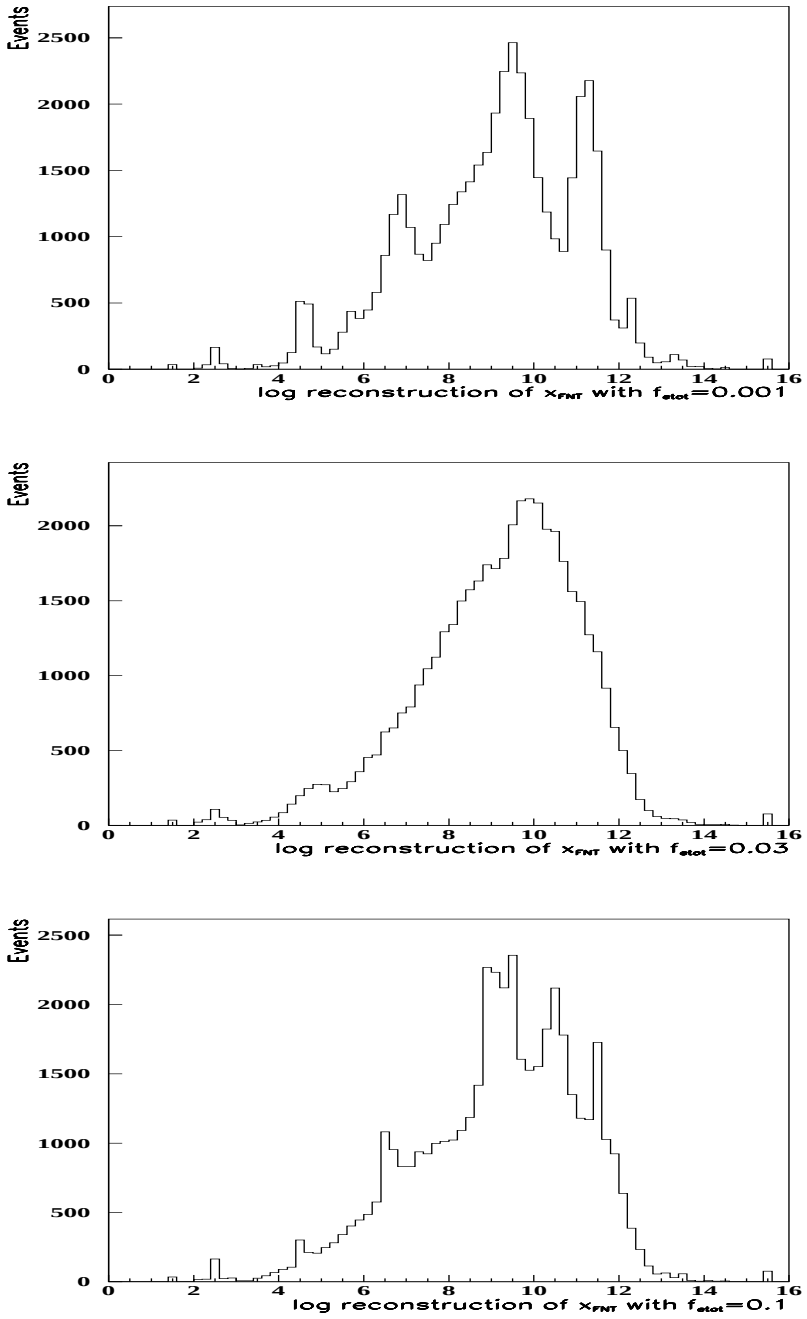


Figure 3.16: Logarithmic reconstruction of the $x$ position of FNT events with different values of the parameter $fE$.

## 3.5 Angular Distributions of Neutrons

The neutron scattering angle can be calculated in FNT coordinates as

$$\theta_n = \frac{\sqrt{(x_{FNT} - x_0)^2 + (y_{FNT} - y_0)^2}}{z_{FNT}}, \tag{3.14}$$

where $(x_0, y_0)$ is the position of the beam spot. The scattering angle $\theta_n$ is limited by the geometric aperture to a maximum value of 0.8 mrad, shown in Fig. 3.17. The circles show the contours of constant $\theta_n$. The circles have their origin at the zero degree spot of the neutron distribution.

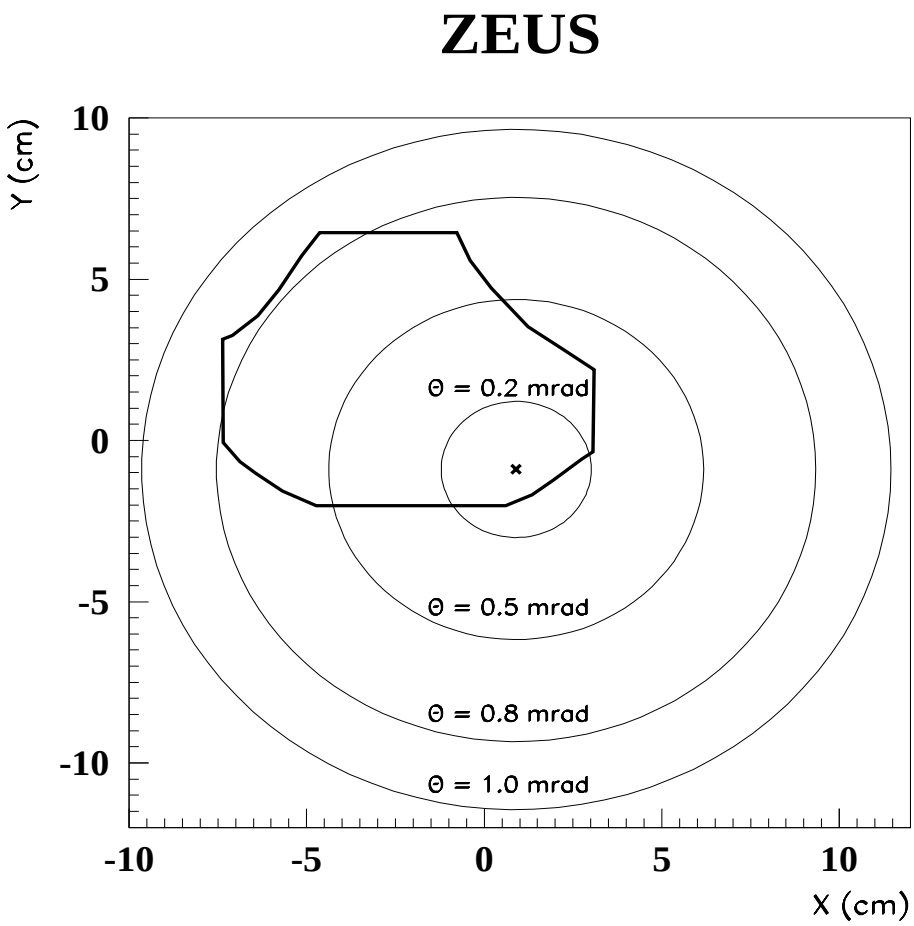


Figure 3.17: The geometric acceptance in the FNT and the contours of constant $\theta_n$.

# Chapter 4

# Theoretical Background

## 4.1 Deep Inelastic Scattering

Deep Inelastic Scattering (DIS) describes a process where a lepton scatters off a nucleon with a momentum transfer large compared to the scale of the strong interaction. The lepton can be a charged lepton ($e$, $\mu$) or a neutrino ($\nu_e$, $\nu_\mu$) and the nucleon is a proton ($p$) or a neutron ($n$). The interaction can be either a neutral current (NC) interaction mediated by the exchange of a neutral boson ($\gamma$, $Z^o$), or a charged current (CC) interaction mediated by a charged boson ($W^\pm$). At HERA the kinematic limit in $Q^2$, the momentum transfer squared, is $10^5\,\mathrm{GeV}^2$.

### 4.1.1 DIS Kinematic Variables

An electron $e$ scatters off a proton $p$ producing a scattered electron $e'$ and a hadronic final state $X$,

$$e(k)p(p) \rightarrow e'(k')X(h), \tag{4.1}$$

where

$$k = (0, 0, -E_e, E_e) \tag{4.2}$$

$$p = (0, 0, E_p, E_p) \tag{4.3}$$

$$k' = (p_{x,e'}, p_{y,e'}, p_{z,e'}, E_{e'}) \tag{4.4}$$

$$h = (p_{x,h}, p_{y,h}, p_{z,h}, E_h) \tag{4.5}$$

are the corresponding 4-vectors and the particle masses are neglected. The center-of-momentum energy is

$$\begin{aligned} s &= (k+P)^2 \\ &= k^2 + P^2 + 2k \cdot P \\ &= 4E_e E_p, \end{aligned} \tag{4.6}$$

$E_e$, $E_p$ are the energy of the electron and proton beam. The particle masses are often neglected in this thesis, because they are small compared to their much larger momenta. The momentum transfer squared $Q^2$ is the negative invariant mass squared of the exchanged (virtual) boson

$$Q^2 = -q^2 = -(k-k')^2. \tag{4.7}$$

The Bjorken scaling variables, $x$, is defined as

$$x = \frac{Q^2}{2p \cdot q}. \tag{4.8}$$

The inelasticity $y$ is

$$y = \frac{p \cdot q}{p \cdot k}. \tag{4.9}$$

This leads to the relation

$$Q^2 = s \cdot x \cdot y. \tag{4.10}$$

The exchanged boson-proton center-of-momentum energy is the total hadronic mass squared

$$W^2 = (p+q)^2 \tag{4.11}$$

$$= Q^2(\frac{1-x}{x}). \tag{4.12}$$

The rapidity, also denoted by $y$, of a particle is given by

$$y = \frac{1}{2}\ln(\frac{E+p_z}{E-p_z}), \tag{4.13}$$

which is, neglecting the masses, equal to the pseudorapidity $\eta$,

$$\eta = -\ln(\tan(\frac{\theta}{2})), \tag{4.14}$$

where $\theta$ is the production angle with respect to the proton direction.

## 4.2 Quark Parton Model

In the Quark Parton Model (QPM), the proton is assumed to be composed of free, point-like constituents, which are called partons [28]. In this model the cross section for deep inelastic $ep$ scattering is the incoherent sum of two body elastic electron-parton interactions.

The neutral current (NC) cross section can be written generally for $Q^2 << M_Z^2$ as a function of two structure functions $F_1$ and $F_2$ as

$$\frac{d^2\sigma}{dxdQ^2} = \frac{4\pi\alpha^2}{xQ^4}[\frac{y^2}{2}2xF_1(x,Q^2) + (1-y)F_2(x,Q^2)]. \tag{4.15}$$

The variable $x$ is the momentum fraction carried by the struck parton. For collisions with spin $\frac{1}{2}$ quark constituents, the structure functions $F_1$ and $F_2$ are related by the Callan-Gross relation

$$F_1(x,Q^2) = \frac{1}{2x}F_2(x,Q^2), \tag{4.16}$$

and $F_2(x,Q^2)$ can be written as

$$F_2(x,Q^2) = x\sum_i e_i^2 f_i(x,Q^2), \tag{4.17}$$

where $e_i$ is the parton charge and the parton density function (PDF) $f_i(x,Q^2)dx$ is the probability of finding a quark i of charge $e_i$ in the momentum range of $x$ to $x+dx$. The Callan-Gross relationship is a consequence of the spin $\frac{1}{2}$ nature of partons; partons with spin zero would have a ratio $2xF_1/F_2 = 0$. In the QPM, these PDFs depend only on $x$ and have no dependence on the scale $Q$. This is called scale invariance [29]. The Callan-Gross relation and the scaling hypothesis were confirmed at the Stanford Linear Accelerator in 1969 [30].

If the proton consisted only of charged partons (quarks) momentum conservation implies

$$\sum_i \int_0^1 x f_i(x)dx = 1. \tag{4.18}$$

The experimentally found value is $\approx 0.5$ [31]. This can be understood if about half of the proton's momentum is carried by neutral partons, called gluons. Experimental

evidence of these gluons was found in 1979 at DESY [32]. ZEUS and other experiments have confirmed scale invariance for $x \approx 0.15$ as seen in Fig. 4.1. However, variations in $F_2$ with $Q^2$ are seen at lower and higher values of $x$, thus breaking scale invariance. The theory of quantum chromodynamics (QCD) explains this deviation from the expectations of the simple quark parton model by introducing the radiation of gluons from quarks and the splitting of gluons to quark-anti-quark pairs.

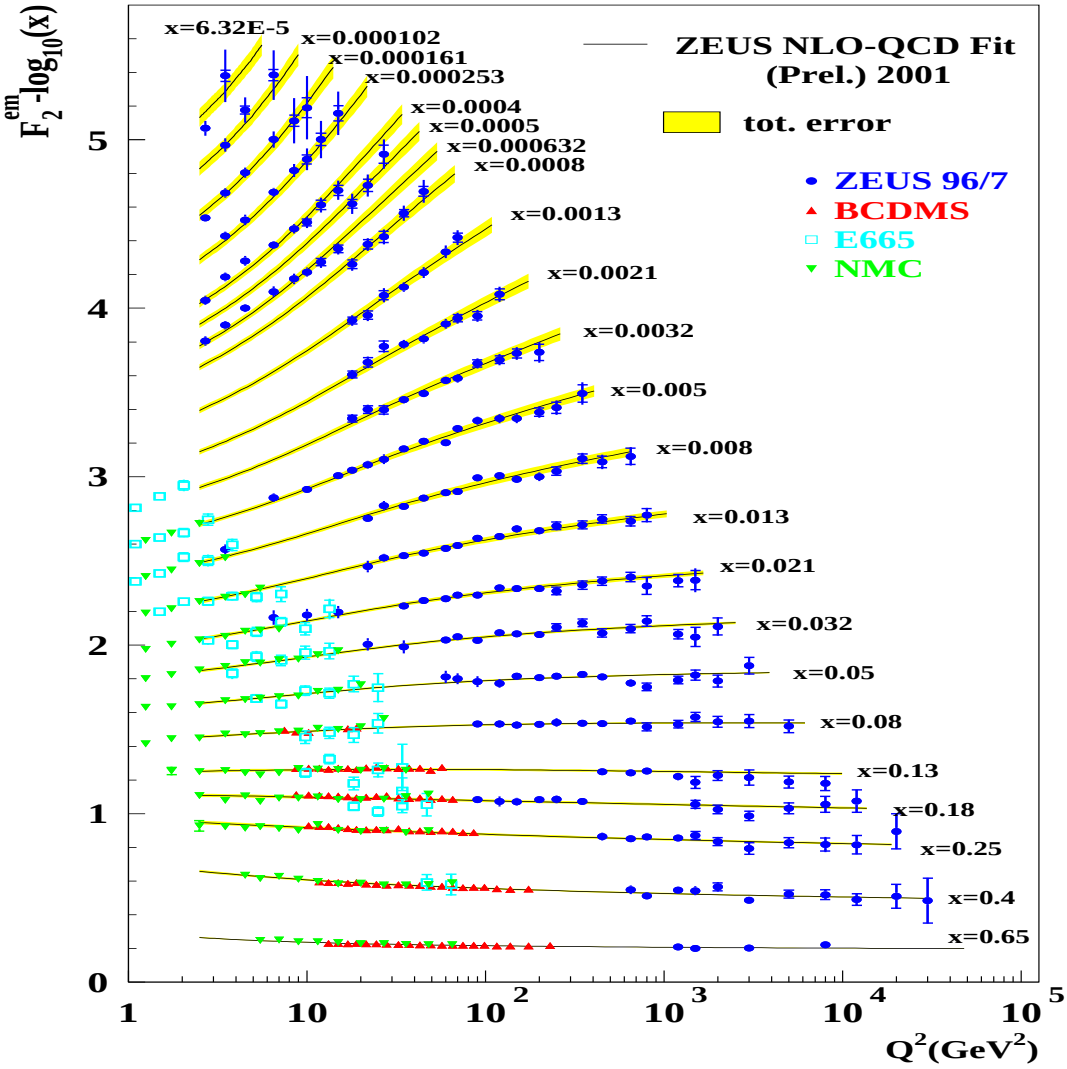


Figure 4.1: The structure function $F_2(x, Q^2)$ as a function of $Q^2$ and fixed $x$ values.

## 4.3 Quantum Chromodynamics

Quantum Chromodynamics (QCD) is a theory developed in the 1970s to describe the physics of the strong interaction. QCD is a non-abelian gauge theory based on a SU(3) colour symmetry group. In QCD, quarks interact by exchanging gauge bosons, called gluons. The gluons can couple to each other as well, due to a colour charge they carry. The colour coupling in QCD is distance dependent and decreases at very short distances. In leading order perturbation theory the scale dependence of the strong coupling constant, $\alpha_s$, is given by

$$\alpha_s = \frac{12\pi}{(33 - 2n_f)\ln(\frac{\mu^2}{\Lambda^2})}, \tag{4.19}$$

where $n_f$ is the number of quark flavors and $\mu$ is an arbitrary scale. $\Lambda$ is the QCD scale parameter at which the strong coupling constant becomes large and perturbation theory breaks down.

Non-perturbative effects make it impossible to calculate inclusive cross sections in QCD from first principles. The factorization theorem [33] can be used to describe the cross section for $ep$ scattering as

$$\sigma_{ep} = \sum_i f_{i/p}\sigma_{ei} \tag{4.20}$$

where $\sigma_{ei}$ is the cross section for a short distance (perturbative) interaction and $f_{i/p}$ are the parton density functions which sum over long distance (non-perturbative) effects and have to be determined experimentally. The PDFs are hadron dependent, but the cross sections $\sigma_{ei}$, which can be calculated perturbatively, depend only on the parton i. This separation into a short distance part calculable in perturbative QCD and a long distance part is called factorization. The separation itself is determined by a so-called factorization scale $\mu$. The cross section in $ep$ scattering, $\sigma_{ep}$, is measurable and hence must be independent of the choice of the factorization scale $\mu$.

## 4.4 Regge Exchange

Prior to QCD, an understanding of the strong interaction observed in scattering experiments at high energies was achieved by Regge theory [34]. It is not based on

a microscopic theory, but rather on basic properties of the scattering amplitudes. In principle therefore, it should be possible to predict the results of Regge theory from QCD but this has so far not proven tractable. Regge theory gives a good description of soft hadronic interactions, in particular of their cross sections. In the Regge picture the interaction of hadrons $ab \rightarrow cd$ is mediated by exchanged particles that lie on linear trajectories in angular momentum, $\alpha$, as a function of $t$, the momentum transfer squared carried by an exchanged virtual particle. $\alpha(t)$ is a continuous complex variable. The cross section results from the sum of all possible exchanges consistent with the exchanged quantum numbers. The observable poles on these trajectories are the particles at $t = m_\alpha^2$ with $\alpha = 0, 1, 2....$ The region of viability for Regge theory is at high $s$ and small momentum transfer. It is convenient to analyse the scattering amplitude as a partial wave series which can be transformed into a sum of Regge trajectories [35], [36], [37], [38]. The scattering amplitude $A$ takes the form

$$A \propto s^{\alpha(t)}, \tag{4.21}$$

with the Regge trajectory $\alpha(t)$ defined as

$$\alpha(t) = \alpha_0 + \alpha' t, \tag{4.22}$$

and the differential cross section in $t$ is given by

$$\frac{d\sigma}{dt} \propto s^{2\alpha(t)-2}. \tag{4.23}$$

The total cross section at high $s$ is given by

$$\sigma \propto s^{\alpha_{I\!P}(0)-1}, \tag{4.24}$$

where $I\!P$ is the so-called 'pomeron'. The pomeron is a trajectory with an intercept slightly greater than 1 and the same quantum numbers as the vacuum. Originally it was introduced in Regge theory to explain slowly rising cross sections in hadron-hadron interactions.

## 4.5 Leading Neutron Production

The semi-inclusive production of neutrons, $ep \rightarrow enX$, where the neutron is produced a at small angle $\theta_n$ and carries a large fraction of the momentum of the initial state

proton, is called leading neutron (LN) production [5], [8], [10]. Fig. 4.2 shows the Feynman diagram of semi-inclusive leading neutron production in $ep$ collisions. To describe LN production, two hadronic variables are introduced. The momentum transfer, $t$, from the target proton to the produced neutron and the inelasticity, $(1 - x_L)$, are given by

$$t = (p - p')^2 \tag{4.25}$$

$$(1 - x_L) = \frac{k \cdot (p - p')}{k \cdot p}. \tag{4.26}$$

The variables $t$ and $(1 - x_L)$ are the hadronic equivalents for the detected neutrons of the leptonic variables $Q^2$ and $y$. The momentum transfer from the initial proton momentum to the leading neutron is small, because the leading neutrons are produced at very small scattering angles. In the lab frame, $x_L$ and $p_T^2$, the transverse momentum squared of the neutron, are given by:

$$x_L = \frac{|p_z|}{|p|} \simeq \frac{E_n}{E_p} \tag{4.27}$$

$$p_T^2 = -t \cdot x_L - (1 - x_L)(m_n^2 - x_L m_p^2) \tag{4.28}$$

$$\simeq (x_L E_p \theta_n)^2, \tag{4.29}$$

where $E_p$ is the proton beam energy and $\theta_n$ is the neutron production angle with respect to the proton direction. Here $x_L$ is estimated as the energy fraction of the incident proton carried by the produced neutron.

## 4.6 One Pion Exchange

In the $p \to n$ transition the $\pi$ on the pion trajectory (with $\alpha(0) = \alpha_0 = m_\pi^2$ and $\alpha' = 1$) and the $\rho$ on the rho trajectory can be exchanged. However, due to its small mass, the pion dominates the transition amplitude and its relative contribution increases as $|t|$ decreases. Therefore one-pion-exchange (OPE) is an often proposed mechanism for the successful description of leading neutron production data. The HERA leading neutron data allow the low $x$ structure of the pion to be probed. The simple OPE picture (Fig. 4.2) can be exploited by employing factorization. The cross

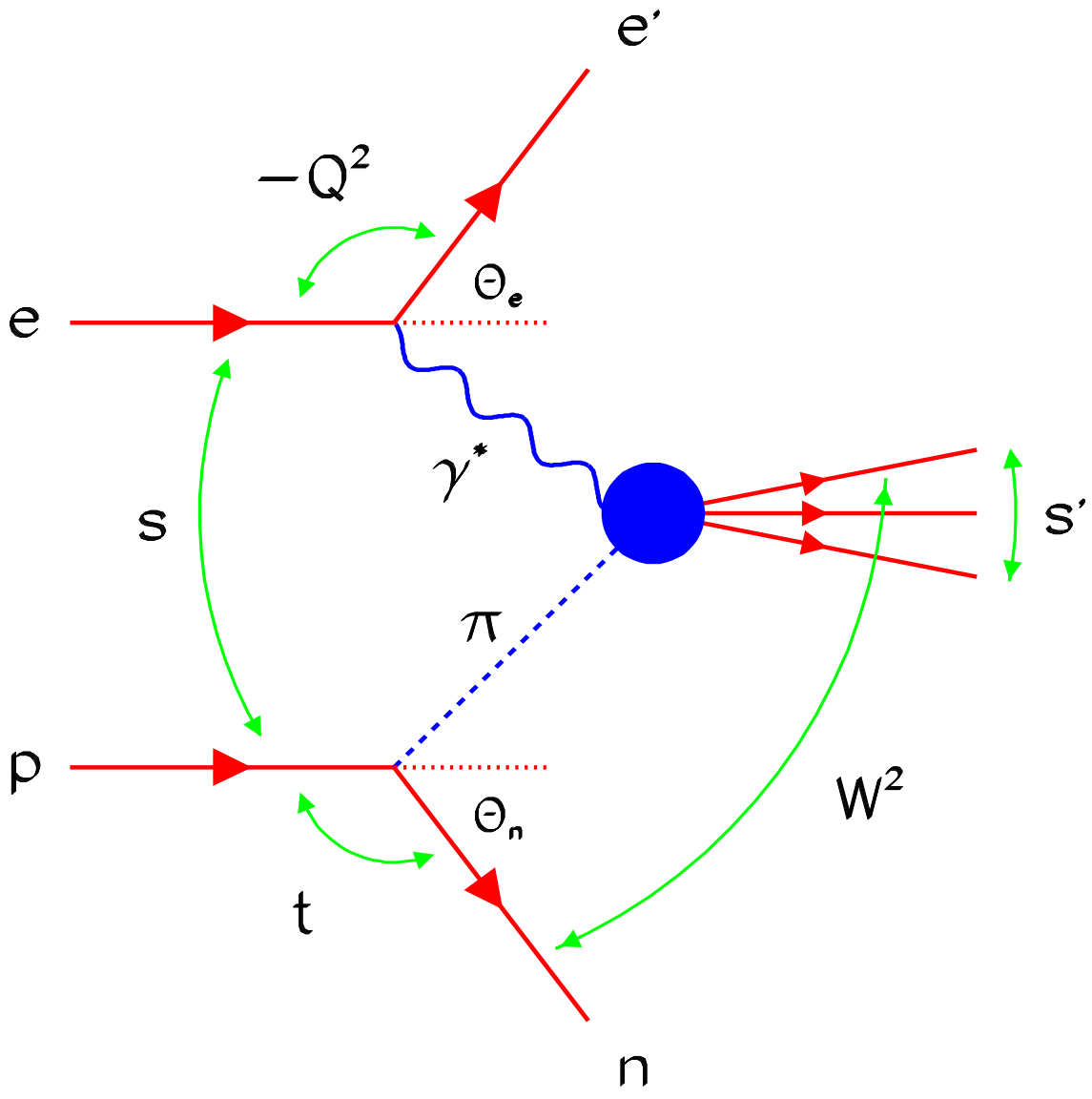


Figure 4.2: The Feynman diagram for OPE.

section for semi-inclusive $ep \to enX$ factorizes into two terms:

$$\frac{d\sigma^2(W^2, Q^2, x_L, t)}{dx_L dt} = f_{\pi/p}(x_L, t) \cdot \sigma_{\gamma^*\pi}((1 - x_L)W^2, Q^2), \tag{4.30}$$

where $W$ represents the center-of-mass energy of the virtual photon-proton system, $t$ represents the four-momentum squared (the mass of the exchanged pion) carried by the exchanged pion, $f_{\pi/p}$ is the flux of the virtual pions in the proton and $\sigma_{\gamma^*\pi}$ is the total cross section of the scattering of the virtual photon and virtual pion.

To evaluate the flux factor is crucial. There are two choices found in the literature:

• The OPE diagram can be expressed in the form of a Reggeized pion trajectory. The Reggeized pion flux factor is of the general form

$$f_{\pi/p}(x_L, t) = \frac{1}{4\pi}\frac{g^2}{4\pi}\frac{-2t}{(t - m_\pi^2)^2}(1 - x_L)^{1-2\alpha_\pi(t)}(F(t))^2, \tag{4.31}$$

where $F(t)$ is a form factor, accounting for off-mass shell corrections, and $g$ is the $p\pi^0 p$ coupling constant. The pion trajectory is given by $\alpha(t) = (t - m_\pi^2)/(1\,\mathrm{GeV}^2)$ that is $\alpha_0 \approx 0$ and $\alpha' \approx 1\,\mathrm{GeV}^{-2}$. The form factor is independent of $x_L$. In the literature it is usually considered to be exponential or Gaussian [39], [40], [41].
• A non-reggeized pion flux omits the pion trajectory (i.e., $\alpha_\pi(t)$ is set to 0). This leads to a flux given by

$$f_{\pi/p}(x_L, t) = \frac{1}{4\pi}\frac{g^2}{4\pi}\frac{-2t}{(t - m_\pi^2)^2}(1 - x_L)(F(t, x_L))^2, \tag{4.32}$$

where the form factor $F$ can depend on both $t$ and $x_L$.

Five different form factors are considered in this thesis:

- a Gaussian

$$F(t) = \exp(-R^2(t - m_\pi^2)^2) \tag{4.33}$$

- a simple exponential

$$F(t) = \exp((b(t - m_\pi^2)) \tag{4.34}$$

- an n-pole approach

$$F(t) = \left(\frac{\Lambda^2 - m_\pi^2}{\Lambda^2 - t}\right)^n \tag{4.35}$$

(n = 1 is called monopole, n = 2 is called dipole)

- a light-cone exponential

$$F(t, x_L) = \exp\left(b\frac{t - m_\pi^2}{1 - x_L}\right) \tag{4.36}$$

- a light-cone dipole approach

$$F(t, x_L) = \exp\left(b\frac{\Lambda^2 - m_p^2}{\Lambda^2 + m_p^2 + \frac{m_\pi^2 - t}{1 - x_L}}\right) \tag{4.37}$$

The Gaussian and exponential form factors are used in Reggeized OPE and the other three form factors, as well as the exponential, are used in non-Reggeized OPE. The values of $R^2$ and the slopes $b$ are obtained from data [42], [43], [3], [41], [44], [45]. The values for non-Reggeized $b$, $R^2$, $\Lambda^2$ can be obtained from [46], [47],[48], [49], [50], [51], [52], [53], [54] and [55]. Different authors use different expressions for the form factor and different values for parameters. Table 4.1 gives an overview of some of the preferred parameters.

| Author | Form-Factor | Parameter | Reference |
|---|---|---|---|
| Bishari-0 | exponential | $b = 0$ GeV$^{-2}$ | [39] |
| Bishari-4 | exponential | $b = 2$ GeV$^{-2}$ | [39] |
| KPP | exponential | $b = 0.3$ GeV$^{-2}$ | [39] |
| NSSS | Gaussian | $R = 1.5$ GeV$^{-1}$ | [41] |
| GKS | exponential | $b = 1.2$ GeV$^{-2}$ | [47] |
| FMS | exponential | $b = 1.8$ GeV$^{-2}$ | [46] |
| FMS | monopole | $\Lambda^2 = 0.25$ GeV$^2$ | [46] |
| FMS | dipole | $\Lambda^2 = 0.81$ GeV$^2$ | [46] |
| PSI,SNS | light-cone exp. | $b = 0.4$ GeV$^{-2}$ | [48],[56] |
| MST | light-cone dipole | $\Lambda = 1.5$ GeV | [55] |

Table 4.1: The type of expression used for the form factor by different authors and the values of parameters used.

## 4.7 Photoproduction

When the virtuality of the exchanged photon is close to zero, $Q^2 \approx 0$, the regime of photoproduction is reached. At HERA the range of photoproduction extends from $Q^2 \approx 10^{-8}$ GeV$^2$ (quasi-real) to $Q^2 \approx 4$ GeV$^2$. There are two types of processes contributing to photoproduction. The first is direct photoproduction, where the photon interacts directly with a parton from the proton. The full photon 4-momentum is present and the coupling is point-like. Fig. 4.3 shows an example of direct photoproduction. The photon interacts directly with the gluon via a quark to produce a quark anti-quark pair.

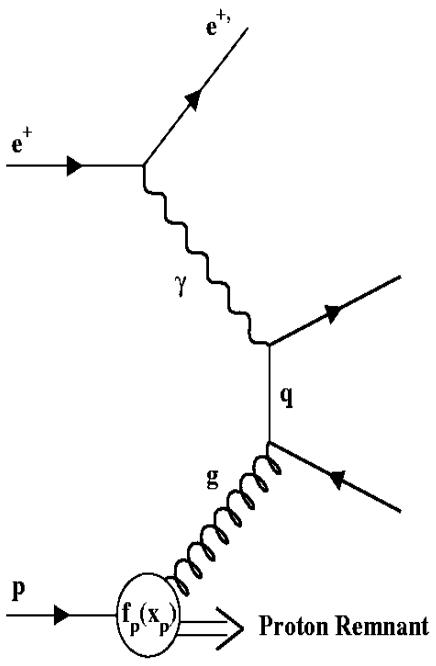


Figure 4.3: Example of a leading order Feynman diagram for direct photoproduction of quarks $\gamma g \to qq$.

The second process is resolved photoproduction. A parton from the photon interacts with a parton from the proton as seen in Fig. 4.4. The photon shows the behavior of a hadron, and acts as a source of partons. Only a fraction of the photon's 4-momentum is transferred. Resolved photoproduction has a "soft" component due to peripheral processes at low momentum transfer and a "hard" component from the scattering of a parton from the proton on a parton from the photon with high momentum transfer [57]. The resolved contributions are summed in the photon structure functions $F^{\gamma}$.

Direct and resolved hard photon processes give rise to quarks and gluons with large transverse momenta in the final state, which are observed as narrow jets of hadrons in the detector. The two jets have to balance in transverse momentum. The fractional momenta carried by the initial state partons in the photon, $x_{\gamma}$, and in the proton, $x_p$,

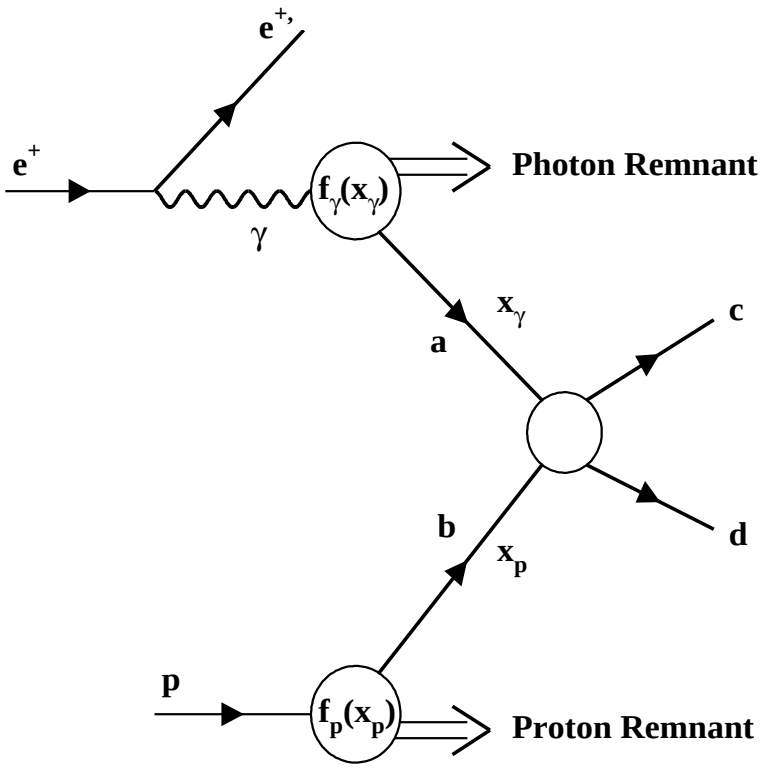


Figure 4.4: Example of a leading order Feynman diagram for resolved dijet photoproduction of quarks $qq \rightarrow qq$.

can be written as

$$x_\gamma = \frac{\sum_{partons} E_T^{parton} e^{-\eta^{parton}}}{2E_\gamma} \quad (4.38)$$

$$x_p = \frac{\sum_{partons} E_T^{parton} e^{\eta^{parton}}}{2E_p}, \quad (4.39)$$

where $E_T^{parton}$ and $\eta^{parton}$ are the transverse energy and the pseudorapidity of the outgoing partons. Events with $p_T < 1\,\mathrm{GeV}$ are defined as soft physics and events with $p_T > 1\,\mathrm{GeV}$ are considered hard physics. The following observables are used as experimental estimates of $x_\gamma$ and $x_p$

$$x_\gamma^{obs} = \frac{\sum_{jets} E_T^{jets} e^{-\eta^{jet}}}{2E_\gamma} \quad (4.40)$$

$$x_p^{obs} = \frac{\sum_{jets} E_T^{jets} e^{\eta^{jet}}}{2E_p}. \quad (4.41)$$

### 4.7.1 Photoproduced Dijets and OPE

The differential cross section for dijet events with a leading neutron $ep \to enX + 2jets$ using the OPE description can be written as

$$\frac{d\sigma^{ep}}{dE_T} = \int dy f_{\gamma/e}(y) \int dx_L f_{\pi/p}(x_L) \int dx_\pi^{obs} dx_\gamma^{obs} f_\pi(x_\pi^{obs}) f_\gamma(x_\gamma^{obs}) \frac{d\sigma}{dE_T}, \quad (4.42)$$

where $f_\pi$ represents the parton density in the pion, $f_{\pi/p}$ the pion flux from the proton and $\sigma$ is the hard scattering cross section. The neutron tagged dijets are a subset of all dijet events. In the OPE picture, the photon interacts with a pion and the neutron is produced, as seen in Fig. 4.5. The fraction of the pion momentum carried by the parton into the dijet production is estimated as

$$x_\pi^{obs} = \frac{E_p x_p^{obs}}{E_p - E_n} = \frac{x_p^{obs}}{1 - x_L} = \frac{\sum_{jets} E_T^{jet} e^{\eta^{jet}}}{2(E_p - E_n)}. \quad (4.43)$$

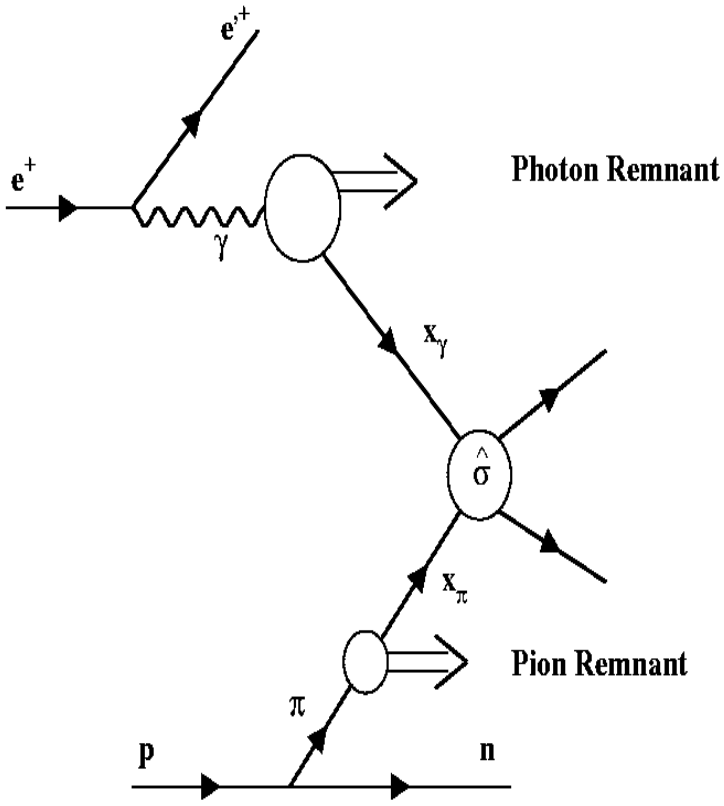


Figure 4.5: Resolved OPE dijet photoproduction.

## 4.8 Absorption

Neutron absorption can occur through rescattering of the neutron on the virtual photon. Since the size of the virtual photon falls like $Q^{-1}$, more neutron rescattering is expected for photoproduction than for DIS. The variation of the mean size of the $n$-$\pi$ system as a function of $x_L$ in exchange models leads to an $x_L$ dependence of the absorption. The data in this thesis are compared to two model calculations of absorption in the context of OPE.

### 4.8.1 The model of D'Alesio and Pirner

The absorption model of D'Alesio and Pirner [58], is based on the Meson Cloud Model (MCM) [59], [60], [61]. In the MCM the proton is seen as a bare proton surrounded by a cloud of virtual mesons.

The invariant differential cross section for OPE is given by D'Alesio and Pirner as

$$E_n \frac{d^3\sigma}{d^3p_n} = \frac{x_L}{\pi}\frac{d\sigma}{dx_L dp_T^2} \tag{4.44}$$

$$= \frac{2}{4\pi}\frac{g^2}{4\pi}\frac{1}{x_L(1-x_L)}\frac{m_N^2(1-x_L)^2+p_T^2}{(M_{N\pi}^2-m_N^2)^2}|G(x_L,p_T)|^2\sigma_{tot}^{p\pi}, \tag{4.45}$$

where $G(x_L, p_T)$ is the form factor extracted from Skyrme type models [62], [63] or from the light-cone or the covariant approach.

In this picture, a collision can be described by different impact parameters, as seen in Fig. 4.6. When $x_L$ is large, the pion and the neutron in the target proton are well separated and the impact parameter $b$ has a higher probability to be large. As shown in Fig. 4.6, the impact parameter $b$ describes the distance between the target proton (as a neutron-pion system) and the projectile $p$, which is a photon.

In Fig. 4.6 (a), the impact parameter is large. The $\pi$ is stripped and the neutron acts as a spectator. In the case of Fig. 4.6 (b), a more central collision takes place and the projectile $p$ can rescatter the neutron. The separation of the $n-\pi$ system , $b_{rel}$ (i.e., the distance between neutron and pion) depends on the flux factor used.

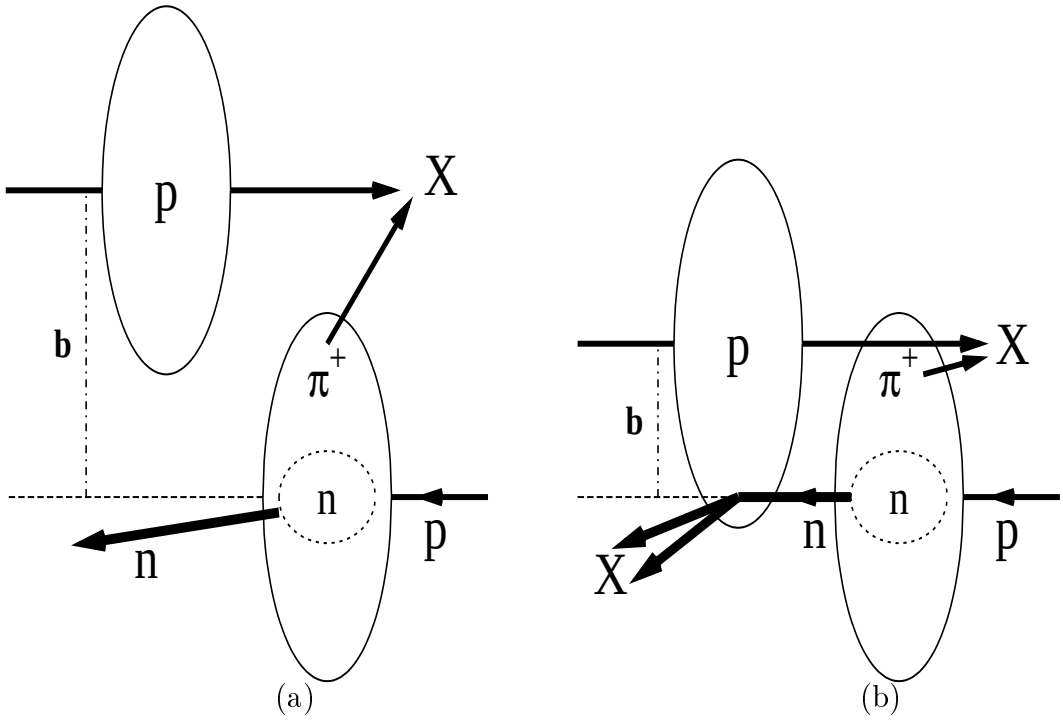


Figure 4.6: Picture of the collision for two different impact parameters. The projectile $p$ is a photon in the case of HERA.

Fig. 4.7 shows the density of the neutron-pion system for different form factors. The separation is larger at high $x_L$, so less rescattering of the neutron takes place. The resulting predictions of energy distributions of neutrons in DIS and PHP are shown in Fig. 4.8. Absorption decreases with increasing $x_L$ because the mean $n$-$\pi$ separation is increasing.

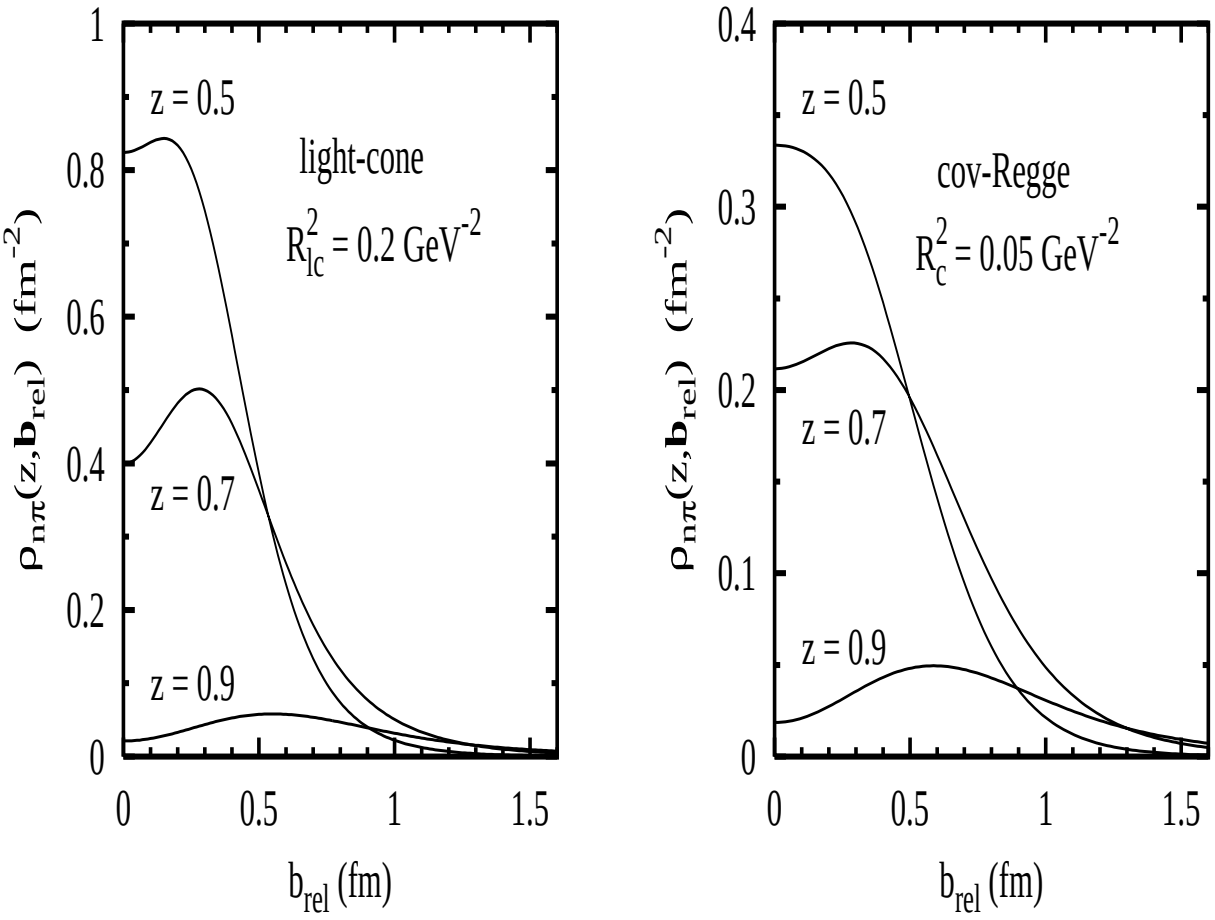


Figure 4.7: Pion-neutron densities for various $z\,(= x_L)$ values.

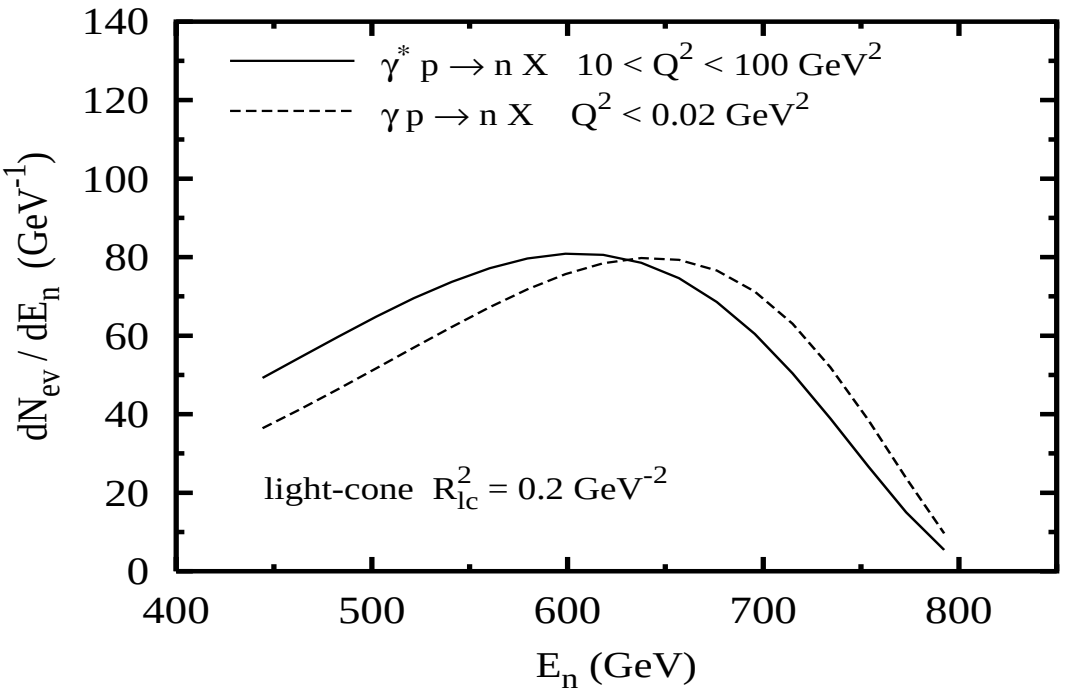


Figure 4.8: Comparison of the energy distributions of neutrons for DIS and PHP calculated by D'Alesio and Pirner.

### 4.8.2 The model of Nikolaev, Speth and Zakharov

In the absorption model of Nikolaev, Speth and Zakharov [64] a pion cloud around the proton is assumed as well. This model calculates initial and final state interaction effects, using the diagrams shown in Fig. 4.9, 4.10 and 4.11.

The optical theorem, which relates the total cross section $\sigma_{ab}$ for a two body process to the forward elastic scattering amplitude, is generalized to include one-particle inclusive reactions [65]. The total cross section for a one-particle inclusive interaction is related to the forward scattering amplitude for the three-body elastic scattering process. The generalized optical theorem relates Fig. 4.9 (a) to Fig. 4.9 (b). Fig. 4.10 shows the diagram that includes both $\pi$ and Pomeron exchange. The absorptive factor $K_{abs}$ is defined as

$$K_{abs} = \frac{(f_{\pi/p} + f_{abs})}{f_{\pi/p}}, \tag{4.46}$$

where $f_{abs}$ is the absorptive correction ([66], [67], [68], [69]). The effect of the absorptive strength $K_{abs}$ is approximately included in OPE by modifying the form factor $F_{abs}(t)$. As in the calculation of D'Alesio and Pirner, the absorption of a neutron is strong for impact parameter $b < R_p$ where $R_p$ is the radius of the proton. The size of the pion cloud around the nucleon is comparable to $R_p$.

Due to the impossibility to calculate the diagram in Fig. 4.10 exactly, the absorptive effects are calculated using Reggeon diagrams corresponding to Fig. 4.11(b) for the pion exchange mechanism. A Gaussian parameterization of the amplitude of elastic $a\pi$ scattering and a form factor $F(t) = \exp[R^2(t - m_\pi^2)]$ was used for the calculation. The absorptive factor $K_{abs}$ is shown in Fig. 4.12 for $pp$ and $\gamma p$ scattering to a final state $Xn$.

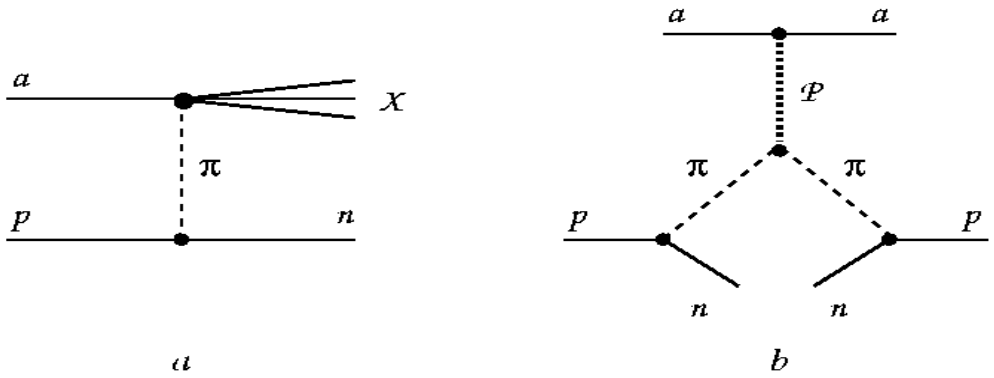


Figure 4.9: The pion exchange amplitude for the reaction $ap \to Xn$ and the corresponding triple Regge diagram.

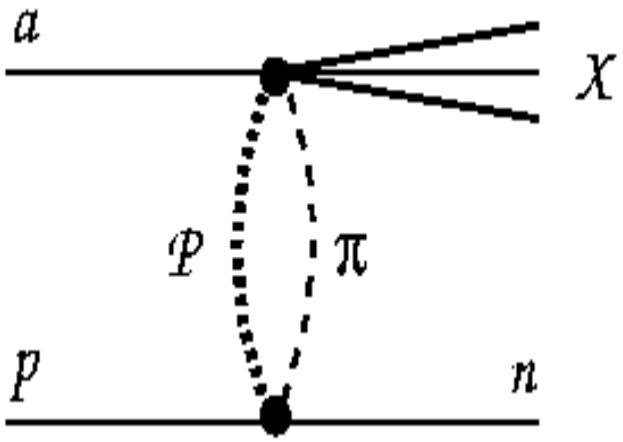


Figure 4.10: The absorptive $\pi$ exchange amplitude for the $ap \to Xn$ reaction.

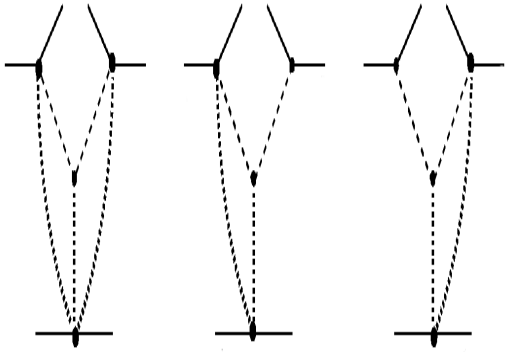

Figure 4.11: The triple Regge diagrams for absorption corrections corresponding to Fig. 4.10.

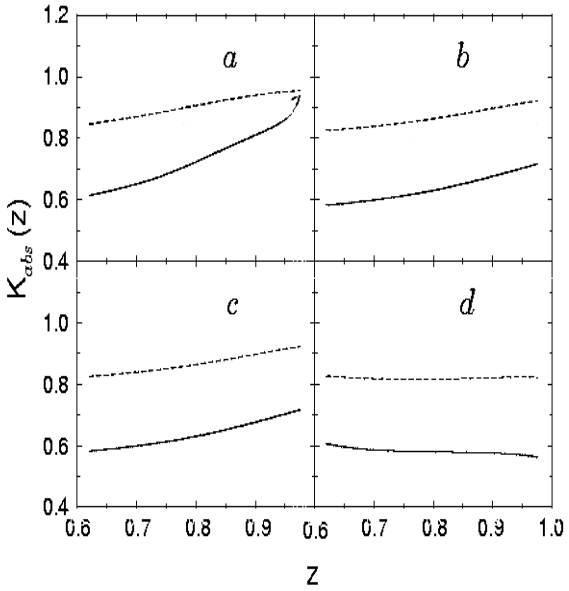


Figure 4.12: The absorptive $K_{abs}$ factor for (a) $p_T^2 = 0\,\mathrm{GeV}^2$, (b) $p_T^2 = 0.1\,\mathrm{GeV}^2$, (c) $p_T^2 = 0.2\,\mathrm{GeV}^2$ and (d) $p_t^2 = 0.3\,\mathrm{GeV}^2$ as a function of $z(= x_L)$. The solid lines give the values for $pp \to Xn$ at a center of mass energy of 400 GeV. The dashed lines show the predictions of the Reggeon calculus approach for $\gamma p \to Xn$.

# Chapter 5

# Kinematic Reconstruction

There are several methods to reconstruct the kinematic variables $Q^2$, $x$ and $y$.

## 5.1 Jacquet-Blondel Method

The Jacquet-Blondel (JB) method reconstructs kinematic variables from the hadronic final state [70], referred to here by the subscript $h$. This can be done in the ZEUS detector since it is nearly a $4\pi$ detector. However, a part of the hadronic information is lost through the forward beam hole, but the Jacquet-Blondel variables are not sensitive to this loss. However, they are sensitive to any energy lost by hadrons through the rear beam hole, but this is a small effect, since any such particles have very low energy. The variables $\delta_h$=($E_h$-$p_{z,h}$) and $p^2_{T,h}$ are determined as follows:

$$\delta_h = \sum_i (E_i - p_{z,i}) \tag{5.1}$$

$$p^2_{T,h} = (\sum_i p_{x,i})^2 + (\sum_i p_{y,i})^2, \tag{5.2}$$

where the sum is taken over each CAL cell i, but excluding cells associated with the scattered electron.

The kinematic variables are then:

$$y_{JB} = \frac{\delta_h}{2E_e} \tag{5.3}$$

$$Q^2_{JB} = \frac{p^2_{T,h}}{1 - y_{JB}} \tag{5.4}$$

$$x_{JB} = \frac{Q^2_{JB}}{s y_{JB}}. \tag{5.5}$$

## 5.2 Double Angle Method

The double angle (DA) method uses the measurement of the polar angle $\theta'_e$ of the scattered positron and the hadronic polar angle $\gamma_h$ [71]. The accuracy of angle measurements very often exceeds that of energy measurements, which is an advantage of the DA method. The DA method is less sensitive to radiative corrections as well. The angle $\gamma_h$ can be calculated from the hadronic system as:

$$\cos\gamma_{\rm h} = \frac{{\rm p}^2_{\rm T,h} - \delta^2_{\rm h}}{{\rm p}^2_{\rm T,h} + \delta^2_{\rm h}}. \tag{5.6}$$

The kinematic variables are then:

$$y_{DA} = \frac{\sin\theta_e(1+\cos\gamma_h)}{\sin\gamma_h + \sin\theta_e - \sin(\theta_e+\gamma_h)} \tag{5.7}$$

$$Q^2_{DA} = 4E_e^2 \frac{\sin\gamma_h(1+\cos\theta_e)}{\sin\gamma_h + \sin\theta_e - \sin(\theta_e+\gamma_h)} \tag{5.8}$$

$$x_{DA} = \frac{E_e\sin\gamma_h + \sin\theta_e + \sin(\theta_e+\gamma_h)}{E_p\sin\gamma_h + \sin\theta_e - \sin(\theta_e+\gamma_h)}. \tag{5.9}$$

## 5.3 Electron Method

The electron method uses the measured energy $E'$ of the electron and the polar angle $\theta'_e$. In this method, the kinematic variables can be expressed as [71]:

$$y_{el} = 1 - \frac{E'_e}{2E_e}(1-\cos\theta_e) \tag{5.10}$$

$$x_{el} = \frac{E_e}{E_p}\frac{E'_e(1+\cos\theta_e)}{2E_e - E'_e(1-\cos\theta_e)} \tag{5.11}$$

$$Q^2_{el} = 2E_eE'_e(1+\cos\theta_e). \tag{5.12}$$

# Chapter 6

# Event Sample

In this chapter, the data used for the analysis in this thesis are presented. Three different data sets are defined:

- DIS: a semi-inclusive deep inelastic scattering analysis data sample $ep \to enX$ with $Q^2 > 10\,\mathrm{GeV}^2$. The data were taken in 2000 in a run period which accumulated an integrated luminosity of 20.1 $\mathrm{pb}^{-1}$.
- PHP: a semi-inclusive photoproduction analysis data set $ep \to enX$ with $Q^2 < 4\,\mathrm{GeV}^2$. The integrated luminosity was 9.3 $\mathrm{pb}^{-1}$, since the trigger for photoproduction was not operational for the entire 2000 run period.
- PHP-dijet: a photoproduced dijet analysis sample $ep \to 2jets + enX$ with $Q^2 < 4\,\mathrm{GeV}^2$. The sample period corresponding to an integrated luminosity of 20.1 $\mathrm{pb}^{-1}$ as the DIS sample was used.

The online and offline selection used for DIS, PHP and PHP-dijet data are introduced and described. The last part of the chapter describes the final offline event selection cuts to ensure a clean neutron sample.

## 6.1 Trigger

To select events and reject background, the ZEUS three level trigger system was used as described in the Chapter 2, Section 2.2.6. Background can be synchrotron

radiation, proton beam interactions with the residual gas in the vacuum pipe, beam halo muons from decaying pions, protons or electrons interacting with beam line material, and cosmic rays.

## 6.2 DIS selection

### 6.2.1 FLT

The major task for the first level trigger (FLT) for DIS events was to select an electron in the calorimeter. Events pass the FLT when they fulfill one of the following requirements:

- an isolated electromagnetic deposit in the RCAL is found and:
  - the total energy deposit in the RCAL EMC $E_{RCALEMC} > 3.75\,\mathrm{GeV}$
  - the SRTD timing is consistent with an $ep$ interaction
- $E_{RCALEMC} > 3.4\,\mathrm{GeV}$ outside the cells around the beam pipe hole or both the energy in the BCAL EMC $E_{BCALEMC} > 4.8\,\mathrm{GeV}$ and a track is found in the CTD

  Events which occur outside the detector are removed using signals from upstream veto counters.

### 6.2.2 SLT

At the second level trigger level further energy and timing cuts filter out more background. The calorimeter timing is an average energy-weighted time of the forward and rear calorimeter cells. The DIS requirements in the SLT are:

- timing of the calorimeter:
  - $|t_{FCAL}| < 8\,\mathrm{ns}$ or $|t_{FCAL} - t_{RCAL}| < 8\,\mathrm{ns}$. The timing is set so that energy deposits from $ep$ events from the interaction point arrive at the FCAL and RCAL at 0 ns. Proton beam events have arrival times at the RCAL about 10 ns earlier.

  - cosmic muon events are rejected on the basis of a time difference between the upper and lower half of the calorimeter.

- static discharges of a PMT to its shielding are seen as an isolated energy deposit. Due to the large imbalance of energy in the cell produced by such an event (recall that each cell is viewed by two PMTs), they are easily identified and rejected.

- $\delta = E - p_z$ is calculated as the sum over all calorimeter cells assuming an interaction point at $x = y = z = 0$, i.e.:

$$\delta = \sum_i E_i(1 - cos\theta_i), \tag{6.1}$$

  where $\theta_i$ is the polar angle of each cell and $E_i$ the energy. Since $\delta$ is conserved by the interaction, $\delta = 2E_e = 55.2\,\mathrm{GeV}$ will be found for a fully contained event. Escaping particles through the forward beam hole contribute $\approx 0$ to $\delta$ (Note that $\delta$ is the JB variable defined in equation 5.1). A particle $k$ escaping through the rear beam hole, however, results in a loss to $\delta$ of $\approx 2E_k$. In DIS the loss is small, but in the case of photoproduction, the loss is large since the high energy scattered electron escapes through the rear beam hole. In order to remove photoproduction events from the DIS sample, the cut made is:

$$\delta' = \delta + 2E_{\gamma_{LUMI-\gamma}} > 29\,\mathrm{GeV}, \tag{6.2}$$

  where $E_{\gamma_{LUMI-\gamma}}$ is the LUMI photon tagger. Its energy is included to account for DIS events in which a photon is radiated from the initial state electron.

### 6.2.3 TLT

The TLT has the full event information. Calibrated detector information is available at this level and the full offline reconstruction code is used. For a DIS event the requirements are:

- $\delta < 100$ GeV

- $\delta' > 30$ GeV

- a positron with $E_{e'} > 4$ GeV is found by at least one of four independent positron finders

### 6.2.4 DIS Offline Cuts

All events passing through the trigger chain are written on tape for storage. They are analyzed using the full offline reconstruction software package with final calibration and corrections. Further information such as beam conditions, bad running periods, detector components offline and a bad readout channel list is also available. An event record containing the information needed to reconstruct the entire kinematics is stored in Data Summary Tapes (DSTs). The final event selection is made from the DSTs. For the DIS sample, the criteria were:

- the vertex $z$ position $-50\,\text{cm} < |z_{vertex}| < 100\,\text{cm}$

- identification of a positron (or electron) using SINISTRA, a neural network electron identifier. The probability has to be $P > 0.9$ and the energy has to be greater than 10 GeV.

- a "box cut" of 13 cm $\times$ 9 cm in $x \times y$ is made on the position of the scattered positrons on the face of RCAL. This cut is done to avoid energy degration due to shower leakage into the beam pipe hole.

- $y_{JB} > 0.2$ to ensure good resolution in the hadronic angle $\gamma_h$. The hadronic angle reconstruction resolution is very poor for events with a small amount of hadronic activity in the calorimeter, since the effects of the uranium noise in the calorimeter become significant.

- $y_{el} < 0.95$ to remove events in the forward calorimeter that have a misidentified positron. The main cause is an energetic photon from the decay of a $\pi^0$ produced in jet fragmentation. DIS positrons in the forward region are expected from very high $Q^2$ events. An electromagnetic cluster from a $\pi^0$ photon has an energy below that expected. Hence it has a very high value of $y_{el}$ and is removed by the cut.

- $38\,\text{GeV} < \delta = E - P_z < 70\,\text{GeV}$ is a cut around the nominal value of 55 GeV for a fully contained DIS event.

## 6.3 PHP

### 6.3.1 FLT

The FLT requires for a PHP event:

- an energy deposit in the LUMI-e detector $E_e > 5\,\text{GeV}$
- $E_{RCAL\,EMC} > 0.464$ GeV, outside the cells around the beam pipe hole or $E_{RCAL\,EMC} > 1.250\,\text{GeV}$
- energy deposit in the FNC $E_{FNC} > 180\,\text{GeV}$

### 6.3.2 SLT

In PHP events the positron scatters at a very small angle and escapes through the rear beam hole. This results in $\delta = 2(E_e – E_{e'})$, leading to a cut rejecting DIS events:

- $\delta_{SLT} + 2\ E_{LUMI-\gamma} < 29$ GeV, with $E_{LUMI-\gamma}$ the energy deposit in the LUMI-$\gamma$ detector.

### 6.3.3 TLT

The TLT requirement is:

- a vertex is found and $-66\,\text{cm} < z_{vertex} < 66\,\text{cm}$, that the vertex origin is no more than 66 cm away from the ZEUS interaction point

### 6.3.4 Photoproduction Offline Cut

The only extra offline cut required is:

- Lumi-$\gamma < 1\,\text{GeV}$

## 6.4 PHP-dijet

### 6.4.1 FLT

The major criteria for passing the FLT for PHP-dijet events are:

- $E_{BCALEMC} > 3.4\,\text{GeV}$
- $E_{RCALEMC} > 2.0\,\text{GeV}$, outside the cells around the beam pipe hole
- total transverse energy $E_T > 11.6\,\text{GeV}$, excluding the forward pipe region
- total EMC energy deposit $E_{EMC} > 10\,\text{GeV}$, excluding the forward pipe region
- the total energy deposited in the calorimeter $E_{CAL} > 15.0\,\text{GeV}$

### 6.4.2 SLT

The SLT requirements for photoproduced dijet events are the same as for PHP events.

- $\delta_{SLT}+2\ E_{LUMI-\gamma} < 29$ GeV, with $E_{LUMI-\gamma}$ the energy deposit in the LUMI-$\gamma$ detector.

### 6.4.3 TLT

For a PHP-dijet event it is required that

- at least 2 jets were found using a cone algorithm with radius 1.0 (i.e., jet energy is found within a cone radius $\sqrt{\eta^2+\phi^2} = 1$), each with $E_T^{jet} > 3.0\,\text{GeV}$ and pseudorapidity $|\eta^{jet}| < 2.5$

### 6.4.4 PHP-dijet Offline Cuts

The photoproduced dijet events were selected using variables calculated with the reconstructed vertex position of the interaction point and the energy deposits in the calorimeter. Events with an electron in the CAL were removed, so that $Q^2 < 4\,\text{GeV}^2$. Dijet events were required to have at least two jets, each having

$$E_T^{jet} > 5\,\text{GeV} \tag{6.3}$$

$$|\eta^{jet}| < 2. \tag{6.4}$$

Finally, the photon-proton center-of-momentum energy was restricted to

$$135\,\mathrm{GeV} < \mathrm{W} < 265\,\mathrm{GeV}. \tag{6.5}$$

## 6.5 Final Event Selection for Neutrons

The event selection above ensured clean samples in the main ZEUS detector. Further cuts were introduced to ensure that the particles incident on the FNC and FNT were neutrons.

### 6.5.1 FNC Energy Cut

The neutron energy spectrum is limited to

$$x_L > 0.2 \quad . \tag{6.6}$$

### 6.5.2 Maximum Energy Position Cut

To ensure that a particle incident on the FNC is approximately within ± 10 cm in $y$ from the zero degree axis, a cut on the number of the tower with the highest deposited energy is made:

$$5 < TWR_{max} < 10. \tag{6.7}$$

### 6.5.3 Electromagnetic Showers caused by Photons

Electromagnetic showering of photons causes a much narrower shower than the neutron showers and tend to be completely concentrated in one tower. These events are removed using a parameter

$$\gamma_{tag} = \frac{E_{TWR_{max}} + E_{N_{TWR}}}{\sum_{TWR=1}^{10} E_{TWR}}, \tag{6.8}$$

where $E_{N_{TWR}}$ is the energy of the tower with the next-to-maximum energy. Fig. 6.1 shows the $\gamma_{tag}$ distribution. The peak close to $\gamma_{tag} = 1.0$ is due to photons. A cut is made at

$$\gamma_{tag} < 0.92. \tag{6.9}$$

### 6.5.4 Shower Size

Due to the vertical FNC segmentation, the RMS shower width in the $y$-direction can be calculated as

$$Y_{width} = \sqrt{\frac{\sum_{TWR=1}^{10} E_{TWR} \cdot y_{TWR}^2}{\sum_{TWR=1}^{10} E_{TWR}} - y_{TWR_{max}}^2}, \tag{6.10}$$

where $E_{TWR}$ is the energy measured in a tower of the FNC and $Y_{TWR}$ is the $y$ position of the center of this tower. Only the towers in the front bottom part of the FNC are

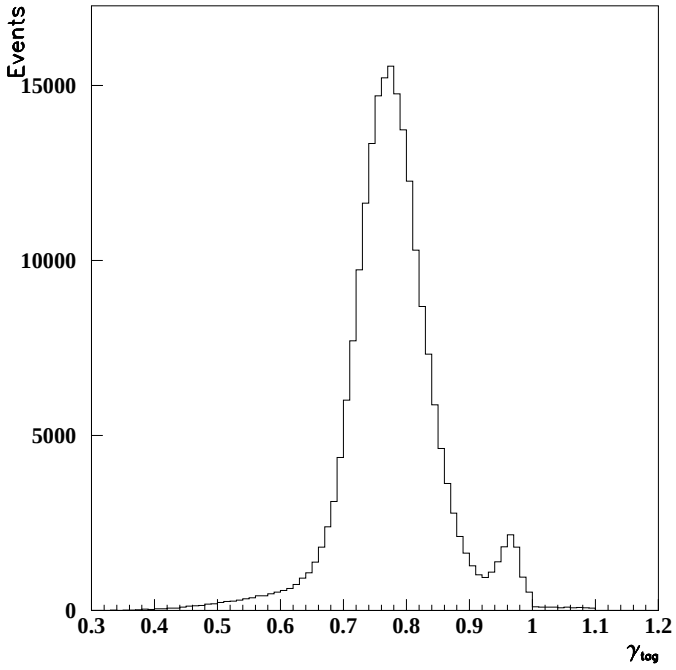


Figure 6.1: The distribution of the $\gamma_{tag}$, after a cut on the energy of the veto counter.

taken into account, since they contain approximately 90% of the energy of a shower. Figure 6.2 shows the $Y_{width}$ distribution for an FNC event sample. The tail is due to particles whose showering is spread out across the FNC surface. A cut is made at

$$Y_{width} < 8.0\,\text{cm} \tag{6.11}$$

to eliminate this tail due to neutrons showering in front of the FNC.

### 6.5.5 Veto Cut

Any charged particle hitting the FND is due to an interaction downstream from the bending magnets in the proton beam. Events with charged particles are rejected by the veto counters. Fig. 3.2 shows the veto counter position in front of the FND. A cut is made at

$$E_{veto} < 0.8\,\text{MIPs}. \tag{6.12}$$

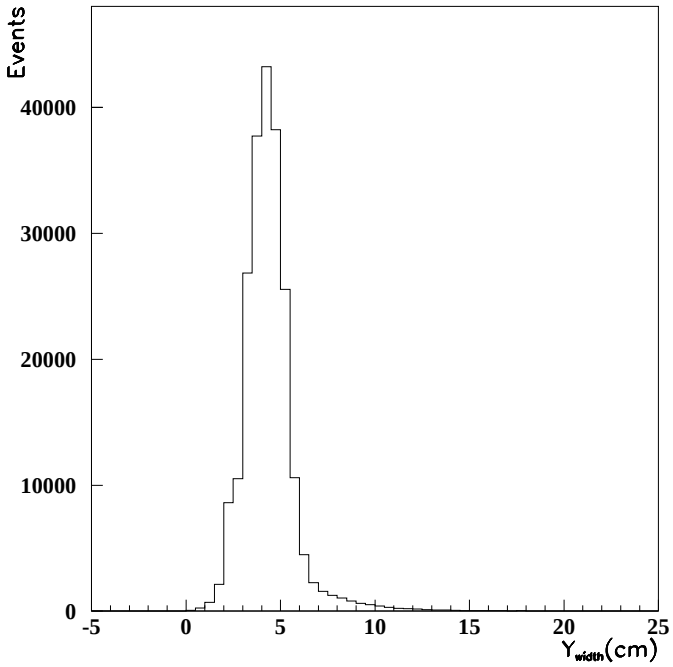


Figure 6.2: The distribution of $Y_{width}$

### 6.5.6 Energy Cut and Clean Shower Cuts in the FNT

In order to select neutrons which shower within the first interaction length, a cut is made on the deposited energy $E_{x_{FNT}}$ and $E_{x_{FNT}}$ in the $x$ and $y$ plane of the FNT. Very low energy deposits indicate that particles have not yet showered. The required cuts are

$$E_{x_{FNT}} > 3\,\mathrm{pC} \tag{6.13}$$

$$E_{y_{FNT}} > 3\,\mathrm{pC}. \tag{6.14}$$

Fig. 6.3 shows the energy distribution in the FNT $x$ plane after the neutron FNC and FNT cleaning cuts. To ensure that there is a well collimated shower in the FNT, the FNT fingers with the highest energy deposit per event and the finger with the second highest energy deposit are required to be adjacent in each plane:

$$|(n^{FNT}_{x,max} - n^{FNT}_{x,max2}| < 2 \tag{6.15}$$

$$|(n^{FNT}_{y,max} - n^{FNT}_{y,max2}| < 2. \tag{6.16}$$

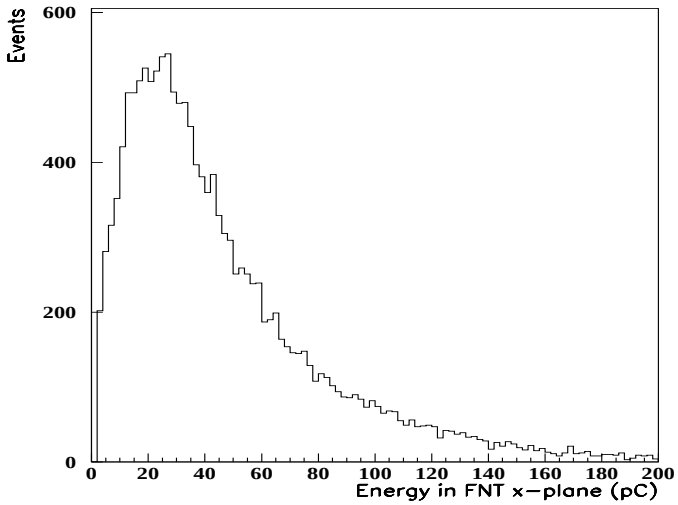


Figure 6.3: Energy in the FNT $x$ plane after neutron FNC and FNT cleaning cuts.

# Chapter 7

# Alignment

To measure the angular distribution of leading neutrons, the determination of the zero degree point $(x_0, y_0)$ relative to the FNT is essential and is the most critical undertaking. Three methods to determine the zero degree point are taken into consideration. The position of the components of the proton beam line can be seen in Figure 7.1. The procedure is complicated by the fact that even inside the geometric aperture, there is inactive material. Mapping this material is important in order to fully understand the angular dependence. Figure 7.2 shows the $x, y$ reconstruction of neutron events in the FNT. The curve outlines the geometric aperture as defined in the ZEUS detector simulation package. There is a band in $y$ around 3 cm where there is a depletion of events. It is caused by a RF-shield made of steel in station 6 of the LPS detector, as discussed in section 7.2.

## 7.1 Sliding Disk Method

In this method, a disk with a radius of 2.3 mm, the FNT position resolution, is moved systematically over the area of the geometric aperture in small steps and the number of events inside the circle is counted. This method gives an idea of the neutron distribution and where dead material might be encountered. Fig. 7.3 shows the result of such a counting in a three dimensional projection. Fig. 7.4 shows a two dimensional projection with different shades giving a scale for the number of events counted. The zero degree point is determined when the event count is maximum, indicating that

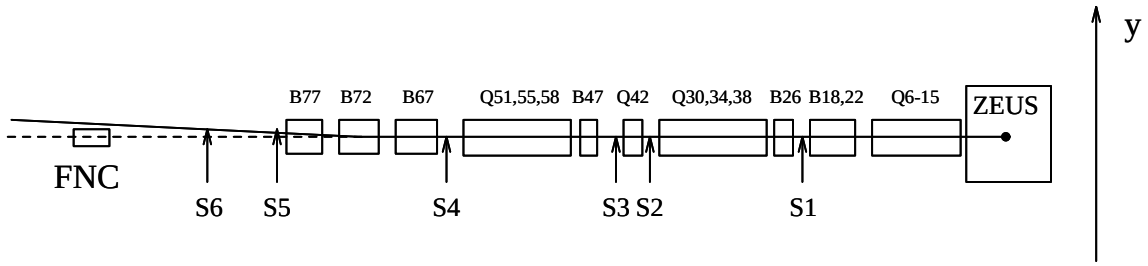


Figure 7.1: The positions of the components of the proton beam line in the HERA tunnel. Components labeled with a Q are quadrupole magnets, components labeled with a B are dipole bending magnets. The numbers give the approximate distance of each component from the ZEUS interaction point in meters.The arrows labeled S1-S6 indicate the LPS station positions and their number. The dashed line shows the zero degree line. The solid line indicates the proton beam, which is bend upwards by dipoles B67, B72 and B77.

the disk is centered on the peak of the neutron distribution. Due to the radius of the sliding disk, the error for the peak finding in this method is larger than 5 mm. To reduce the error on the position measurement, the sliding disk has to be made smaller. The statistics of the measurement decrease too fast to make the disk smaller, the error can not be further reduced in this method.

While this method does not provide detailed information about the position of inactive material, it shows whether the beam spot is moving or stable over a long period of time. The LPS provides a better handle on whether the beam conditions are stable or not. The LPS determines the momentum components $p_x$ and $p_y$. From this information it is possible to calculate the beam position at the FNC. Unfortunately, the zero degree line determined by the LPS itself cannot be used because there is an unknown offset between the LPS and the FNT detectors. Fig. 7.5 shows a plot of the projection of the zero degree line determined by the LPS $y$ beam spot position on the front of the FNC as a function of time and Fig. 7.6 shows the projection of this plot. The proton beam is stable with a RMS deviation of less than 2 mm. Fig. 7.7 compares now the beam spot of the neutron distribution in the FNT, as determined by the sliding disk method, with the measurement of the LPS proton beam spot po-

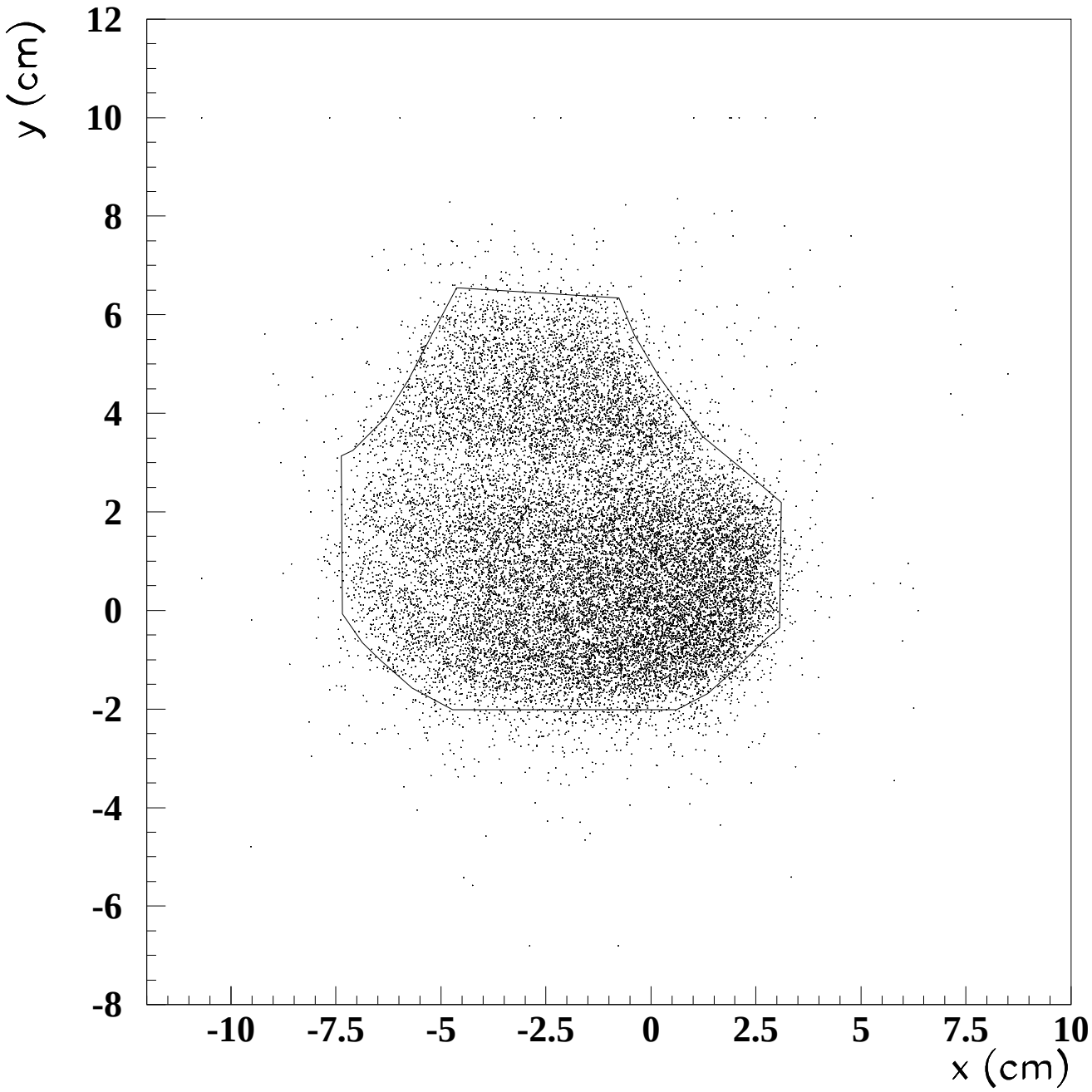


Figure 7.2: The reconstructed $x, y$ position of neutron events in the FNT in the ZEUS coordinate system. The geometric aperture is clearly visible, as well as missing events inside the geometric aperture due to absorbing material inside the geometric aperture. The curve outlines the geometric aperture as predicted by the ZEUS detector simulation.

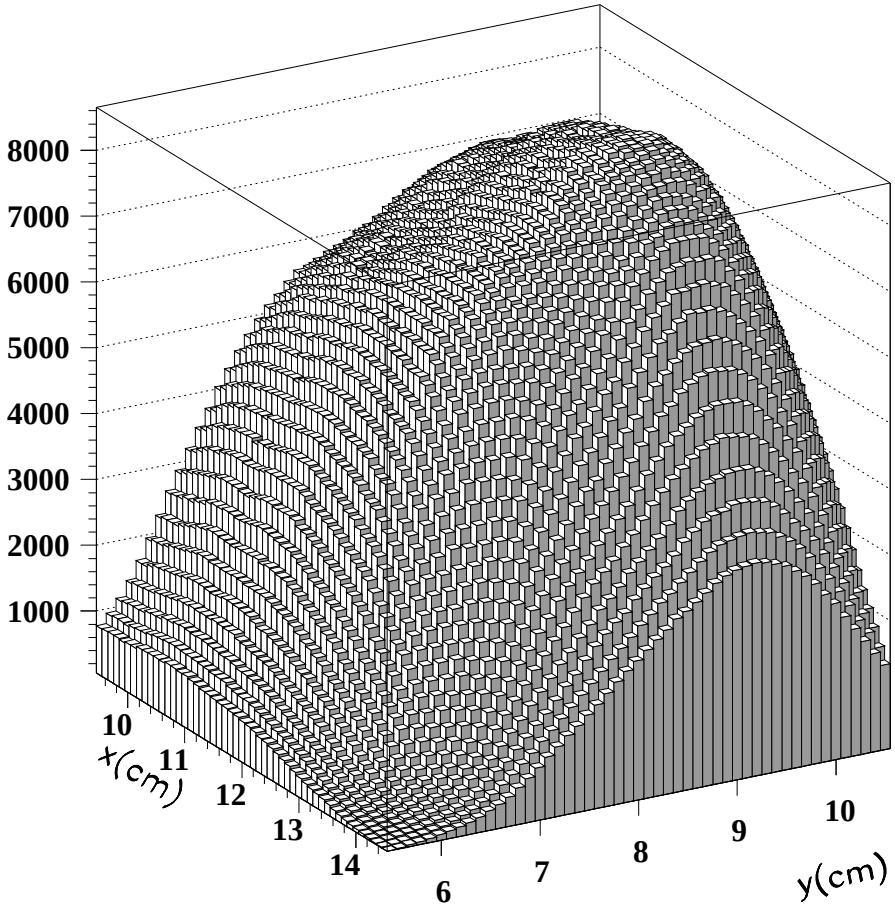


Figure 7.3: The $x, y$ distribution of number of neutron events detected in the FNT as counted by the sliding disk method.

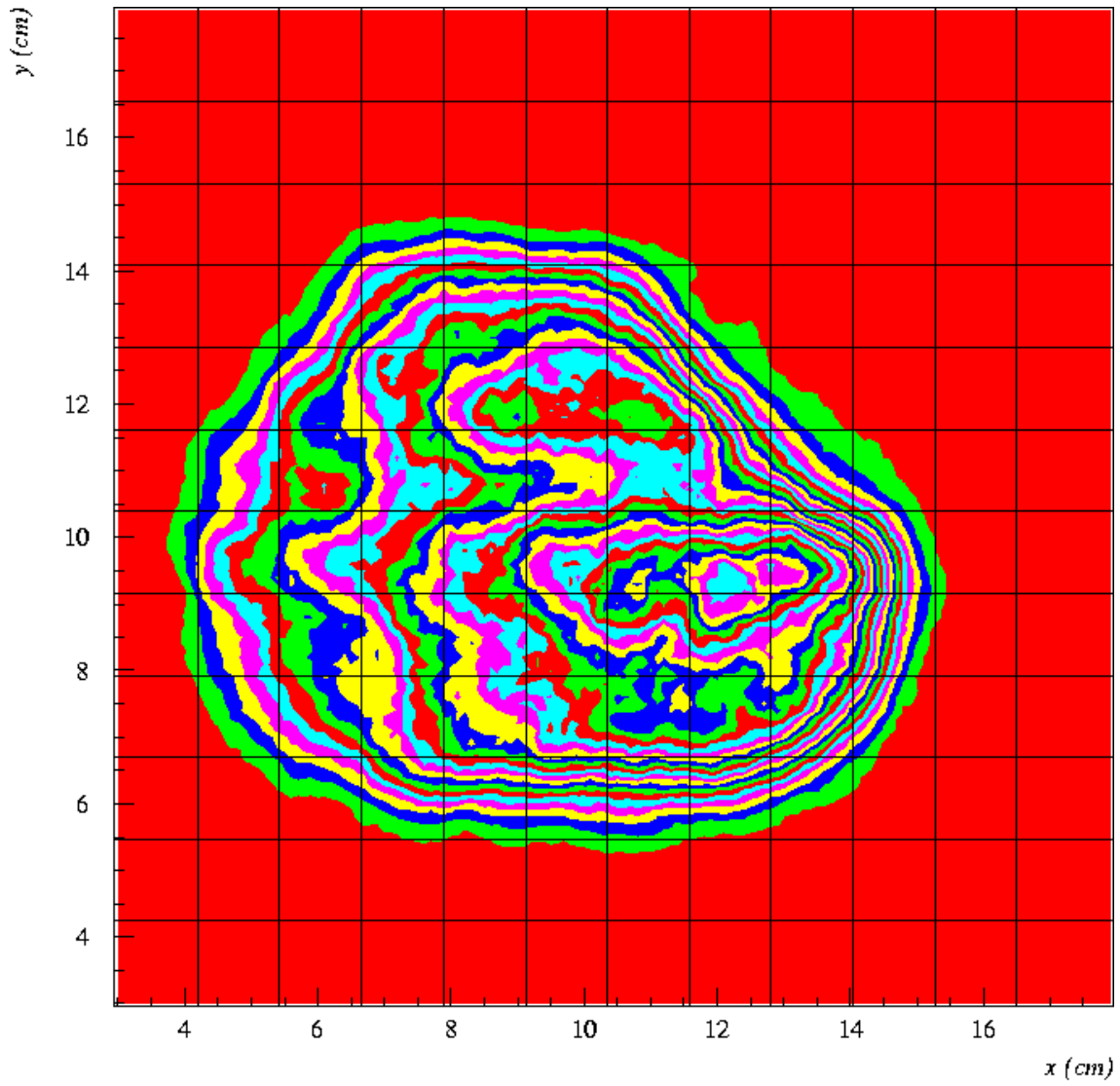


Figure 7.4: The $x, y$ distribution of number of neutron events detected in the FNT as counted by the sliding disk method with respect to the FNT hodoscope. The lines mark the borders between the FNT scintillator fingers.

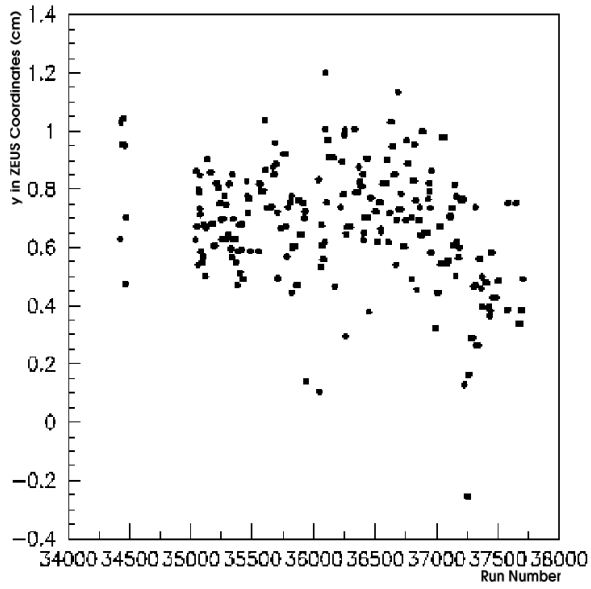


Figure 7.5: Scatter plot of the projection of the LPS $y$ beam spot position on the front of the FNC versus time. Time is given as run number.

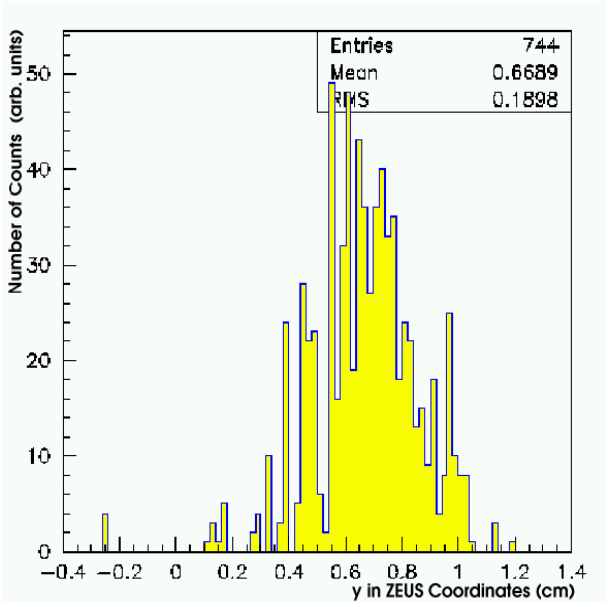


Figure 7.6: Distribution of the projection of the y position on the front of the FNC of the LPS beam spot. Note that there is an unknown arbitrary offset between LPS and FNT coordinate systems.

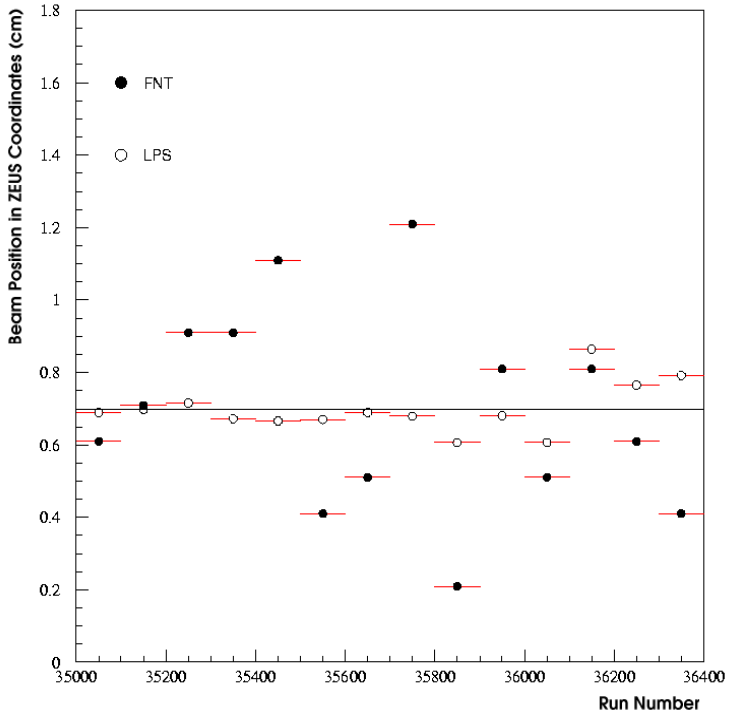


Figure 7.7: Comparison of spread of LPS beam position and FNT beam position measurement for a longer run range. The position of the LPS beam spot is very well evaluated. The comparison shows that the FNT beam spot is as well stable to a few mm. The line indicates the mean value of the FNT beam spot measurement.

sition projected onto the FNC as a function of time. This comparison shows that the neutron beam spot is as well stable to a few mm. This leads to the conclusion, that once the zero degree point is found it can be used for the whole run range and need not to be evaluated for every run or a small run range. This provides a tremendous statistical advantage.

## 7.2 Monte Carlo Method

Another, more precise, way to evaluate the zero degree position is provided by the comparison of the data with a generated Monte Carlo sample. For this a good knowledge of the inactive material is essential. The inactive material inside the geometric aperture is mostly due to LPS station 6, and it has been modeled in detail in the Monte Carlo. Figure 7.8 shows the material seen by neutrons inside the geometric aperture projected to the FNT position. The MC simulation takes into account the geometric aperture including inactive material inside, the proton beam divergence (100 MeV in $x$, 50 MeV in $y$), the FNT position resolution and the FNC energy resolution, and uses a parameterization of the observed $x_L$ spectra. The generated events are subjected to the same cuts as the data. The procedure to find $x_0, y_0$ is iterative:

1. Start with arbitrary $p_T^2$ distributions of the neutrons and produce Monte Carlo samples with a range of $x_0, y_0$ positions.

2. Compare MC to data and determine $x_0$ and $y_0$ in the FNT. To do so, the $x$ or $y$ FNT position reconstruction distribution was compared to the Monte Carlo reconstruction distribution for a range of theoretical $x_0$ and $y_0$ positions in the FNT. This is illustrated in Figs. 7.9 and 7.10. The positions with the lowest $\chi^2$ were used as new $x_0$ and $y_0$ values.

3. Calculate $p_T^2$ distributions from the data with newly obtained $x_0$ and $y_0$ values.

4. Go back to step 2 with the new $p_T^2$ distributions.

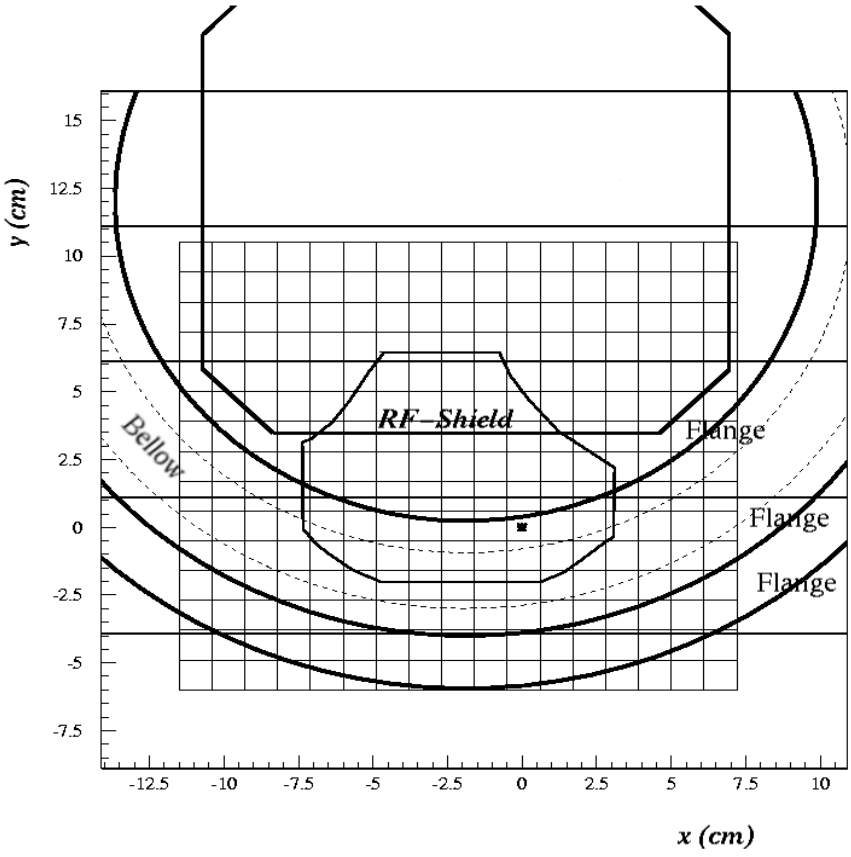


Figure 7.8: Position of dead material inside the geometric aperture as projected on the FNT. The open circles are the position of the outer limits of flanges and the wall of the vacuum chamber of the LPS Roman Pot.

5. Stop when the change in $x_0$, $y_0$ position in the FNT is smaller than the estimated error of the method.

Figures 7.11 and 7.12 show the $\chi^2$ evaluation for the data/MC reconstruction comparison. The lowest $\chi^2$ value marks the zero degree position of the neutron beam. At this point the $\chi^2$/DOF $\approx 1$. The error on the beam position is determined from the position where the $\chi^2$ is increased by 1 from the minimum value. The error is 0.1 cm for both $x_0$ and $y_0$.

## 7.3 Comparison of $p_x^2$ and $p_y^2$

Another method to evaluate the zero degree position of the neutron beam is using the assumption that the transverse momentum distributions for $p_x^2$ and $p_y^2$ in bins of $x_L$ after correction for the inactive material and beam tilts should be the same. Assuming an $x_0, y_0$ position, $p_x^2$ and $p_y^2$ were extracted by bin-by-bin unfolding as described below in section 7.4. The different beam divergences in $x$ and $y$ were accounted for in the Monte Carlo simulation. A $\chi^2$ comparison of the $p_x^2$ and $p_y^2$ distributions will show a minimum at the correct zero degree point in $x$ and $y$. Figures 7.13 and 7.14 shows the $p_x^2$ and $p_y^2$ distribution in increasing $x_L$ bins at the $(x_0, y_0)$ position. The result of this method agrees within 1 $\sigma$ with the result of the previous Monte Carlo method.

## 7.4 Bin-by-Bin-Unfolding

The finite resolution and the limited acceptance of the neutron detector make it necessary to correct for smearing, migration and acceptance, since even after background subtraction, the measured distribution differs from the true distribution. This correction procedure is called unfolding or deconvolution. The relation between the true variable $x$ distribution $f$ and the measured variable $y$ distribution $g$ is

$$g(y) = \int A(y,x) f(x) dx, \tag{7.1}$$

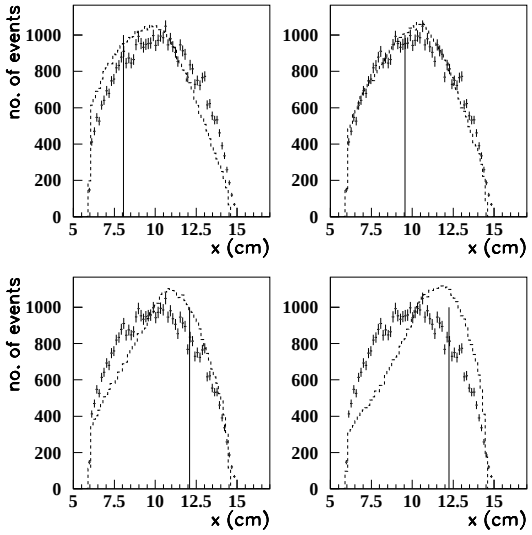


Figure 7.9: Zero degree determination for the FNT $x$ coordinate by comparison of MC and data. The points with errors represent the data, the dashed line the MC simulation and the vertical line the position of the zero degree point. The $x$ coordinate is in the local FNT coordinate system.

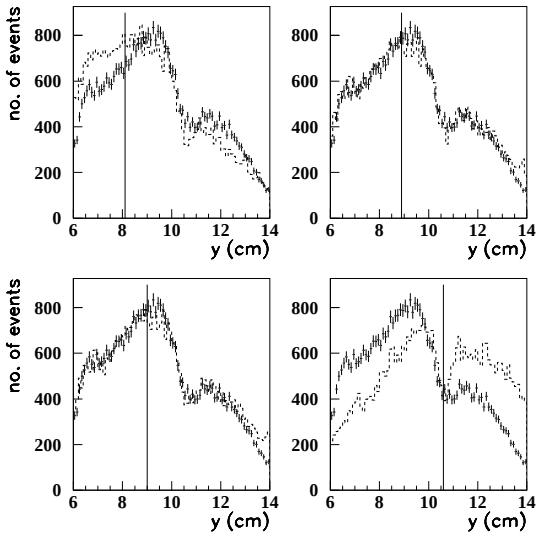


Figure 7.10: Zero degree determination for the FNT $y$ coordinate by comparison of MC and data. The points with error bars represent the data, the dashed line the MC simulation and the vertical line the position of the zero degree point. The $y$ coordinate is in the local FNT coordinate system.

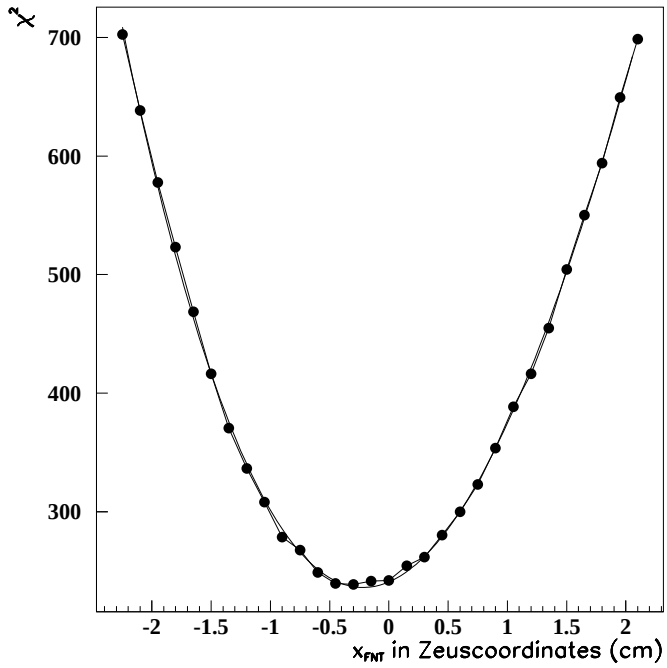


Figure 7.11: Best $\chi^2$ fit for the $x$ reconstruction comparison along the minimum $y$ $\chi^2$ value.

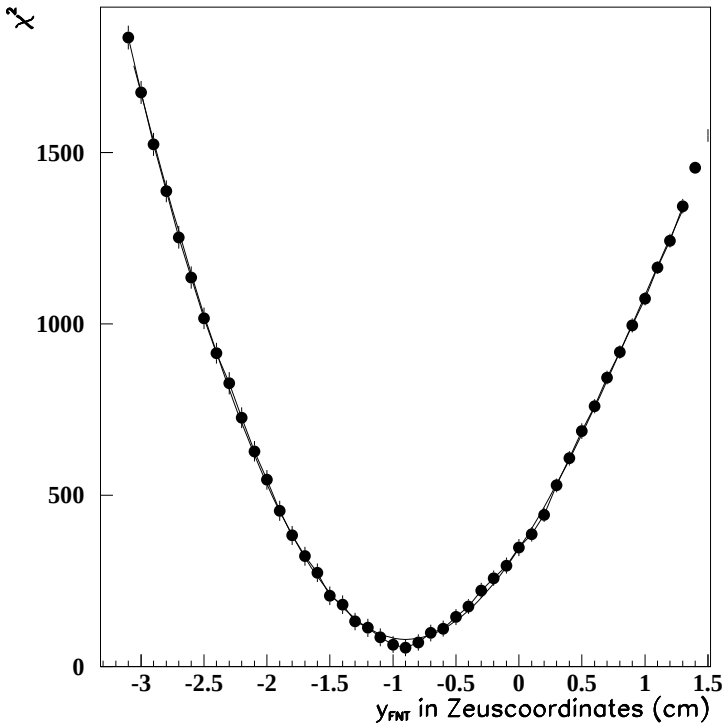


Figure 7.12: Best $\chi^2$ fit for the y reconstruction comparison.

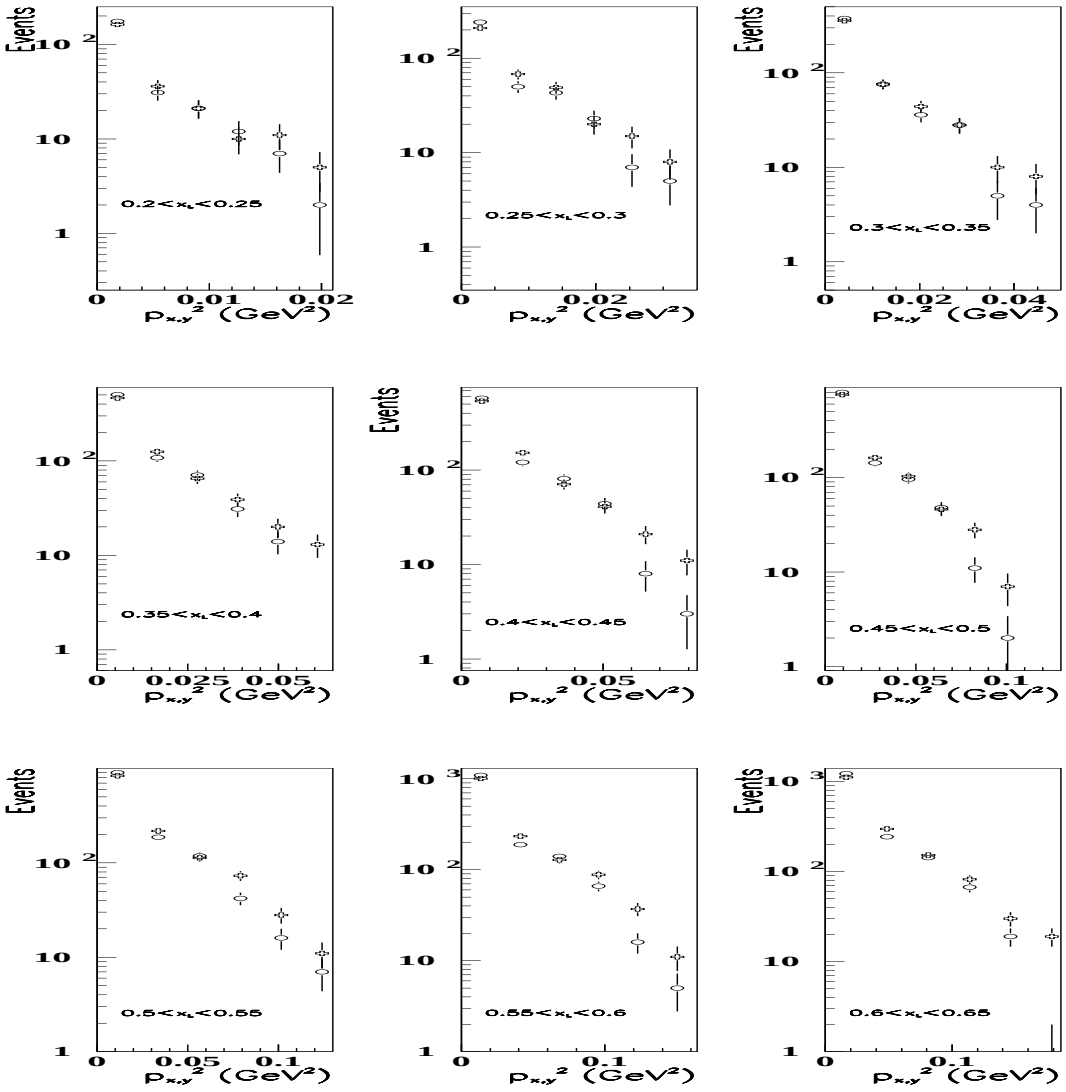


Figure 7.13: The $p_x^2$ and $p_y^2$ distributions in bins of $x_L$ for the $x_0, y_0$ position which gives a best match.

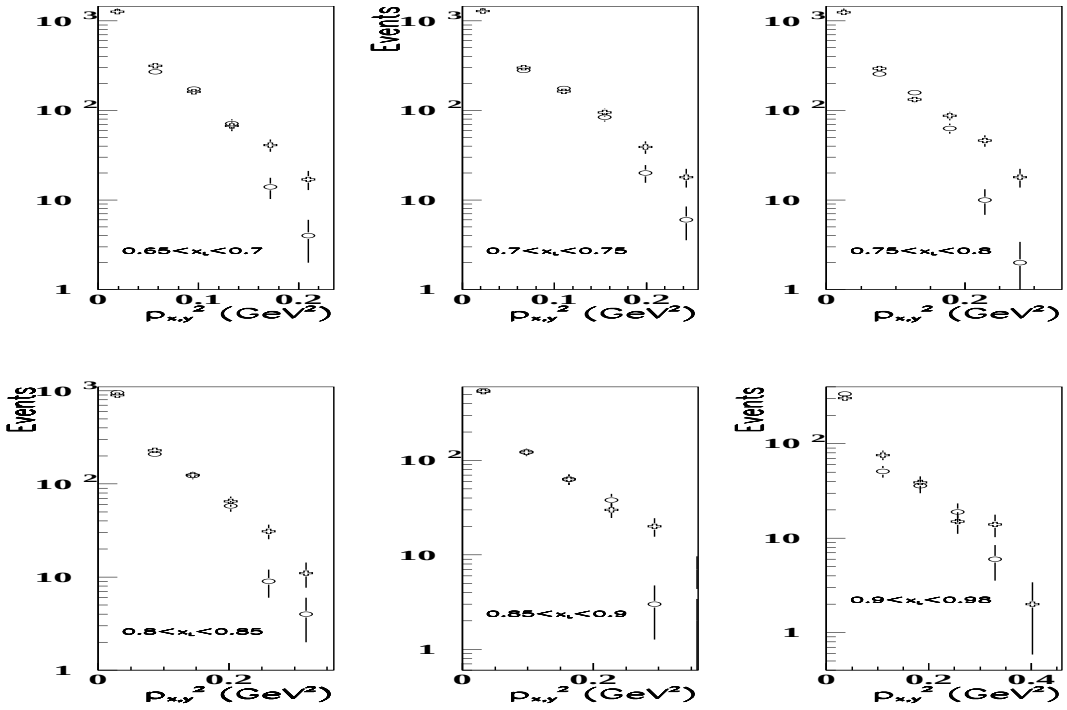


Figure 7.14: The $p_x^2$ and $p_y^2$ distributions in bins of $x_L$ for the $x_0, y_0$ position which gives a best match.

where A(x,y) is the so called transfer function or resolution function. It represents the effects of the detector. The determination of the distribution f(x) from g(y) is the unfolding process. The distributions in this thesis are represented by histograms. The transfer function can be represented by a matrix. Equation 7.1 is written in matrix form as

$$\mathbf{y} = \mathbf{A}\mathbf{x}. \tag{7.2}$$

This equation can be solved for the vector $\mathbf{x}$ given vector (histogram) $\mathbf{y}$ and the matrix $\mathbf{A}$, which describes the transition from $\mathbf{x}$ to $\mathbf{y}$ . Each element of the matrix $\mathbf{A}$ describes the probability of observation of an entry in histogram bin $j$ of the histogram $\mathbf{y}$ , if the histogram bin $i$ of histogram $\mathbf{x}$ is the true value.

In most high energy physics experiments, the resolution function is not known analytically. However, it can be represented by data from Monte Carlo simulations using the relation

$$\frac{Data_{true}}{Data_{observed}} = \frac{MC_{true}}{MC_{observed}} \tag{7.3}$$

and

$$g_i = g_{MC} = \int A(y,x)f(x)dx = \frac{a_i^{MC}}{a_i^{Data}} f_i. \tag{7.4}$$

When the measurements y are close to the the true values x, the bin-by-bin-unfolding can be utilized and $a_i^{Data} = a_i^{MC}$. The bin-by-bin unfolding replaces the transfer matrix by a simple diagonal matrix. Each bin is uncorrelated to the other bins of the histogram and has its own correction factor

$$\frac{1}{a_i} = \frac{\#\text{of generated events in bin i(true)}}{\#\text{events measured in bin i}}. \tag{7.5}$$

This correction is calculated from the Monte Carlo simulation. This leads to the true number N(corrected) of data events by the unfolding equation

$$N_{corrected}^{data} = \frac{1}{a_i} n_i^{data} \tag{7.6}$$

with

$$g_{MC} = g_{Data}. \tag{7.7}$$

## 7.5 Final Values of the Zero Degree Determination

The final values for the determination of the zero degree point of the neutron distribution measured by the FNT, using the method of comparing $p_x^2$ and $p_y^2$, are (in ZEUS coordinates):

$$x_0 = -0.3\,\text{cm} \pm 0.1\,\text{cm} \tag{7.8}$$

$$y_0 = -0.4\,\text{cm} \pm 0.1\,\text{cm} \tag{7.9}$$

# Chapter 8

# Systematic Uncertainties

There are two dominant sources of systematic errors, which apply to all the results in the following chapters:

- The uncertainty in the absolute energy scale of the FNC. It was estimated to be $\pm 2\%$ from the calibration and confirmed by the Kolmogorov test in section 3.2.
- The uncertainty in the geometrical acceptance and finding the zero degree point. This includes the systematic uncertainty in the position of the inactive material. The uncertainty in the position of the beam spot is $\Delta x = \pm 0.1\,\mathrm{cm}$, $\Delta \mathrm{y} = \pm 0.1\,\mathrm{cm}$, as determined in Chapter 7.

The systematic errors were obtained by varying the energy scale (see Fig. 8.1) and the beam position by their errors in each direction and the resulting errors were added in quadrature. The sensitivity to the energy scale error at high $x_L$ is very large, so a cut

$$x_L < 0.92 \tag{8.1}$$

was introduced.

There are other systematic errors which are negligible compared to these two, such as the trigger efficiency of the FNC. It was close to 100% for the energy range under consideration and is therefore not considered in calculating systematic errors.

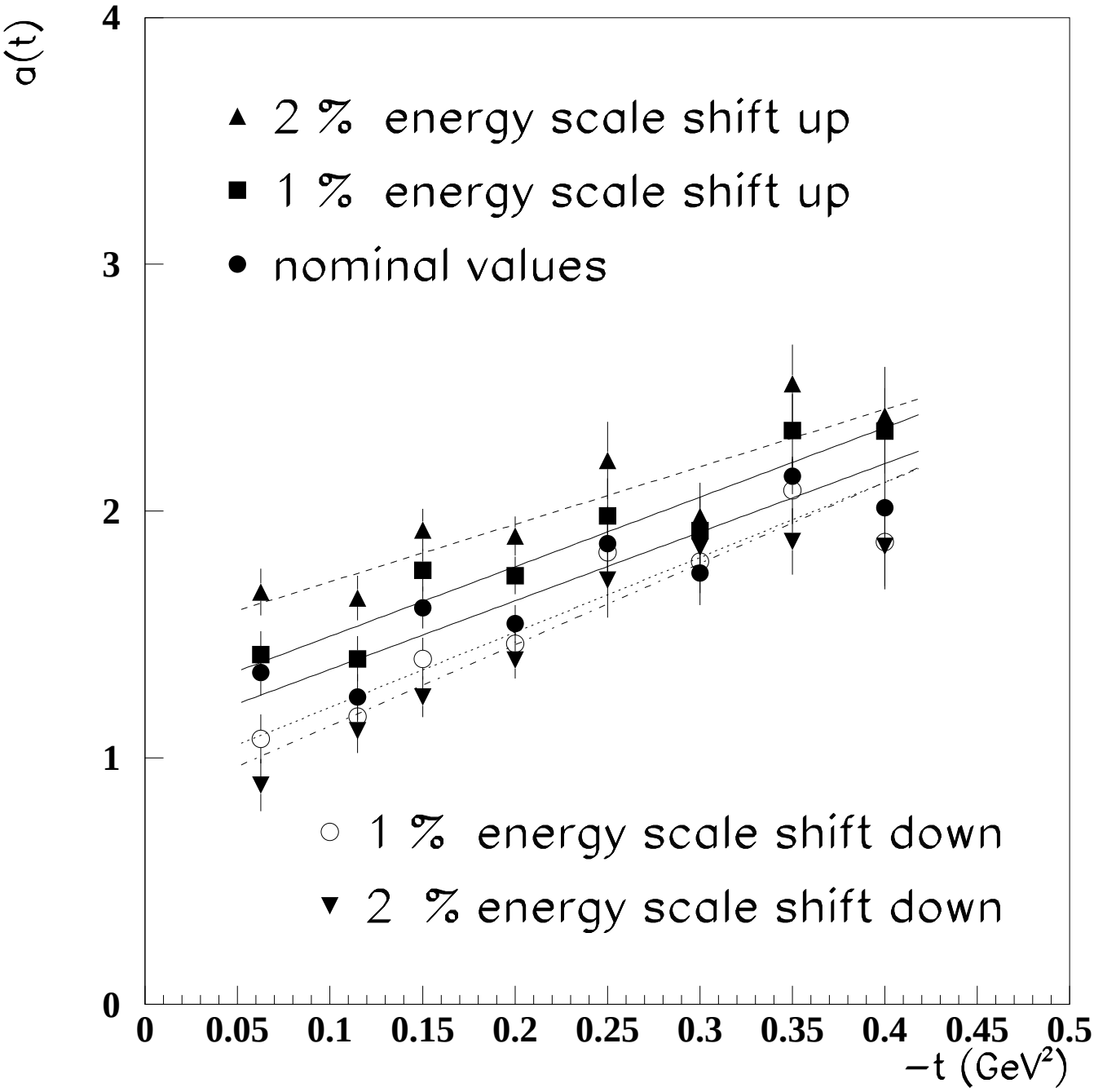


Figure 8.1: Variation of the energy scale ±1% and ±2% in the trajectory analysis of Chapter 10.

## 8.1 Validation of Systematic Uncertanties

A check of the systematic errors was made by comparing the results obtained by the bin-by-bin unfolding method used in this thesis (Method 1) and another independent method (Method 2) described below.

The efficiencies and correction factors for the observed neutron distributions were calculated with Monte Carlo simulation of the proton beam line which included the proton beam-line elements, absorbing material, proton beam spread, and the measured resolutions of the FNC and FNT for neutron as described earlier. Monte Carlo events were generated to match the observed uncorrected distributions and the corrected distributions were obtained using bin-by-bin unfolding [72], as described in section 7.4. The advantages of this method are:

- The directly measured position of the inactive material is used;
- Compared to method 2, no assumptions about the angular distributions of neutrons at low $x_L$ have to be made.

The disadvantage of this method are:

- The statistics are limited due to the fact that only data with the LPS detector 6 out of the beam were used. The complicated distribution of the inactive material when LPS detector 6 is in position could not be accurately modeled;
- The Monte Carlo simulation used itself has a bias. The Monte Carlo data are generated under the assumption of a certain neutron distribution in the beginning. Iteration minimizes the bias, but it will not vanish.

In method 2, developed by Garry Levman [73] the inactive material is measured using low $x_L$ neutrons. Because the maximum $p_T$ accepted by the FNC decreases rapidly with $x_L$, and the slope in $p_T$ decreases with $x_L$, low $x_L$ neutrons are approximately uniformly distributed over the acceptance aperture of the FND. Once the inactive material has been mapped using low $x_L$ neutrons, high $x_L$ neutrons which have the most peaked angular distributions can be used to determine a preliminary beam spot.

The systematic error on the preliminary beam spot determined in this manner is $\approx$ 0.1-0.5 cm. The beam spot position is refined and the error reduced using a grid search for the beam spot position which minimizes the difference, after unfolding, between the $p_x^2$ and $p_y^2$ distributions. The procedure is as follows:

1. Measure the position distribution of low $x_L$ neutrons $150 < E_n < 250$ GeV and compare to the expected distribution for neutrons produced uniformly in angle
2. Create an Inactive Material Map (IMM) and smooth statistical fluctuations out of the map
3. Measure the position distribution of high $x_L$ neutrons $(800 < E_n < 920)$ GeV and correct for inactive material using the IMM and smooth statistical fluctuations out of the high $x_L$ angular distribution
4. Use the peak position as a preliminary measurement of the beam spot
5. Using the IMM and the beam spot position unfold the $p_x^2$ and the $p_y^2$ distributions, then move the beam spot position to minimize the difference between the $p_x^2$ and $p_y^2$ distributions.

The final angular distributions are determined by the following procedure:

1. Use the IMM and the beam spot position to determine an acceptance table as a function of $(E_n, \theta)$ assuming perfect resolution
2. Unfold the angular distributions
3. Improve the Acceptance Table using the measured energy and angular distribution to account for finite resolution effects (migrations)

It was found that iteration of steps 2 and 3 was not necessary.

The advantages of this method are:

- There is no need for a simulation of the beam line and inactive material;
- The position of the FNT with respect to inactive material is not needed in the ZEUS coordinate system;

- there is no need to track the movements of the LPS detector 6 into and out of the beam and therefore there is no loss of statistics due to cutting data with the LPS detector 6 in position;
- No Monte Carlo simulation of the "true" physics distributions is required;
- Bin-by-bin unfolding with its concomitant biases is avoided;
- The resultant acceptances are directly applicable to all distributions;
- Each measured event has its own weight so that averages and moments of distributions can be directly determined;
- The method is traditional and natural for a spectrometer of low effective dimension.

The disadvantages of this method are:

- The assumption of uniformity of the angular distribution of neutrons at small $x$ introduces an uncertainty;
- There could be additional error from uncertainties in the IMM.

Comparing the results of the two analysis methods gives a measure of any further systematic error in the results in this thesis, since the two methods have quite different systematic considerations. As an example, Fig. 8.2 shows the comparison of the $(1 - x_L)$ distributions in bins of $t$ for the analysis in this thesis and the analysis of method 2. The two independent methods agree very well. The comparison shows that the systematic uncertainties are of the order of the statistical error or smaller. All comparisons of results show similar behavior, giving confidence that no further systematic errors need to be assigned.

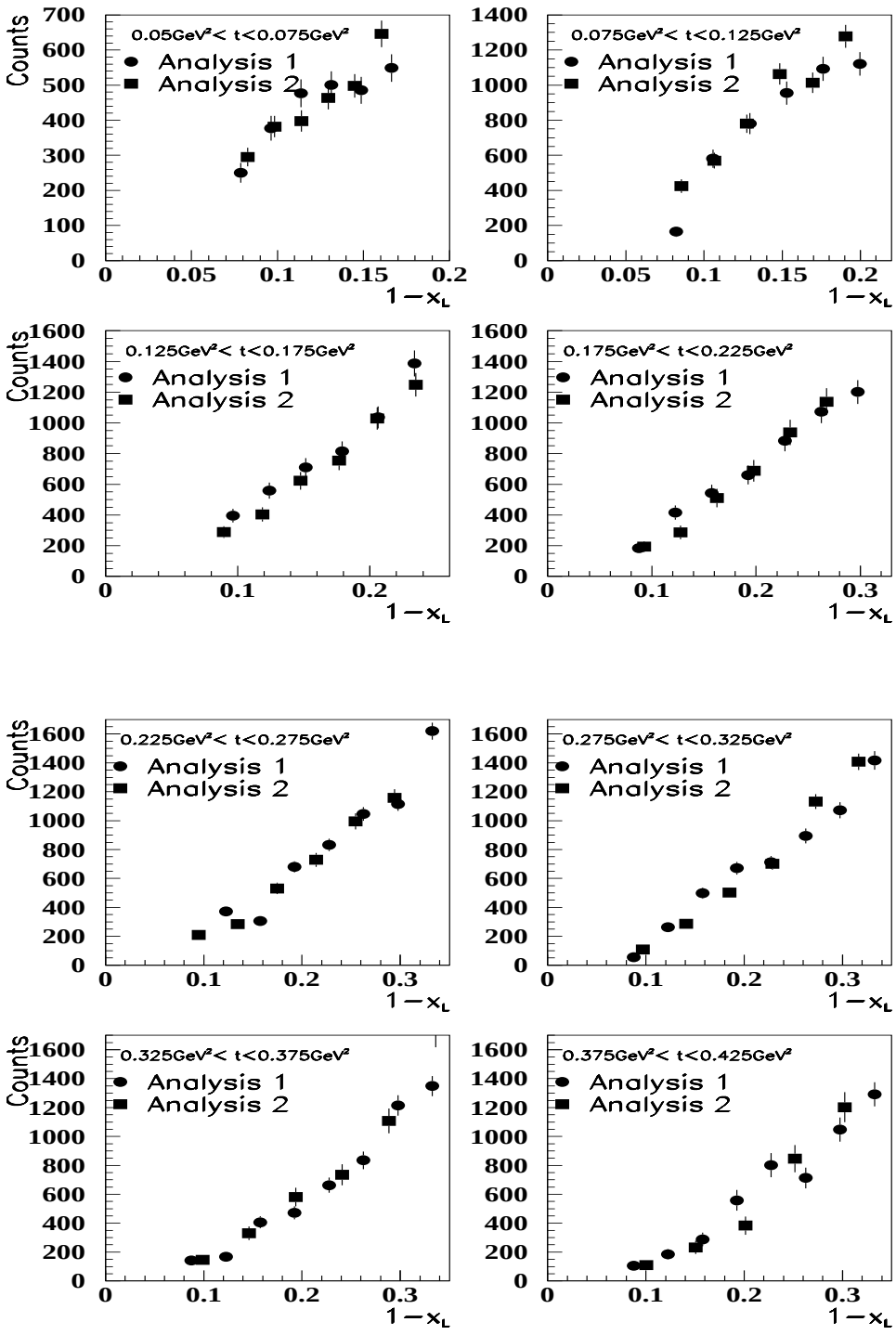


Figure 8.2: The comparison of $(1 - x_L)$ distributions in bins of $t$ for analysis methods 1 and 2.

# Chapter 9

# The $p_T^2$ Distributions of Leading Neutrons

The measurement of the angular distribution of leading neutrons gives the opportunity to better understand the leading neutron production process. The comparison of leading proton angular distributions with those of leading neutrons cast light on differences in the production mechanism. By investigating different channels (DIS, PHP, PHP-dijet) a possible difference in production behavior can be seen. The comparison of predictions of various theoretical flux factors with the measurements can constrain the choice of parameters used in OPE model calculations.

## 9.1 $p_T^2$ Distribution Reconstruction

The transverse momentum squared $p_T^2$ distributions were extracted in bins of $x_L$ using bin-by-bin unfolding. Fig. 3.14 shows the neutron energy distribution for DIS. (A study of the energy distribution as a function of $Q^2$ is made in Chapter 11).

The $p_T^2$ of leading neutrons can be reconstructed using

$$\begin{aligned} p_T^2 &= (E_n \sin\theta_n)^2 \\ &= (E_n \theta_n)^2 \qquad (9.1) \\ &= (E_p \, x_L \, \theta_n)^2, \qquad (9.2) \end{aligned}$$

where $E_p$ is the proton beam energy, $E_n$ is the neutron energy and $x_L = E_n/E_p$. The neutron scattering angle $\theta_n$ is calculated using the measured FNT shower position.

## 9.2 Corrected $p_T^2$ Distributions

Fig. 9.1 shows a comparison of raw $p_T^2$ DIS distributions before unfolding with $p_T^2$ distributions from a MC simulation. The MC and the data agree reasonably well, so bin-by-bin unfolding of the data is justified.

The corrected distributions are fitted to the functional form

$$\frac{dN}{dp_T^2} = N_0 \exp(-bp_T^2) \tag{9.3}$$

and exponential slopes b are obtained.

Figs. 9.2 – 9.4 show DIS, Figs. 9.5 – 9.7 show PHP and Figs. 9.8 – 9.10 show PHP-dijet $p_T^2$ distributions in 12 increasing $x_L$ bins. The results of the exponential fits are also shown in these figures.

## 9.3 Comparison of Neutron and Proton $p_T^2$ slopes in DIS and PHP

Fig. 9.11 shows the comparison of DIS slopes measured for leading neutrons ($ep \to enX$) with the FNT and leading protons ($ep \to epX$) measured with the LPS [74]. While leading neutrons show a rise in the b-slope value with $x_L$, leading protons show just a weak $x_L$ dependence for $x_L > 0.6$. The production process of leading neutrons is dominated by isovector OPE exchange, while leading proton production does not have a dominant single particle exchange production mechanism. Leading protons can be produced by isovector or isoscalar exchange, predominantly $\pi^0$, $\rho$ and Pomeron. $\Delta$ production also contributes [74].

Fig. 9.12 shows the comparison of PHP leading neutron b values to b values of

leading proton production measured previously at ZEUS [74]. As in DIS the b values for leading neutrons rise with $x_L$, while those for leading protons in PHP show a very weak dependence on $x_L$ for $x_L > 0.6$, again indicating more than one dominating production process.

## 9.4 Comparison of b Values for Different Channels

The comparison of the b values in DIS, PHP and PHP-dijet is shown in Fig. 9.13. The values of b rise from $\approx 5\,\mathrm{GeV}^{-2}$ at low $x_L$ to $\approx 11\,\mathrm{GeV}^{-2}$ at high $x_L$. The results for all three data sets are similar. The PHP slopes are systematically higher than the DIS slopes by $\approx 1\,\mathrm{GeV}^{-2}$.

## 9.5 Comparison to OPE Form Factors

The slope of the $p_T^2$ distributions at fixed $x_L$ derives solely from the flux factor $(t/(t-m_\pi^2)^2 F(t))$ if the assumption is made that there is no $t$ dependence in the interaction of the $\gamma^*$ with the virtual exchanged $\pi$, as discussed in Chapter 4. The measured $b(x_L)$ dependence can be compared with the predictions of various OPE models. Figs. 9.14 – 9.16 show the comparison for DIS, PHP and PHP-dijet. The curves labeled Bishari-0, Bishari-4, and KPP are the same model with different choices of parameters. In DIS, some models are inconsistent with the data, while the parameters of others are constrained by the data. OPE is expected to dominate neutron production only for $x_L > 0.6$. In this region several of the models can be rejected immediately as the sole mechanism for producing leading neutrons. Bishari-4 is clearly inconsistent with the data, while Bishari-0 and KPP has a shape compatible with the measured $b-$slopes. The shape of the models MST, PSI, SNS describe the data roughly as well. NSSS, GKS and all the FMS models under consideration can be ruled out. For PHP and PHP-dijet, the picture is similar.

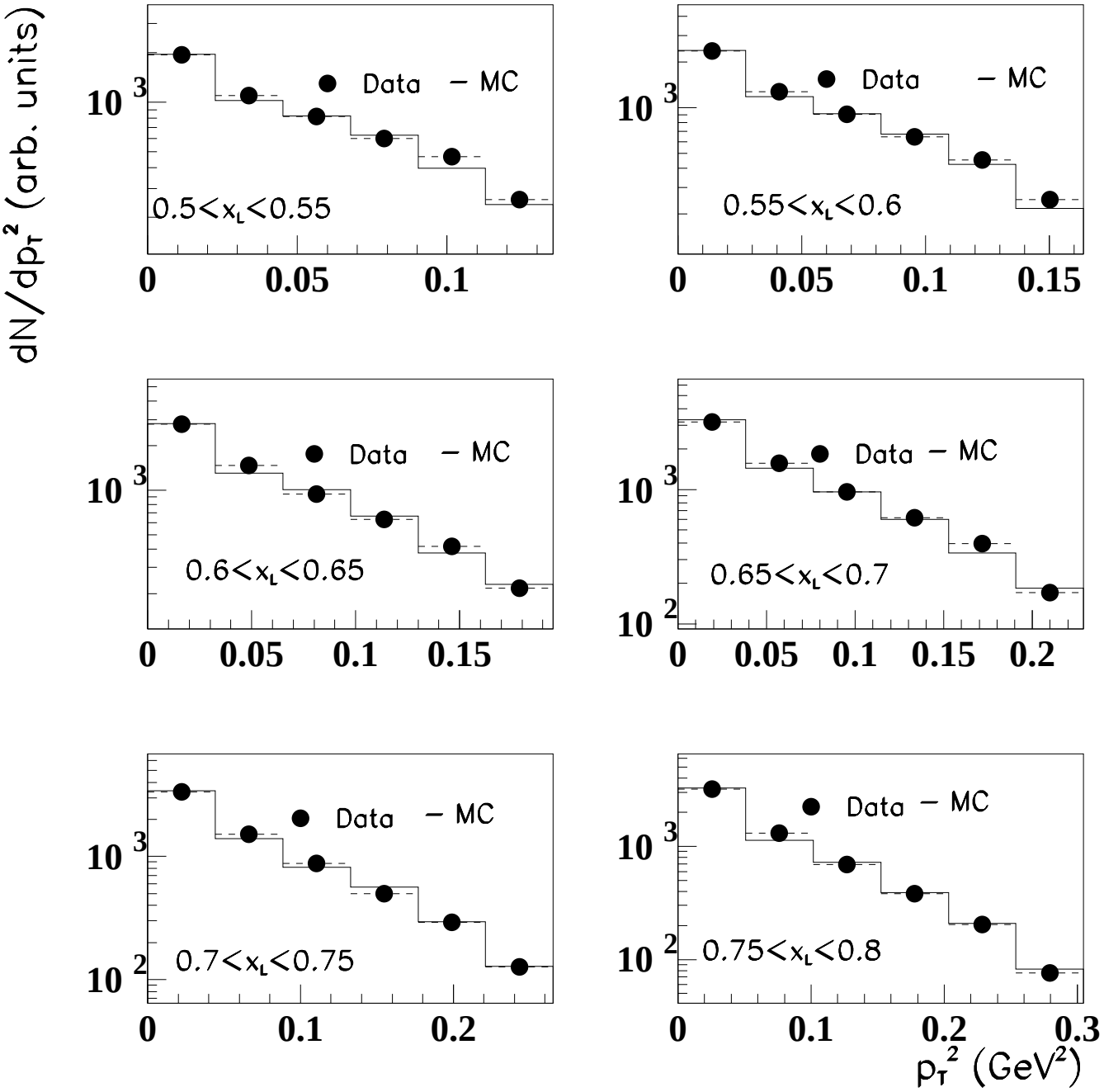


Figure 9.1: Comparison of DIS $p_T^2$ distributions for MC and raw data before unfolding in selected $x_L$ bins.

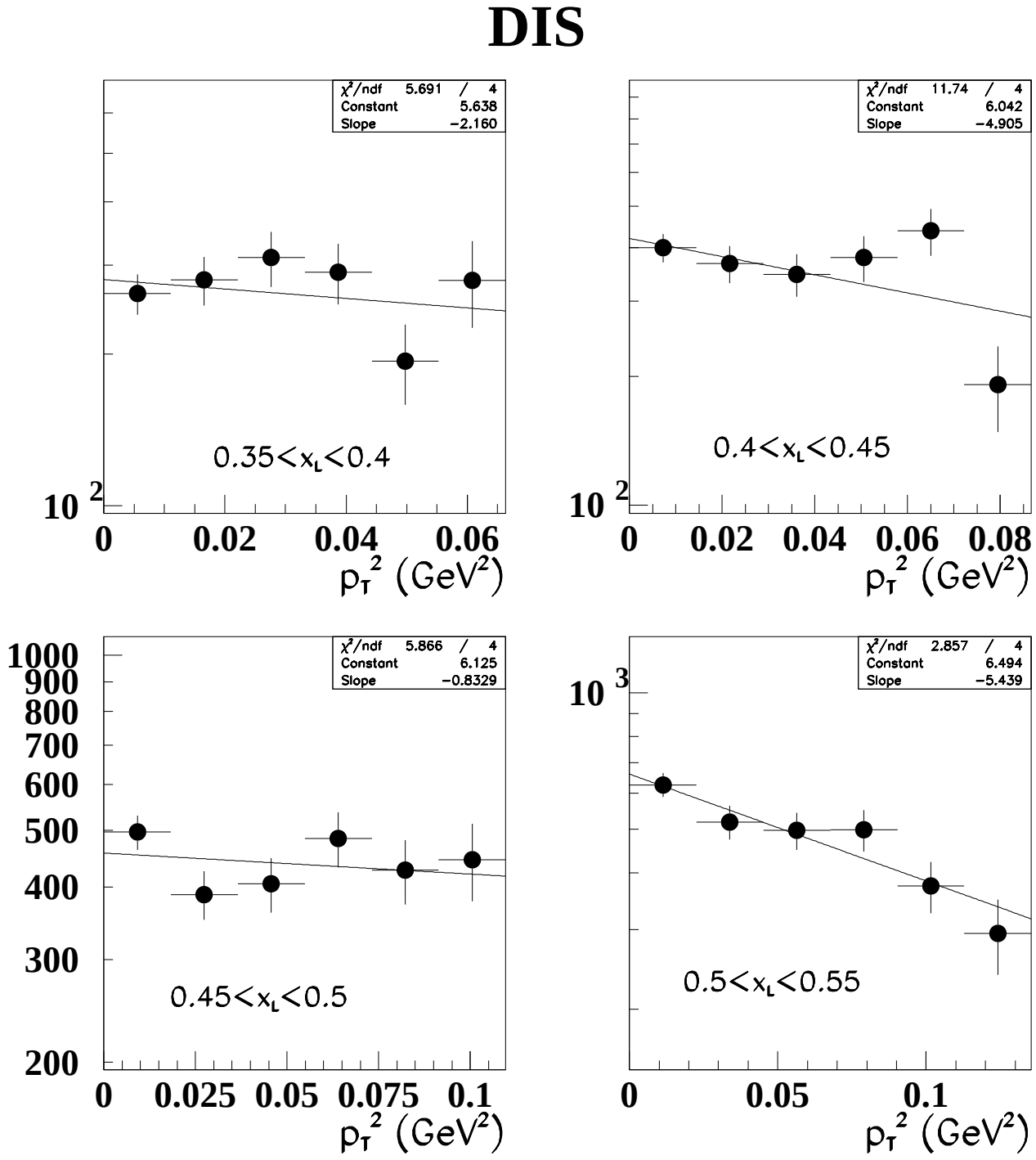


Figure 9.2: Corrected $p_T^2$ distributions for DIS for the $x_L$ bins with $0.35 < x_L < 0.55$.

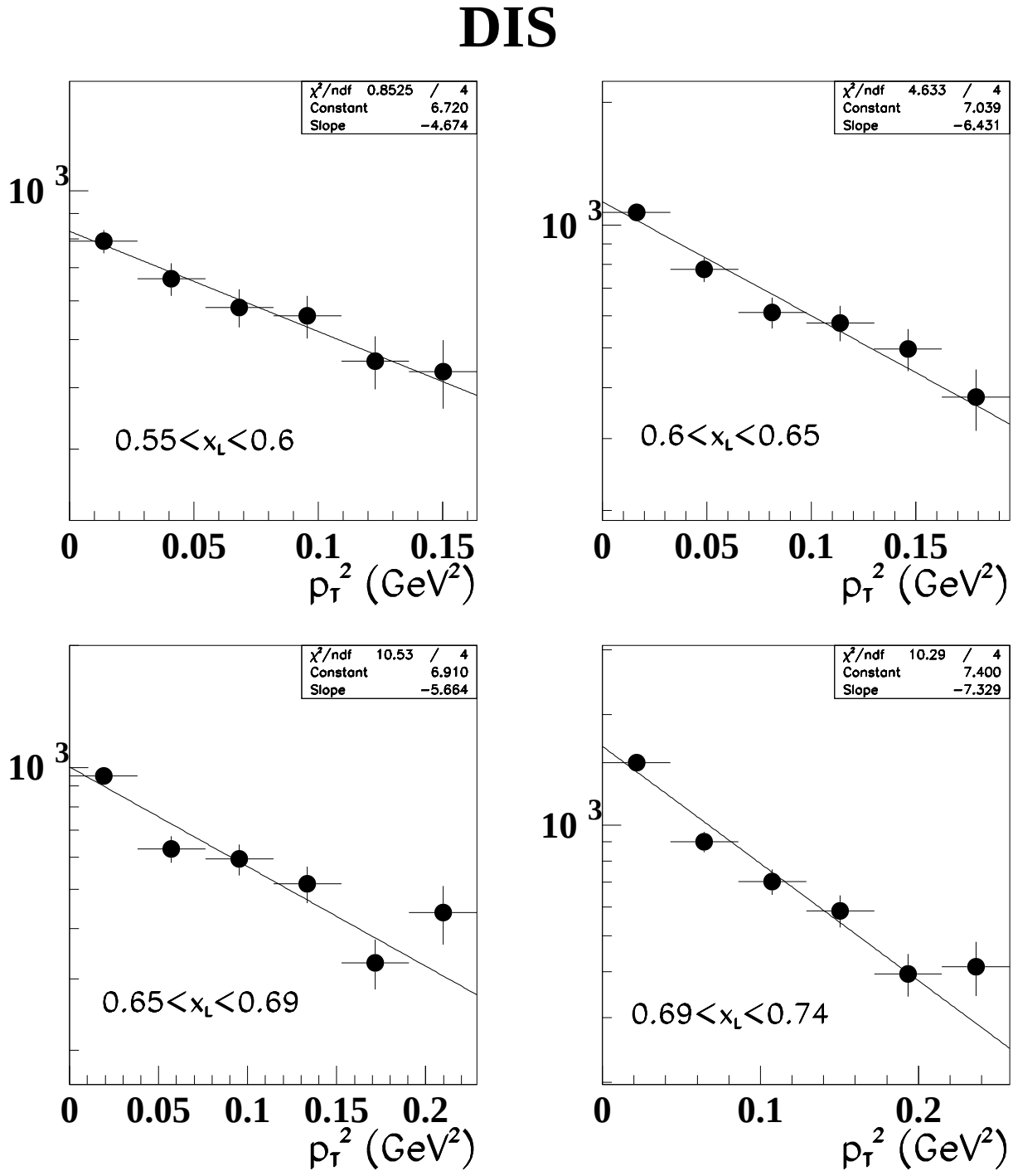


Figure 9.3: Corrected $p_T^2$ distributions for DIS for the $x_L$ bins with $0.55 < x_L < 0.74$.

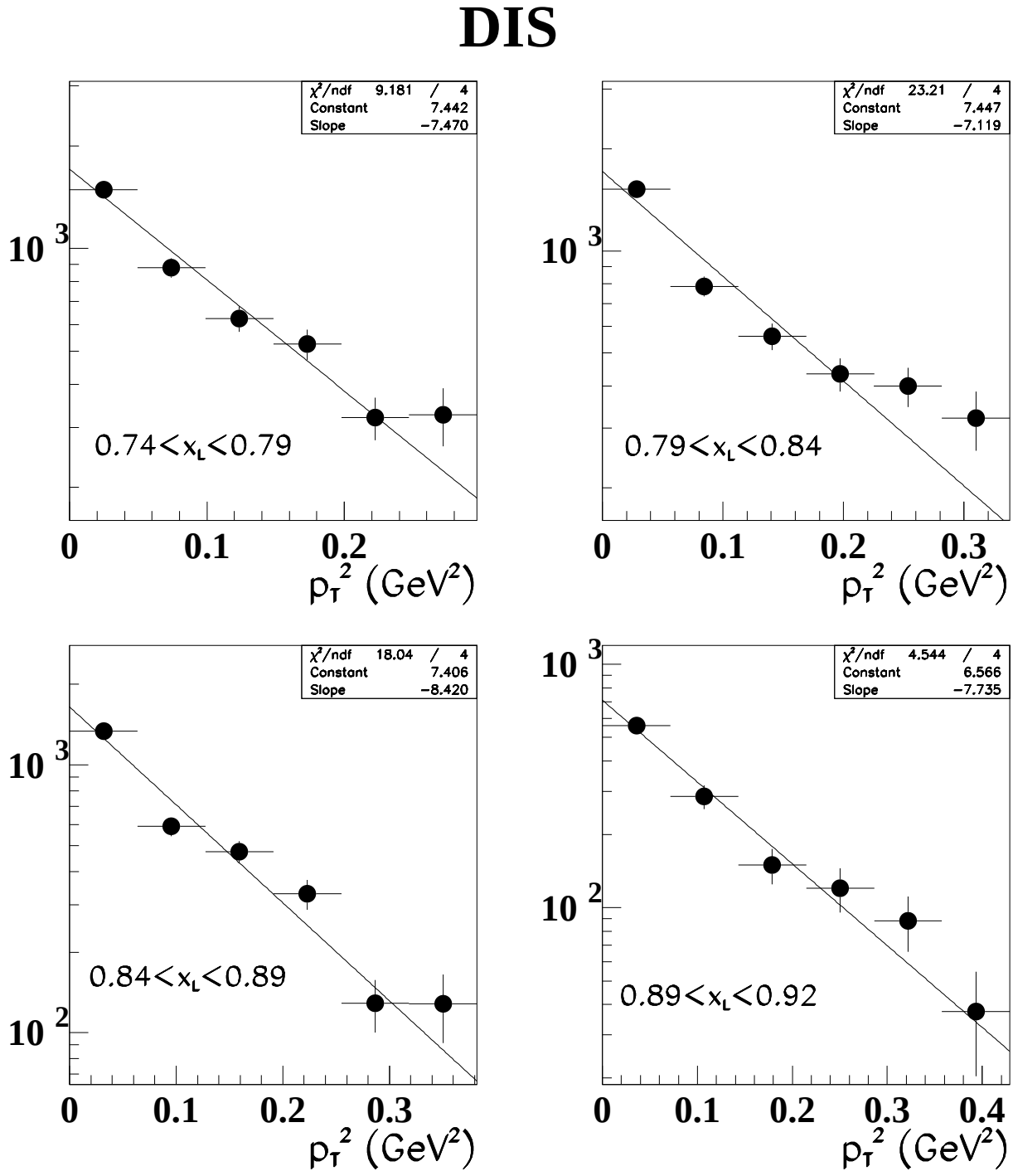


Figure 9.4: Corrected $p_T^2$ distributions for DIS for the $x_L$ bins with $0.74 < x_L < 0.92$.

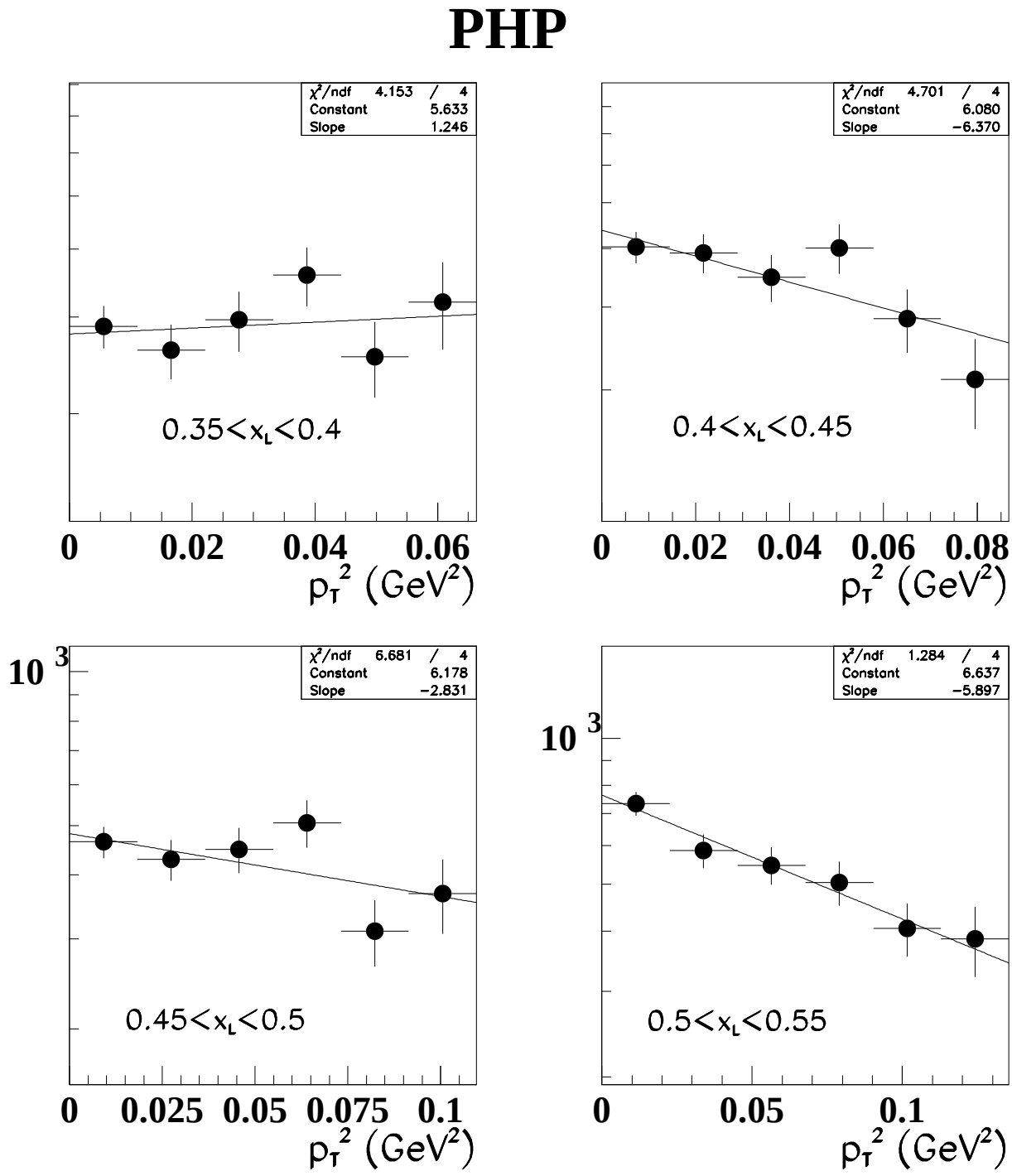


Figure 9.5: Corrected $p_T^2$ distributions for PHP for the $x_L$ bins with $0.35 < x_L < 0.55$.

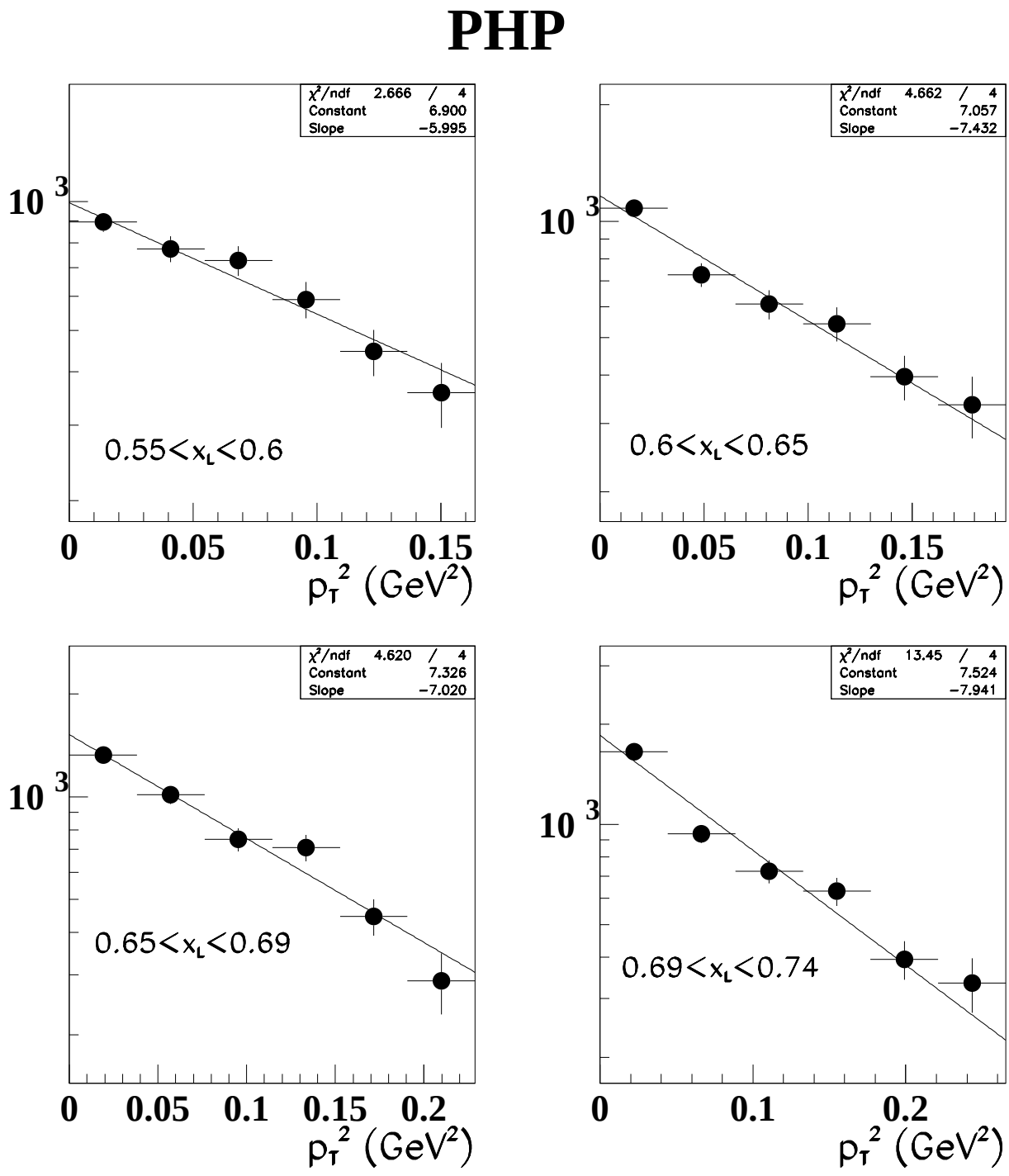


Figure 9.6: Corrected $p_T^2$ distributions for PHP for the $x_L$ bins with $0.55 < x_L < 0.74$.

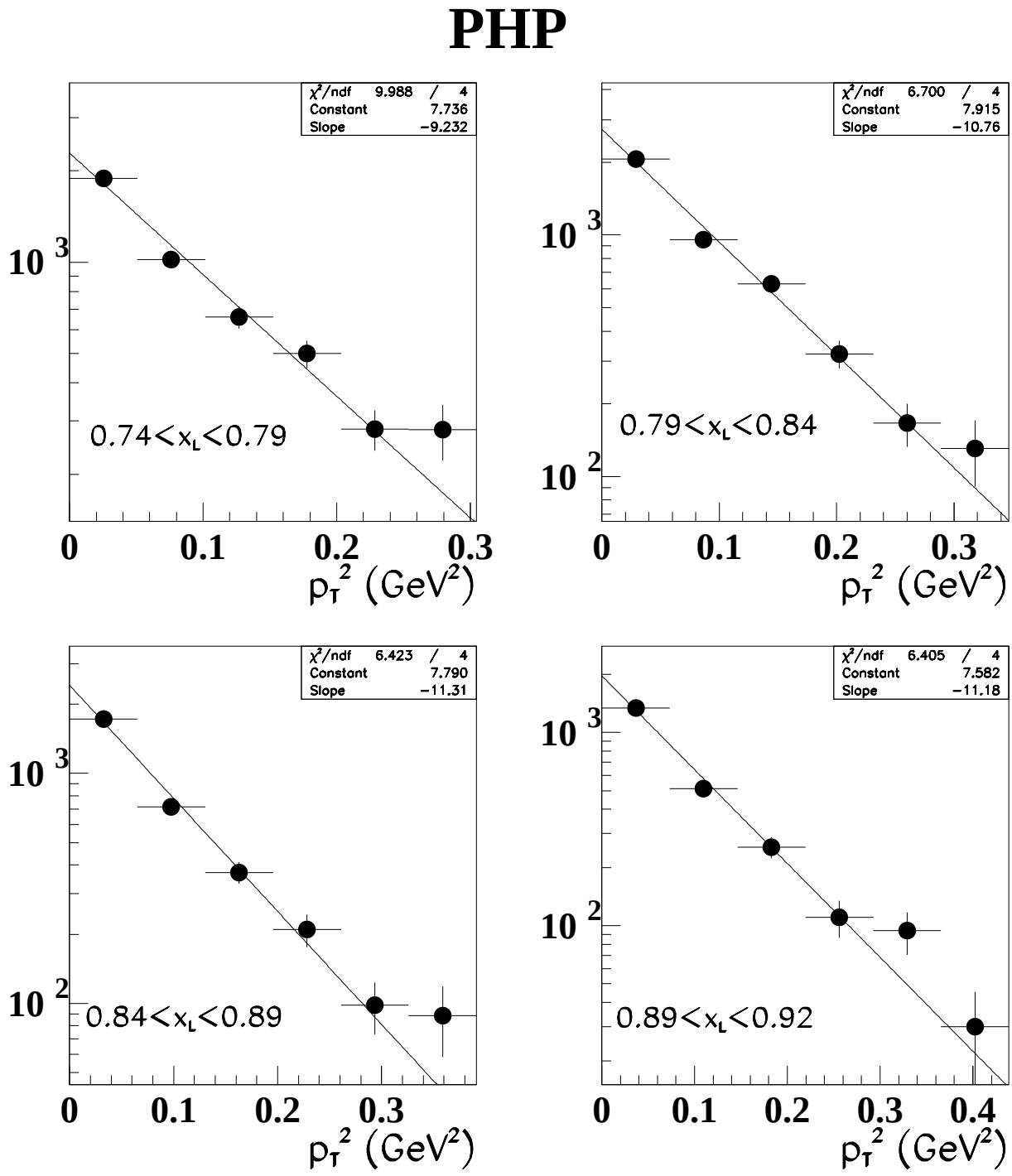


Figure 9.7: Corrected $p_T^2$ distributions for PHP for the $x_L$ bins with $0.74 < x_L < 0.92$.

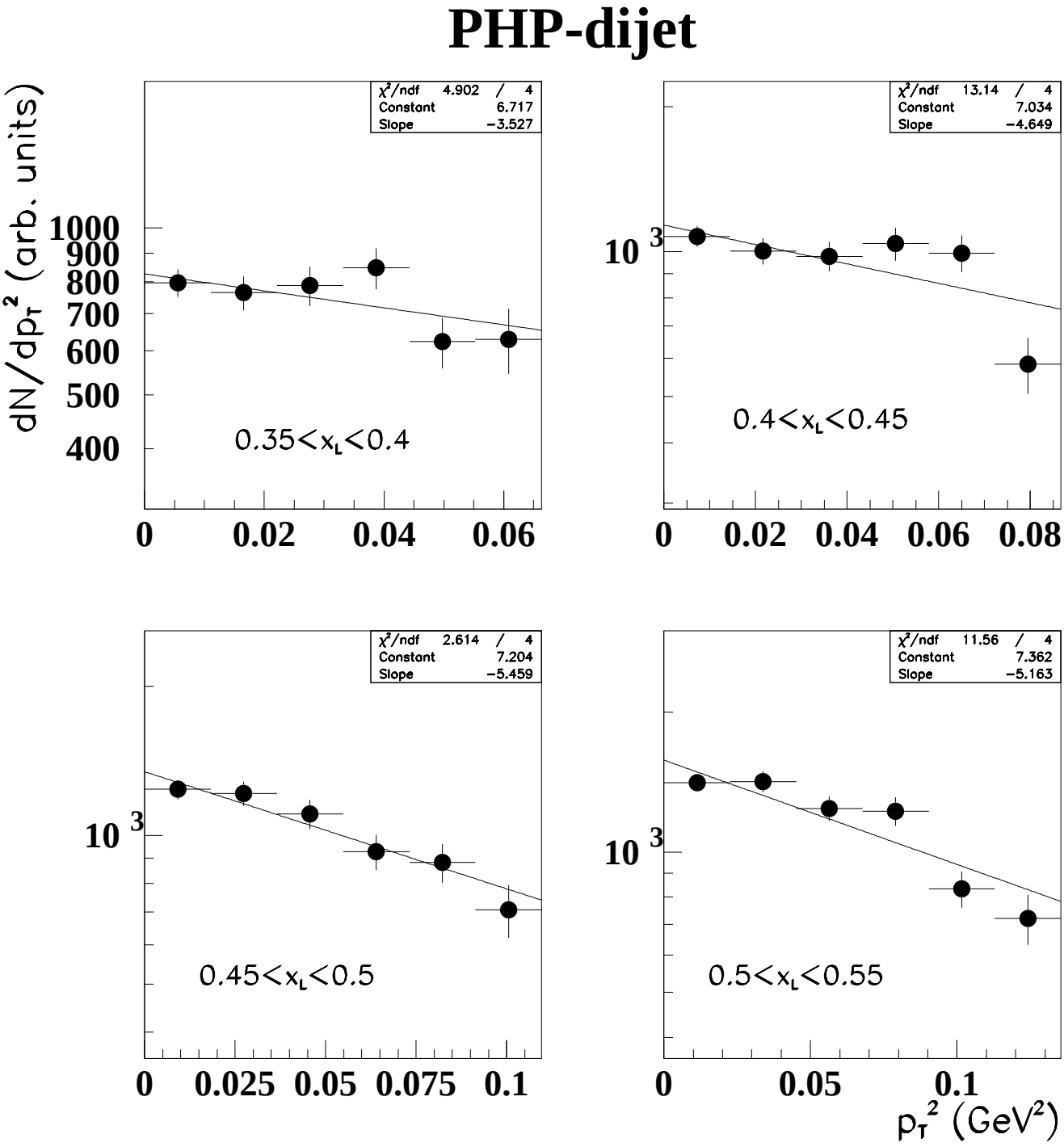


Figure 9.8: Corrected $p_T^2$ distributions for PHP-dijet for the $x_L$ bins with $0.35 < x_L < 0.55$.

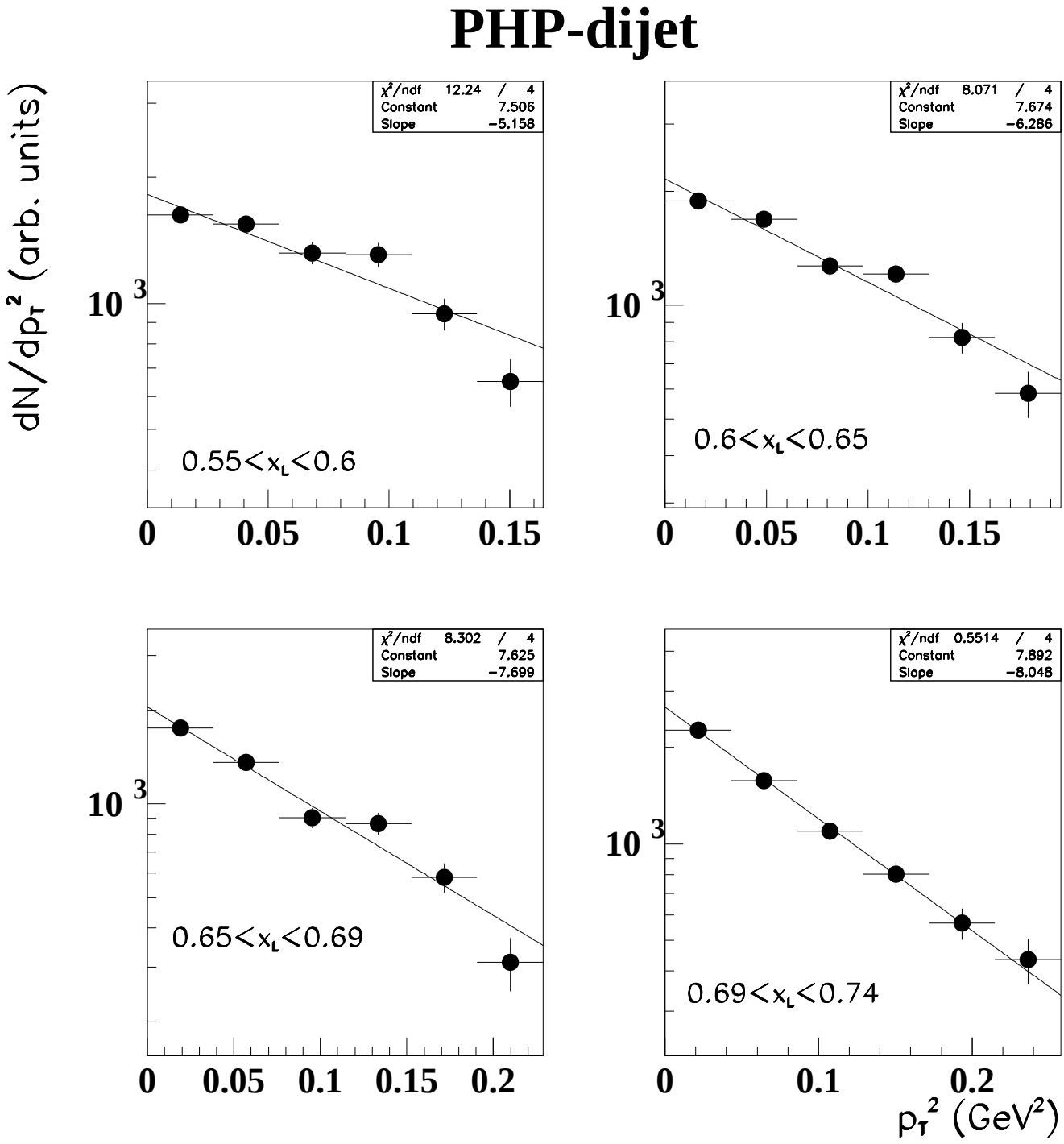


Figure 9.9: Corrected $p_T^2$ distributions for PHP-dijet for the $x_L$ bins with $0.55 < x_L < 0.74$.

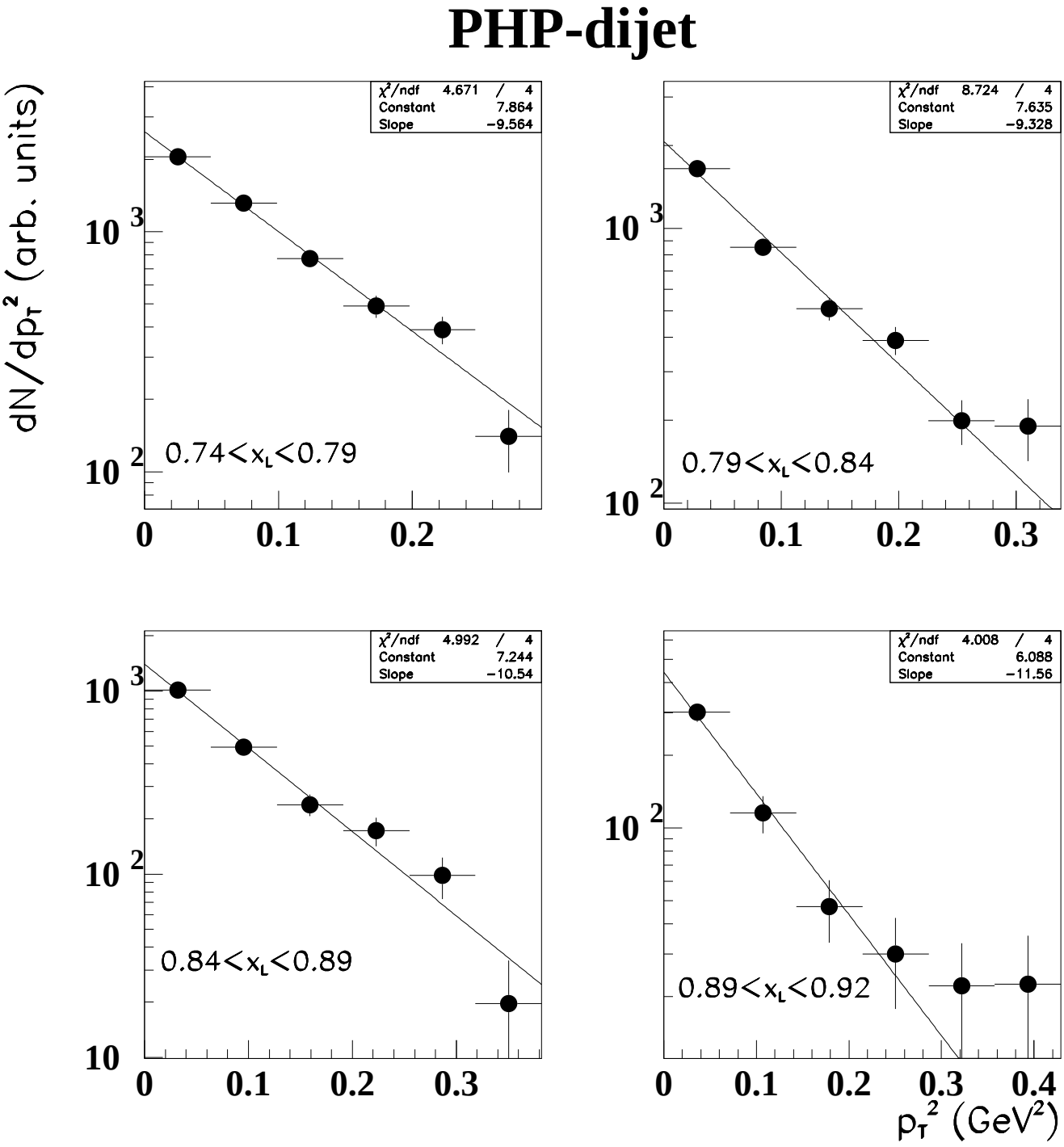


Figure 9.10: Corrected $p_T^2$ distributions for PHP-dijet for the $x_L$ bins with $0.74 < x_L < 0.92$.

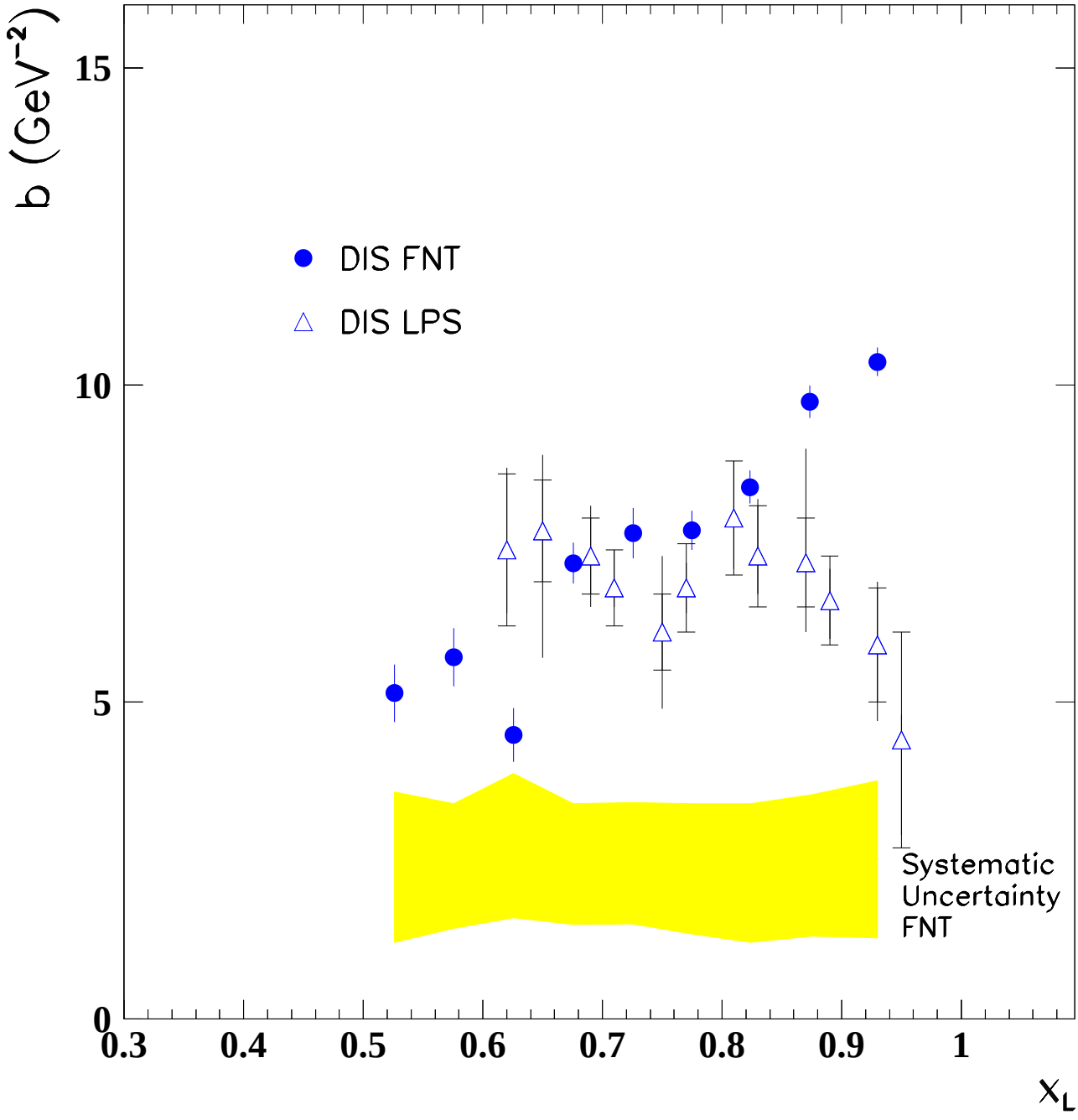


Figure 9.11: Comparison of leading proton b values and leading neutron b values in DIS.

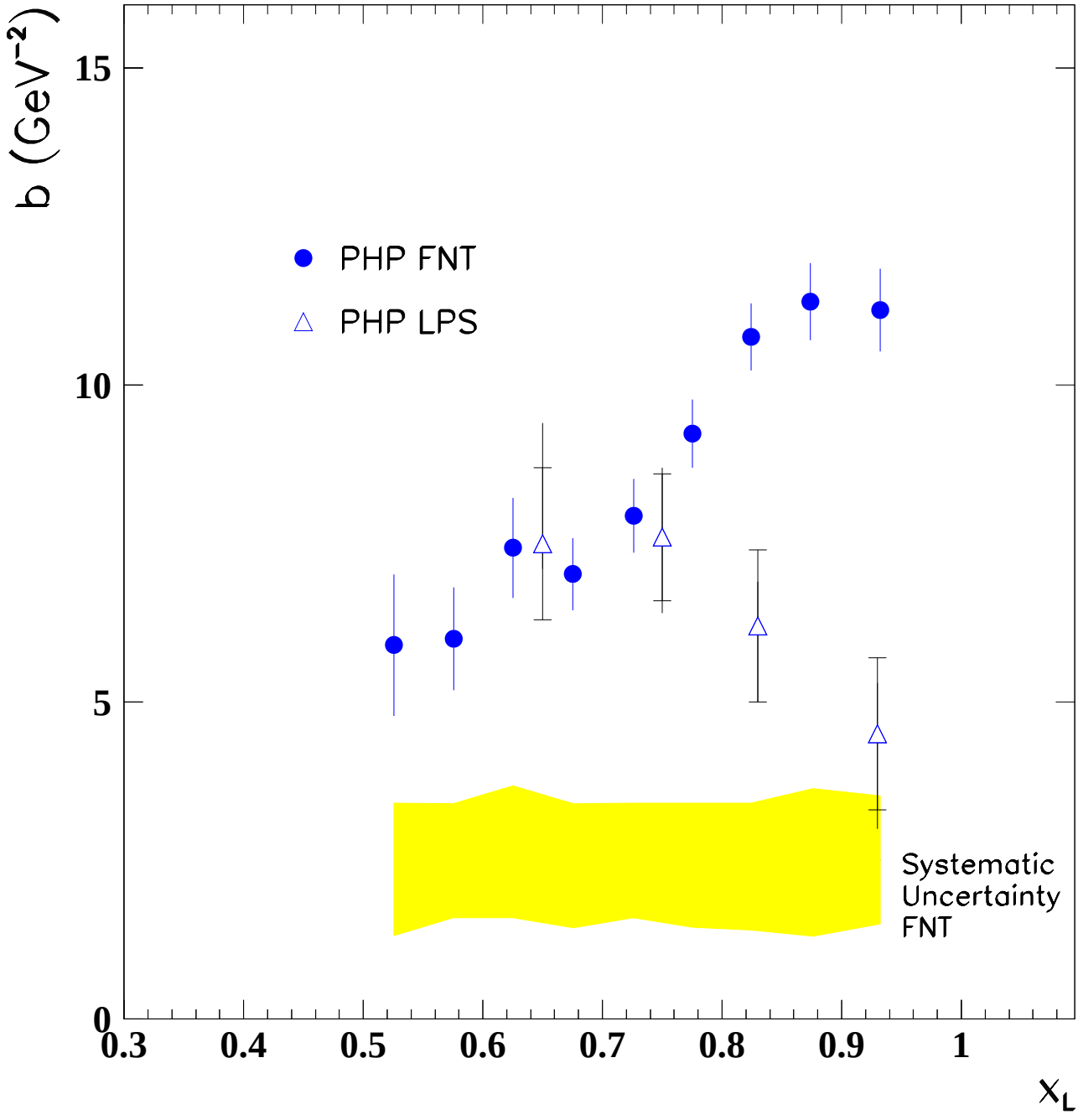


Figure 9.12: Comparison of leading proton b values and leading neutron b values in PHP.

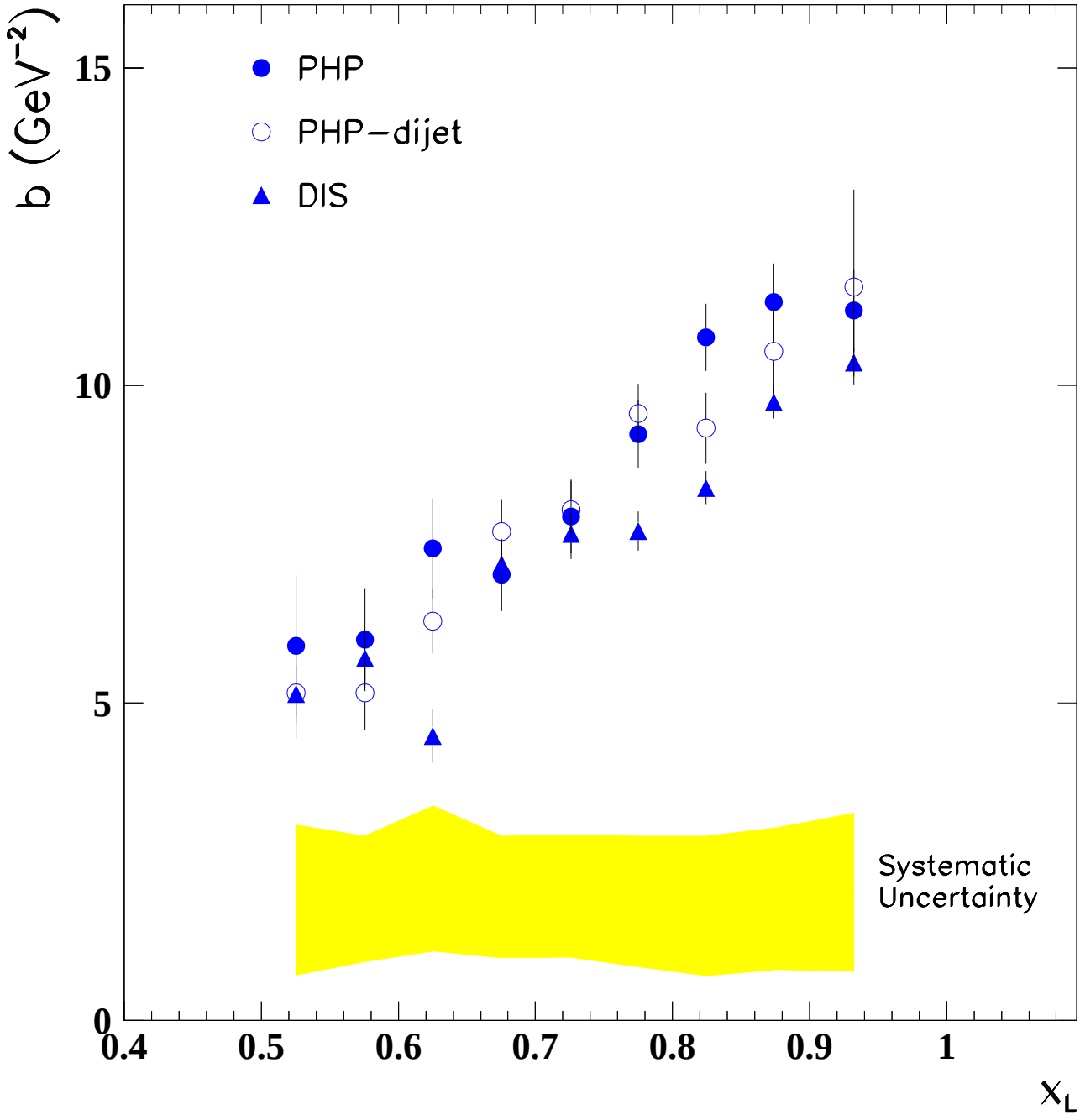


Figure 9.13: The comparison of the b values for DIS and PHP and PHP-dijet.

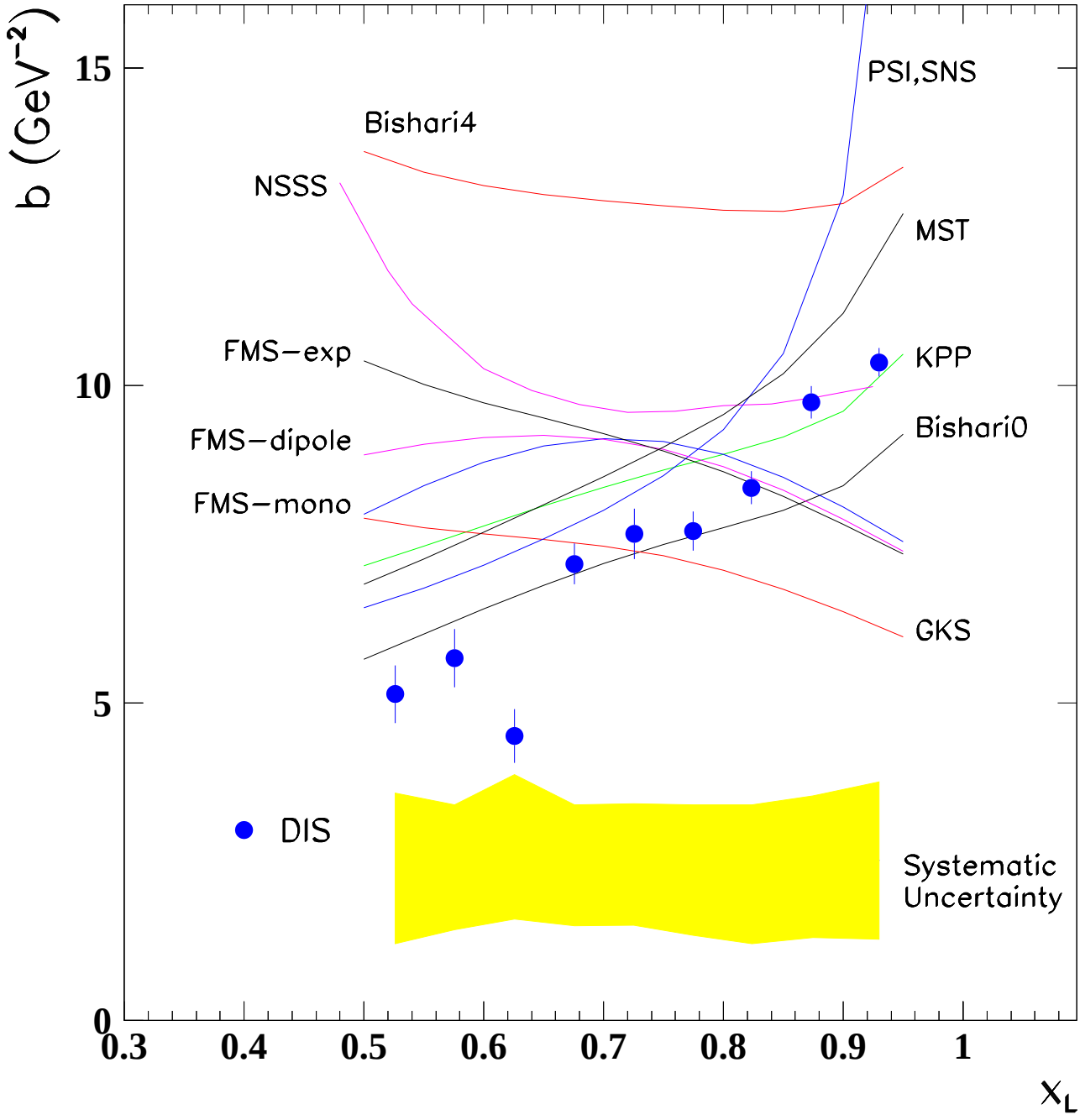


Figure 9.14: The comparison of extracted b values to model predictions for DIS.

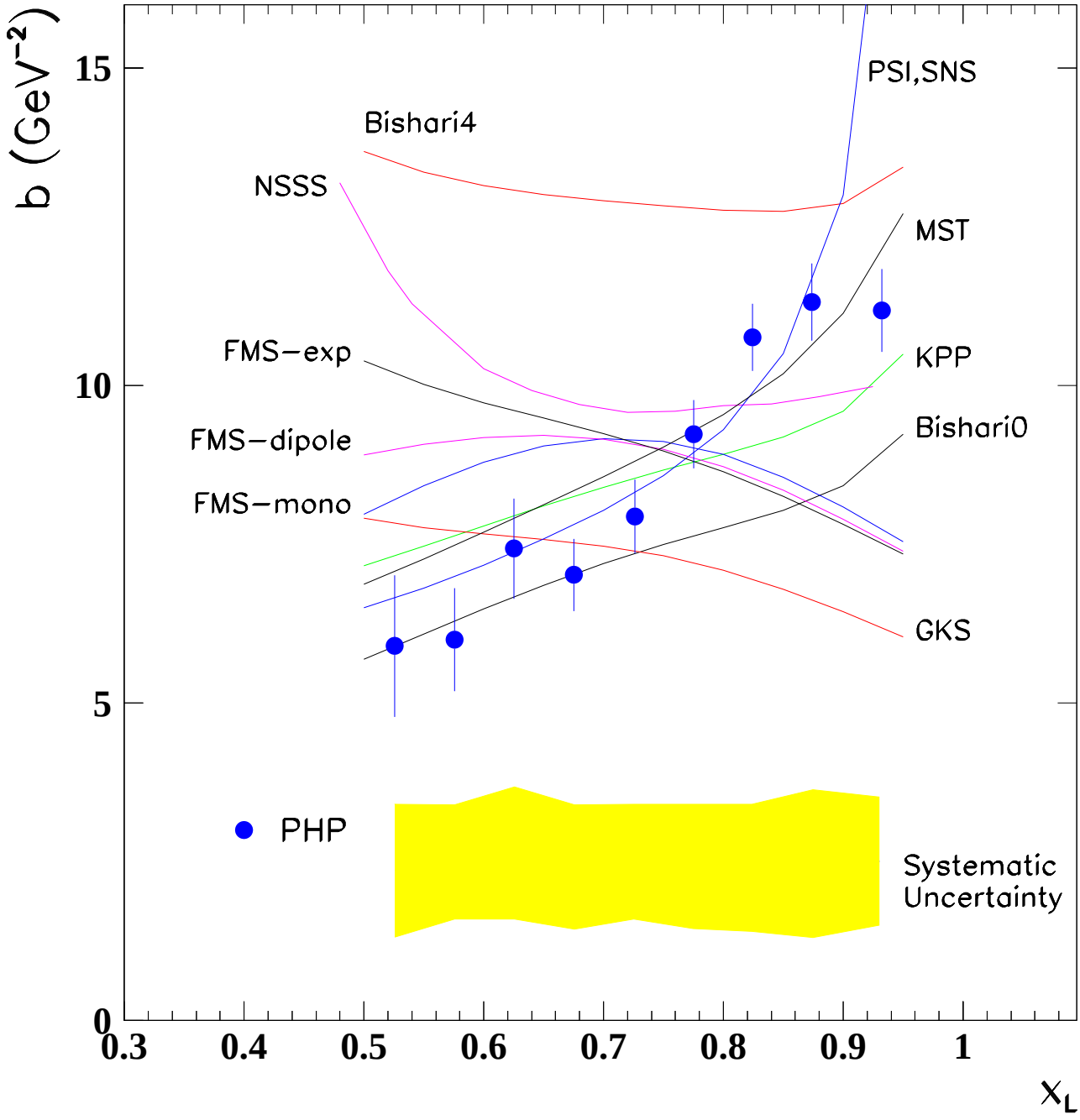


Figure 9.15: The comparison of extracted values of b to model predictions for PHP.

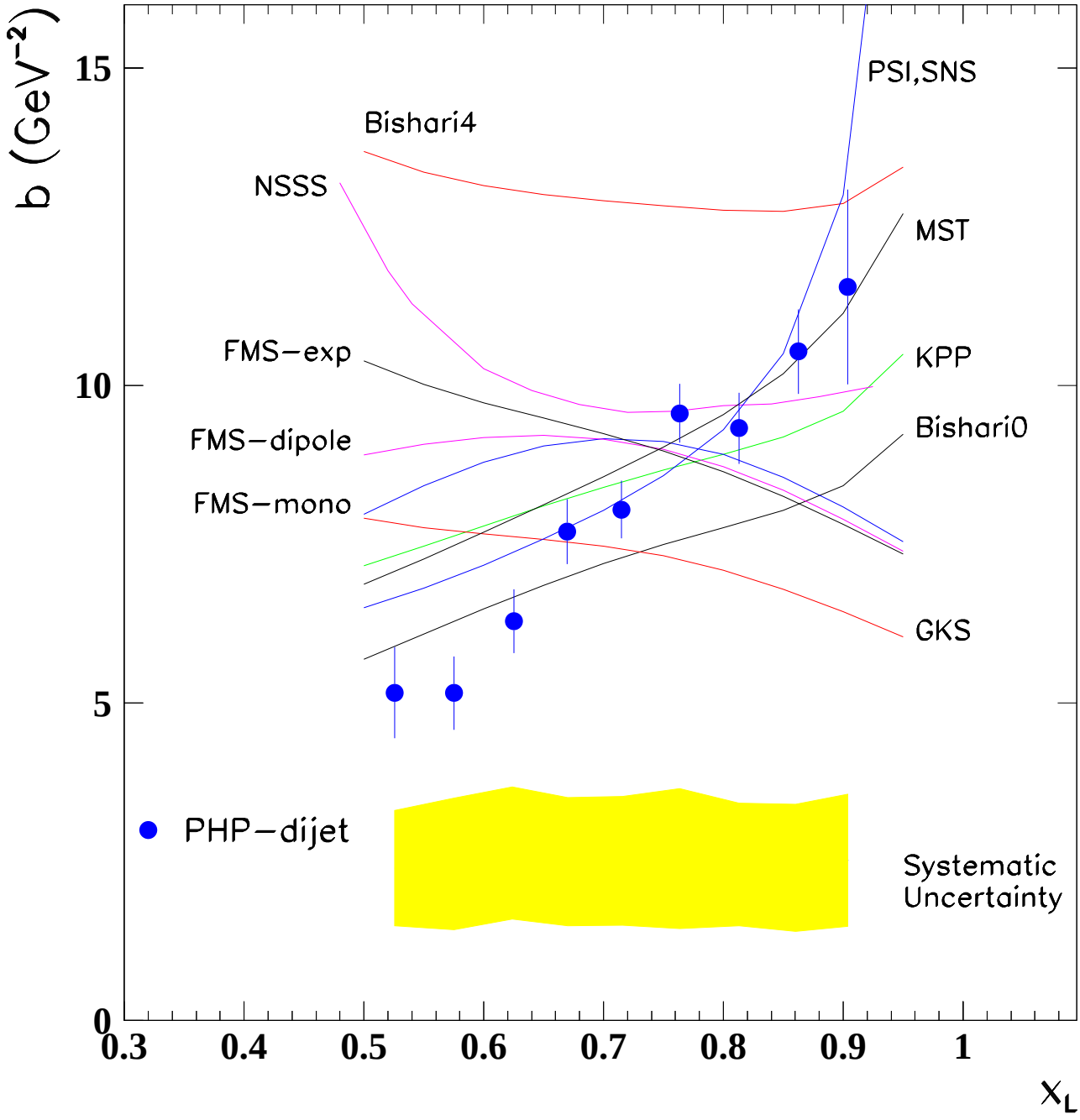


Figure 9.16: The comparison of extracted b values to model predictions for PHP-dijet.

# Chapter 10

# The Pion Trajectory in Photoproduction

For the semi inclusive production process $ep \to enX$, $x_L$ and the invariant momentum transfer squared $t$ between the incoming proton and the neutron are related by the following equation:

$$t = -\frac{p_T^2}{x_L} - \frac{(1-x_L)}{x_L}(m_n^2 - x_L m_p^2), \tag{10.1}$$

with $m_p$ the mass of the proton, $m_n$ the mass of the neutron, and $p_T = E_n\theta_n$ the transverse momentum of the neutron.
The pion flux can be written as

$$f_{\pi/p}(x_L, t) = \frac{1}{4\pi}\frac{g_{n\pi p}^2}{4\pi}\frac{-t}{(m_\pi^2 - t)^2}(1-x_L)^{1-2\alpha_\pi(t)}(F(t))^2, \tag{10.2}$$

where $\alpha_\pi(t) = \alpha_\pi^{'} t$ is the Regge trajectory of the pion with slope $\alpha_\pi^{'}$. The form factor, $F(t)$, is independent of $x_L$ in a covariant approach.

In this case, the flux factor can be parameterized as

$$f_{\pi/p} = A(t)(1-x_L)^{a(t)}, \tag{10.3}$$

which leads to a neutron production cross section of

$$\frac{d^2\sigma}{dx_L dt} = A(t)(1-x_L)^{a(t)}\sigma_{\gamma^*\pi}((1-x_L)W^2, t, Q^2), \tag{10.4}$$

where $\sigma_{\gamma^*\pi}$ is the total cross section. In the following analysis any $t$ dependence of $\sigma_{\gamma^*\pi}$ is assumed to be small and is neglected. The $\gamma^*\pi$ center-of-momentum energy squared $s_{\gamma^*\pi}$ is given by

$$s_{\gamma^*\pi} = (1-x_L)W^2. \tag{10.5}$$

For photoproduction ($Q^2 = 0$) $\sigma_{\gamma^*\pi} \approx \sigma_{\gamma\pi}$, which has a well known power law dependence [54]:

$$\sigma_{\gamma\pi}(s_{\gamma\pi}) = A_{I\!P}(s_{\gamma\pi})^{\epsilon} + A_{I\!R}(s_{\gamma\pi})^{-\eta} \tag{10.6}$$

with $\epsilon = \alpha_{I\!P}(0) - 1 \approx 0.1$ and $\eta \approx 0.5$. At large $s_{\gamma\pi}$, the Pomeron $I\!P(\epsilon)$ term dominates the Reggeon $I\!R(\eta)$ term and the $(1-x_L)$ distribution is proportional to $(1-x_L)^{a_{eff}(t)}$, where the effective trajectory $a_{eff}(t)$ is given by

$$a_{eff}(t) = 1 + \epsilon - 2\alpha_{\pi}^{'}t. \tag{10.7}$$

Fig. 10.1 shows the kinematic region in $t$ and $p_T^2$ that is covered by the FND as a function of $x_L$. Fig. 10.2 shows the $(1-x_L)$ distributions of the PHP data in different $t$ bins. The PHP events were selected as described in section 6.3 and section 6.5. The determination of the systematic uncertainties are described in Chapter 8. The distributions are approximately power laws in $(1-x_L)$, i.e.:

$$dN/dx_L \propto (1-x_L)^{a(t)}. \tag{10.8}$$

For each $t$ bin the power $a(t)$ was obtained by a linear least squares fit to the observed distribution for $x_L < 0.92$. Only statistical errors were used in the fits because the systematic uncertainties are highly correlated point to point. The resulting fits are superimposed on the figures.

Fig. 10.3 shows $a_{eff}$ for PHP as a function of $-t$ and a fit of $a_{eff}(t)$ to a straight line:

$$a_{eff}(t) = 1.08 \pm 0.08^{+0.40}_{-0.42} - (2.78 \pm 0.32^{+0.31}_{-0.41}\ \mathrm{GeV}^{-2})t. \tag{10.9}$$

This results (using equation 10.7) in the following values for the trajectory:

$$\alpha_{I\!P}(0) = 1.08 \pm 0.08^{+0.40}_{-0.42} \quad \text{and} \quad \alpha_{\pi}^{'} = 1.39 \pm 0.16^{+0.16}_{-0.21}\,\text{GeV}^{-2}. \tag{10.10}$$

The results for the pion slope and the pomeron intercept are in good agreement with the expected values of $\alpha_{I\!P}(0)$ and $\alpha_{\pi}^{'}$, and are evidence for the dominance of OPE in the process $ep \to enX$ at very low $Q^2$.

## 10.1 Comparison to earlier Measurements

The effective pion trajectory has been determined in earlier measurements of hadronic interactions. One example is the inclusive reaction $\pi^- n \to pX^{--}$ [75]. The results were:

$$a^{\pi}_{eff}(t) = (0.14 \pm 0.07) + (1.09 \pm 0.19)t \tag{10.11}$$

at $\sqrt{s} = 21\,\text{GeV}$ and

$$a^{\pi}_{eff}(t) = (0.32 \pm 0.08) + (1.30 \pm 0.20)t \tag{10.12}$$

at $\sqrt{s} = 205\,\text{GeV}$ and $360\,\text{GeV}$.

The inclusive reactions $pn \to pX$ and $\pi^+ n \to pX$ have also been studied [76], with the result

$$a^{\pi}_{eff}(t) = (0.26 \pm 0.04) + (1.07 \pm 0.11)t \tag{10.13}$$

at $\sqrt{s} = 100\,\text{GeV}$.

Finally, in the reactions $pp \to nX$ [77], $\alpha_{\pi}^{'}$ was found to be 1.34, 1.16, 1.29 and 1.13 at $\sqrt{s} = 62.7\,\text{GeV}$, $52.8\,\text{GeV}$, $44.9\,\text{GeV}$ and $\sqrt{s} = 30.6\,\text{GeV}$ respectively. $\alpha_{\pi}(0)$ was averaged over all energies with the result

$$\alpha_{\pi}(0) = -0.11 \pm 0.15. \tag{10.14}$$

The earlier measurements for $\alpha_{\pi}$ are in good agreement with the results of this thesis, given in equation 10.10.

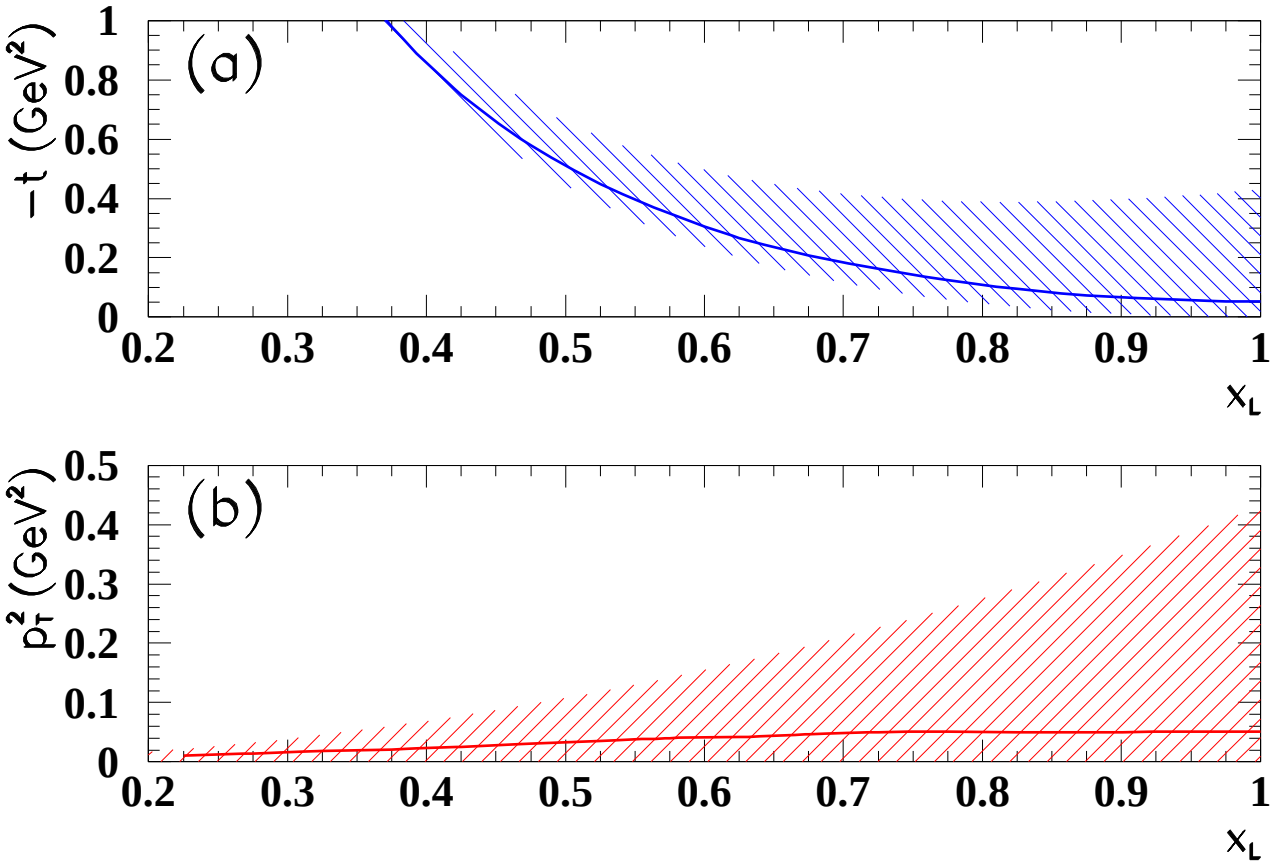


Figure 10.1: The kinematic region in $t$ (a) and in $p_T^2$ (b) that is covered by the angular acceptance of the FND are shown as shaded band, as a function of $x_L$. The solid lines indicate the average $t$ and $p_T^2$ values.

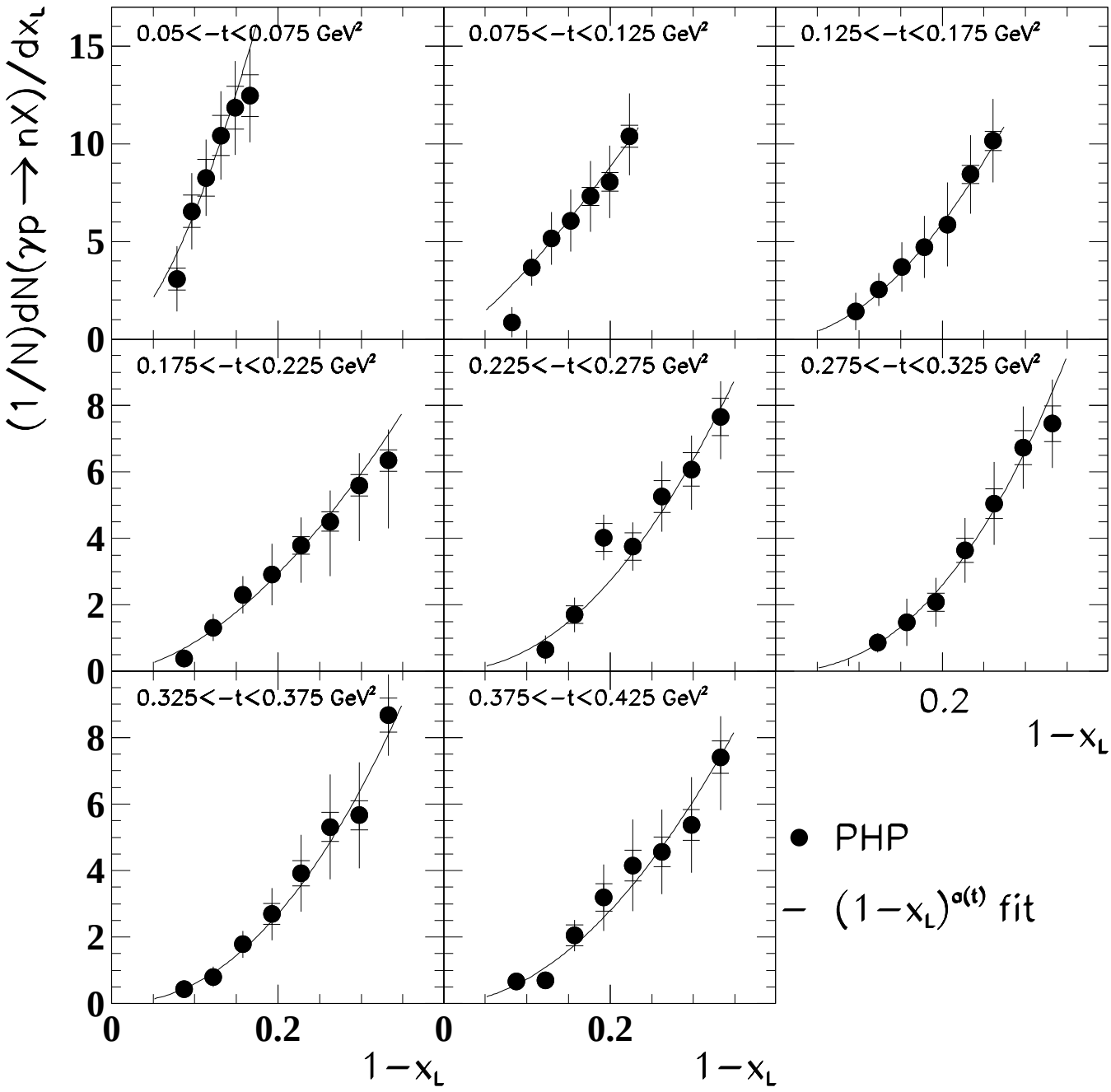


Figure 10.2: The neutron $x_L$ spectrum for inclusive photoproduction in bins of invariant momentum transfer squared $t$. The curve shows the results of fits to the inclusive photoproduction data of the form $A(t)(1 - x_L)^{a(t)}$. The error bars show the contribution of the statistical (inner) and systematic error (outer) to the total uncertainty.

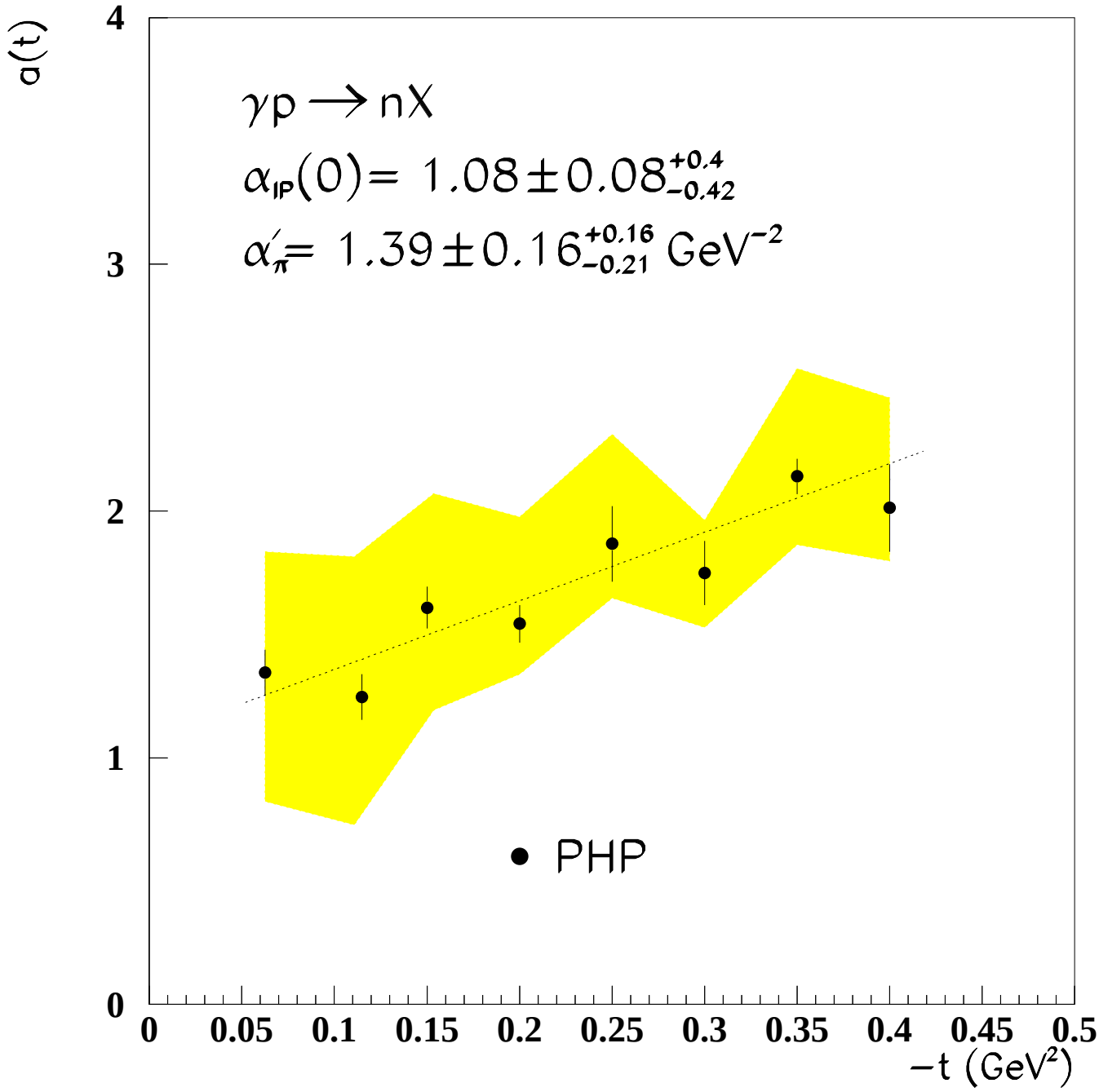


Figure 10.3: The effective powers for PHP (•) as a function of the invariant momentum transfer squared $t$ determined by least squares fits to the $1 - x_L$ distributions. The effective powers for the photoproduction data have been fit to a straight line. The error bars show the contribution of statistical error to the total uncertainty. The band shows the systematic errors.

# Chapter 11

# Comparison of PHP and DIS $x_L$ Spectra

As described in Chapter 4, neutron absorption can occur through rescattering of the neutron on the photon. Since the size of the virtual photon falls like $Q^{-1}$, more neutron rescattering would be expected for photoproduction than for DIS. The variation of the mean size of the $n$-$\pi$ system as a function of $x_L$ in exchange models leads to an $x_L$ dependence of the absorption. Hence vertex factorization should be violated, that is

$$\frac{1}{\sigma_{\rm tot}^{\gamma p\to Xn}}\frac{d^2\sigma^{\gamma p\to Xn}(x_L,p_T^2)}{dx_L dp_T^2} \neq \frac{1}{\sigma_{\rm tot}^{\gamma^* p\to Xn}}\frac{d^2\sigma^{\gamma^* p\to Xn}(x_L,p_T^2)}{dx_L dp_T^2}. \qquad (11.1)$$

The aim of this analysis is to compare the $x_L$ distributions of neutrons for different ranges of photon virtuality $Q^2$. Fig. 11.1 shows the uncorrected neutron energy distributions for the three data sets: DIS, PHP and PHP-dijet. While the three distributions have a similar shape, the change in shape from PHP to DIS is clearly visible, with PHP-dijet lying between the two, but closer to PHP.

A straightforward way to compare the $x_L$ distributions is to take the ratios of the distributions at different $Q^2$. Differences in the shapes are then readily apparent. The data in this thesis are then compared to the two model calculations of absorption in the context of OPE describe in Chapter 4.

An important feature of the analysis in this chapter is that only the DIS data taken

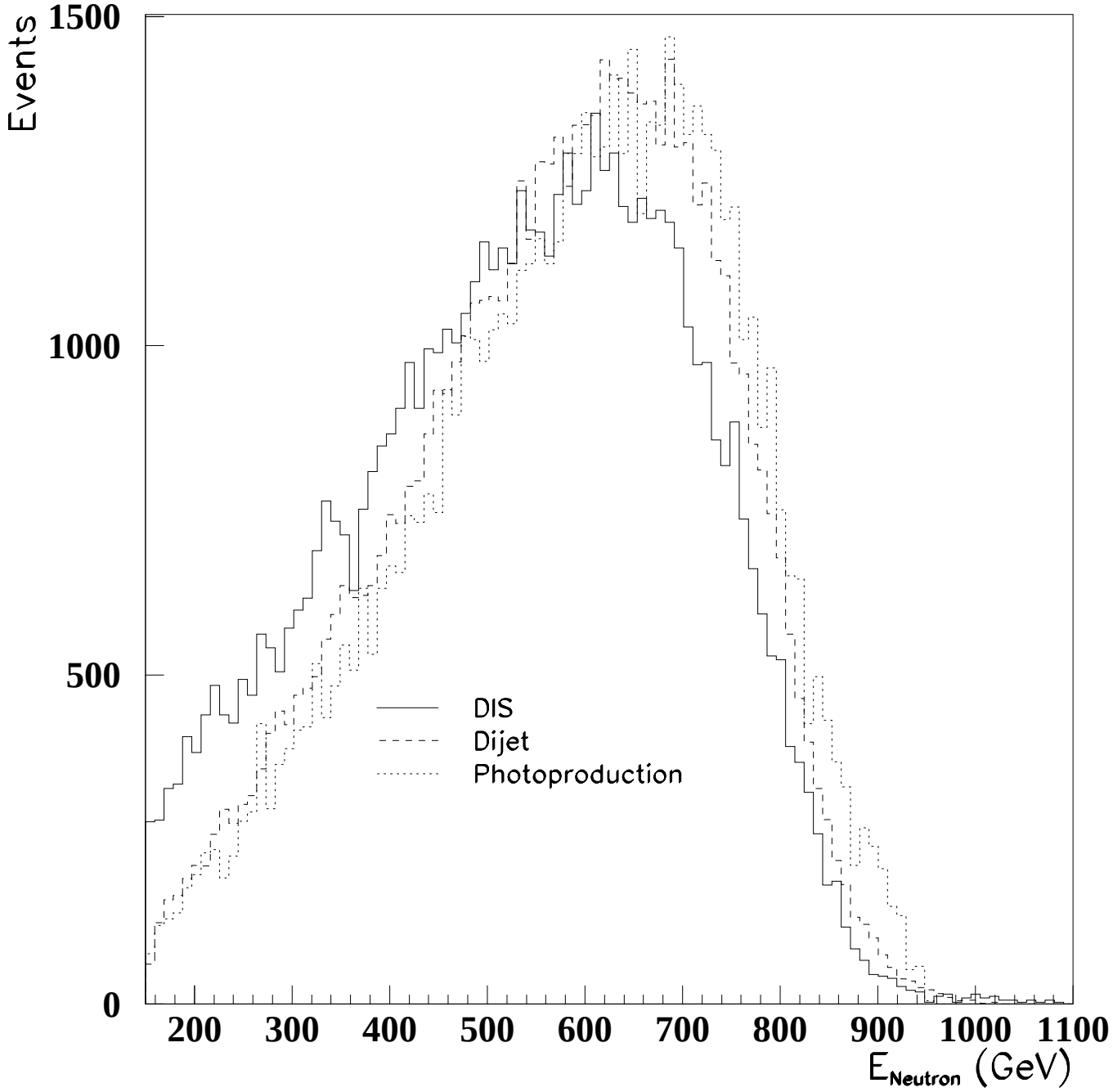


Figure 11.1: Comparison of DIS, PHP and PHP-dijet neutron energy distributions.

simultaneously with the PHP data set (corresponding to 9.3 pb$^{-1}$) is used. Hence a comparison of the two $x_L$ distributions can be made without systematic errors due to the energy scale uncertainty and acceptance uncertainties, since these will largely cancel in the ratio.

In Fig. 11.2 the ratio of the DIS and PHP distributions normalized by their respective inclusive cross sections are given as a function of $x_L$:

$$\rho(x_L) = \frac{\frac{1}{\sigma(\gamma^* p)}\frac{d\sigma(\gamma^* p \to n)}{dx_L}}{\frac{1}{\sigma(\gamma p)}\frac{d\sigma(\gamma p \to n)}{dx_L}}.$$

The current set of data cannot be used to completely fix this normalization because of different efficiencies for the DIS and photoproduction triggers. The inclusive cross section $\sigma(\gamma^* p \to X)$ and $\sigma(\gamma p \to X)$ were not determined. Instead the previous results from ZEUS [10] were used. The ratio $\rho(x_L)$ was rescaled such that it matched these results in the range $0.64 < x_L < 0.82$, resulting in an overall uncertainty in $\rho$ of $\pm$ 0.05. In the range of $0.2 < x_L < 0.55$, the ratio drops slightly. It rises for higher $x_L$ values, exceeding unity for $x_L > 0.9$. Shown as well is the previous ZEUS result, which had worse statistical and systematic uncertainties. Except for the highest $x_L$ point, the old and new data sets are in good agreement. The theoretical predictions discussed in Chapter 4 for absorptive effects are indicated by the lines. These predictions were calculated for the $Q^2$ range 10–100 GeV$^2$. The model of D'Alesio and Pirner [58] is in moderate agreement with the data, but the model of Nikolaev, Speth and Zakharov [64] describes the shape of the data less well.

In Figure 11.3 the ratio is shown in four $Q^2$ intervals. For $x_L < 0.55$ the data samples exhibit a similar fall with $x_L$. Above $x_L = 0.55$, the steepness of the rise of the data with $x_L$ increases with $Q^2$.

In Fig. 11.4 the data samples are split into four different $x_L$ intervals and the ratio $1/\rho$ is shown as a function of $Q^2$. In order to enlarge the $Q^2$ range a point at lower $Q^2$ from previously published ZEUS results [10] has been added to this figure. There is a clearly changing $Q^2$ dependence for different $x_L$ ranges. A dashed line is drawn at the value of 1, which would be expected if vertex factorization holds.

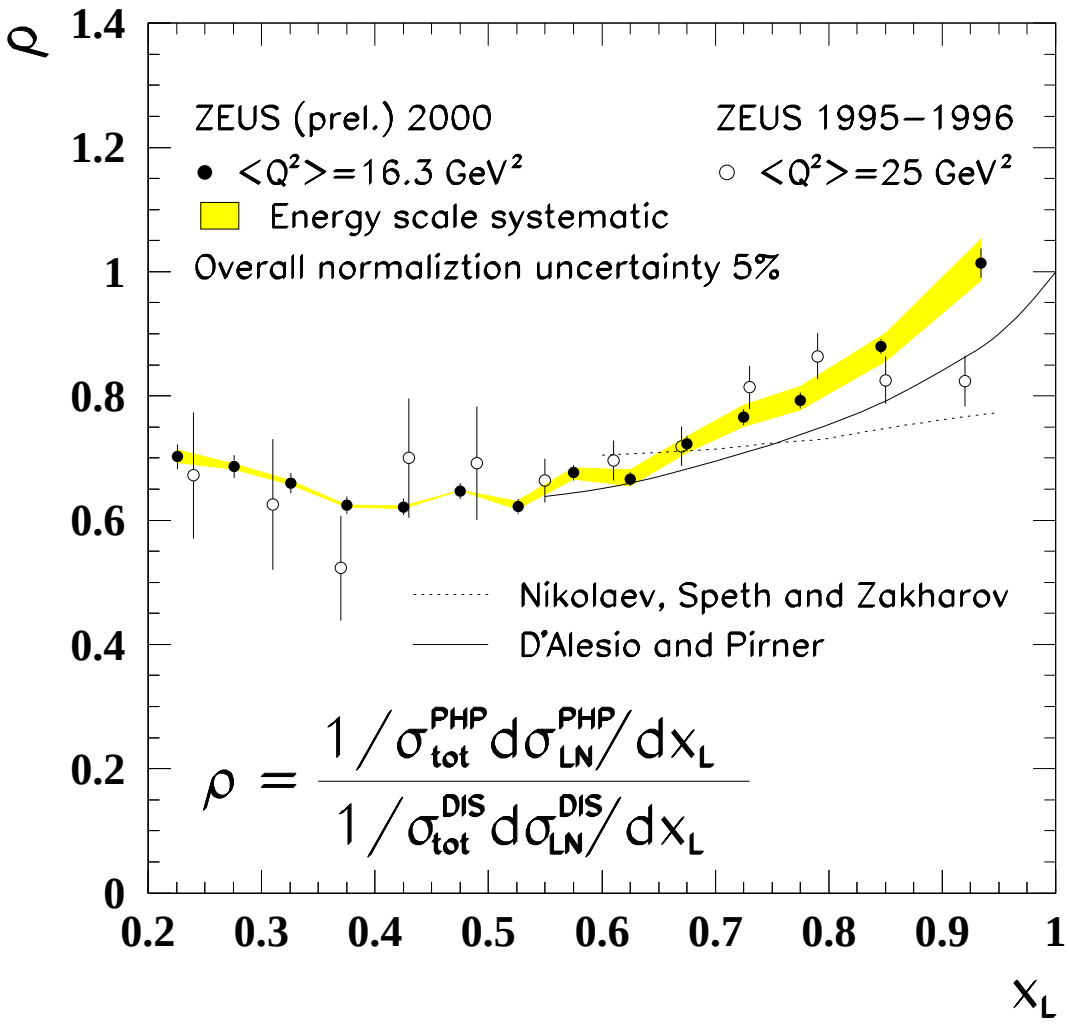


Figure 11.2: The ratio of PHP/DIS versus $x_L$, normalized as described in the text. The solid and dotted curves are the in this thesis discussed absorption models. The vertical error bars display the statistical uncertainty. the shaded band represents the the systematic uncertainty from 0.03 energy scale uncertainty. There is an overall scale uncertainty of 0.05 on this ratio.

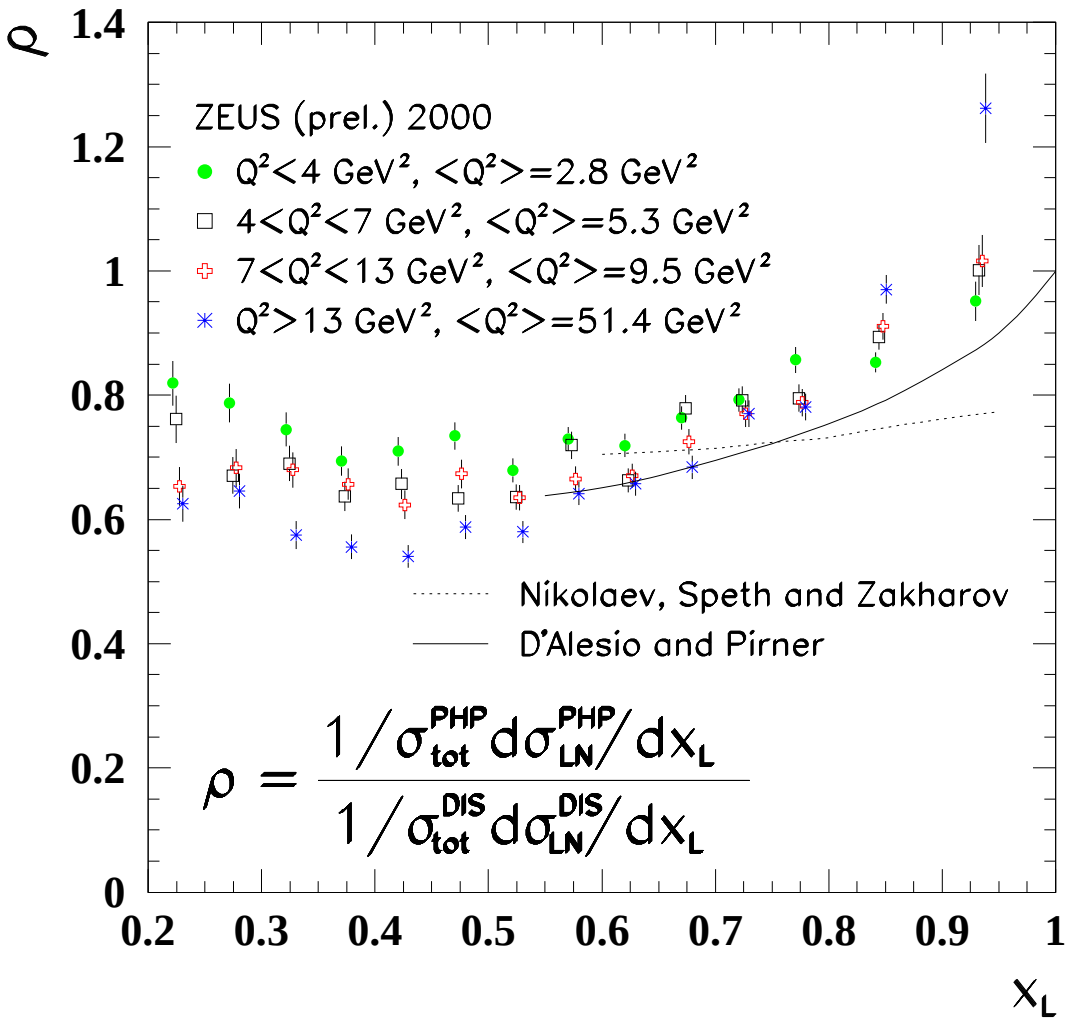


Figure 11.3: The ratio $1/\rho$ versus $x_L$ in four different $Q^2$ ranges. The vertical error bars display the statistical uncertainties . For clarity there is a slight horizontal offset for each point. Solid and dotted curves are again the two discussed absorption models.

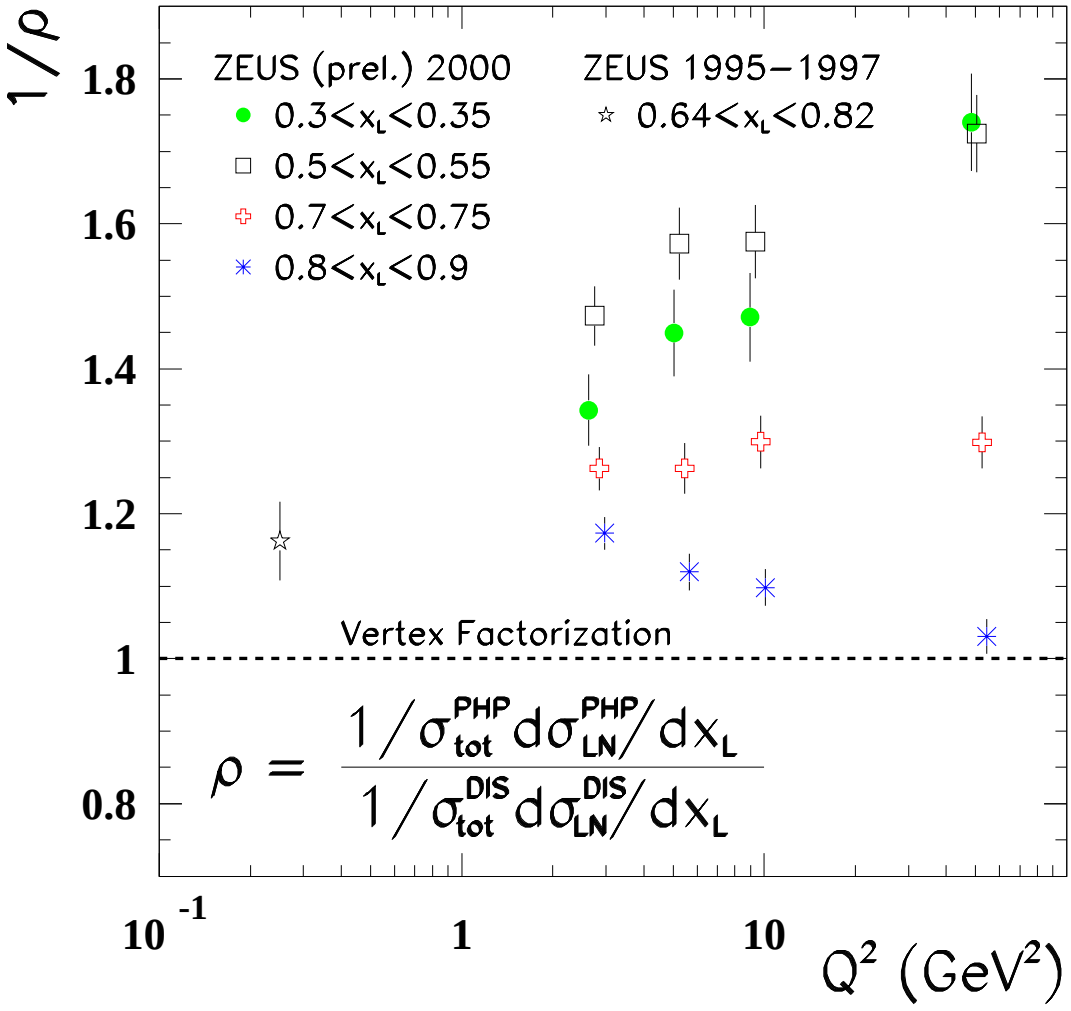


Figure 11.4: The ratio of DIS/PHP versus $Q^2$ in four different $x_L$ ranges, again normalized as described in the text. The vertical error bars show the statistical uncertainties. For clarity each set of points has again a slight horizontal offset. The dashed line at unity is the expectation of vertex factorization.

Both the fact that the ratio is not in agreement with 1 and the changing dependence of the ratio on $Q^2$ as a function of $x_L$ indicate a violation of vertex factorization. The results are only in fair agreement with expectations derived from absorption models.

It should be noted that the above comparison to theory is subject to an important caveat. The quantity derived in the theoretical calculations is

$$\frac{d\sigma_a^{PHP}}{d\sigma_{na}^{PHP}} \Big/ \frac{d\sigma_a^{DIS}}{d\sigma_{na}^{DIS}} \tag{11.2}$$

where $d\sigma_a^{PHP}$, $d\sigma_a^{DIS}$ are the semi-inclusive cross sections calculated with the absorptive processes and $d\sigma_{na}^{PHP}$ and $d\sigma_{na}^{DIS}$ are the cross sections calculated without taking absorption into account. The quantity is not observable. The quantity measured by the experiment is

$$\frac{d\sigma_a^{PHP}}{\sigma^{PHP}} \Big/ \frac{d\sigma_a^{DIS}}{\sigma^{DIS}}, \tag{11.3}$$

where $\sigma^{PHP}$ and $\sigma^{DIS}$ are the cross sections for the inclusive process $ep \to eX$. The theory assumes

$$d\sigma_{na} = f\sigma', \tag{11.4}$$

for photoproduction and DIS, where f is a flux factor and $\sigma'$ is the cross section for the process $e\pi \to eX$. Combining (11.2) and (11.4),

$$\frac{d\sigma_a^{PHP}}{d\sigma_{na}^{PHP}} \Big/ \frac{d\sigma_a^{DIS}}{d\sigma_{na}^{DIS}} = \frac{d\sigma_a^{PHP}}{\sigma'^{PHP}} \Big/ \frac{d\sigma_a^{DIS}}{\sigma'^{DIS}}. \tag{11.5}$$

Therefore, provided

$$\frac{\sigma^{PHP}}{\sigma^{DIS}} = \frac{\sigma'^{PHP}}{\sigma'^{DIS}}, \tag{11.6}$$

it follows that the theoretical expression (11.2) equals the experimental expression (11.3), that is

$$\frac{d\sigma_a^{PHP}}{d\sigma_{na}^{PHP}} \Big/ \frac{d\sigma_a^{DIS}}{d\sigma_{na}^{DIS}} = \frac{d\sigma_a^{PHP}}{\sigma^{PHP}} \Big/ \frac{d\sigma_a^{DIS}}{\sigma^{DIS}}. \tag{11.7}$$

The assumption (11.6) seems reasonable, but it has not been measured.

# Chapter 12

# Summary

The study of the production process of leading neutrons in $ep$ collisions at HERA provides an interesting exploration of short range ("hard") and long range ("soft") aspects of the strong interaction. Pion exchange can be studied and the structure of the pion probed. Absorptive effects can give information on the size of the photon and of the proton viewed as a $\pi$-neutron system. Various aspects of leading neutron production are addressed in this thesis, in particular by studying the neutron angular distributions. This has been made possible by the 1998 upgrade to the ZEUS Forward Neutron Calorimeter (FNC) with a position measuring hodoscope. The angular distributions of leading neutrons are measured in Deep Inelastic Scattering (DIS), Photoproduction (PHP) and Photoproduced dijet (PHP-dijet) event samples.

Crucial to the measurement is the determination of the zero degree point of the neutron distribution. The procedure is complicated by the fact that even within the geometric acceptance of the FNC there is inactive material which partly shadows the leading neutrons. The mapping of the inactive material and the determination of the zero degree point with three different methods agree within the errors of the methods. The angular distributions were measured as a function of the momentum transfer squared to the neutron, $p_T^2$, and parameterized as an exponential form $e^{-bp_T^2}$ for the neutron energy fraction $x_L$. All three data sets show similar values of b, rising from $\approx 5\,\mathrm{GeV}^{-2}$ at low $x_L$ to $\approx 11\,\mathrm{GeV}^{-2}$ at high $x_L$. The PHP (a soft process) b values are $\approx 1\,\mathrm{GeV}^{-2}$ higher than those of DIS and PHP-dijet (both hard processes).

The values of b as a function of $x_L$ are compared to leading proton measurements in DIS and PHP. While the leading neutron b values have a strong dependence on $x_L$, the leading protons have just a weak dependence on $x_L$, in agreement with expectations that the production mechanism for leading protons is not dominated by One-Pion-Exchange (OPE) as is the case for leading neutrons, but rather by a combination of several exchange mechanisms.

The b values are compared to theoretical OPE predictions for neutron production. None of the models with the parameters preferred by the authors is in very good agreement with the data. The data can reject some models and constrain the choice of parameters in others.

The $x_L$ distributions of neutrons for PHP in bins of $t$ are approximately power laws in $(1-x_L)$, that is $dN/dx_L \propto (1-x_L)^{a(t)}$. For each $t$ bin the power $a(t)$ was obtained by a linear least squares fit to the observed distribution. To within the experimental uncertainties the powers lie on a linear trajectory in $t$:

$$a(t) = 1.08 \pm 0.08^{+0.40}_{-0.42} - (2.78 \pm 0.32^{+0.31}_{-0.41}\ \mathrm{GeV}^{-2})t.$$

This leads directly to the following result using OPE:

$$\alpha_{I\!P}(0) = 1.08 \pm 0.08^{+0.40}_{-0.42}$$

and

$$\alpha'_{\pi} = 1.39 \pm 0.16^{+0.16}_{-0.21}\,\mathrm{GeV}^{-2}.$$

These values are in good agreement with the expectations of 1.08 for $\alpha_{I\!P}(0)$, the value of the pomeron trajectory at $t = 0\,\mathrm{GeV}$, and of $\approx 1.0$ for the slope of the pion trajectory. This measurement at a center-of-momentum energy of 318 GeV in $ep$ scattering is consistent with earlier determinations in hadronic experiments with lower center-of-momentum energies.

Neutron absorption is studied by measuring the ratio of the $x_L$ distributions of neutrons at different $Q^2$ and comparing to theoretical predictions. The calculation of

Nikolaev, Speth and Zakharov [64] does not describe the data well, whereas the prediction of D'Alesio and Pirner [58] is better, although still only in moderate agreement with the data.

The $Q^2$ dependence of the ratio is investigated separately for different $x_L$ intervals. The ratio differs from unity and has a $Q^2$ dependence varying with $x_L$, indicating that vertex factorization is violated, i.e., the proton-pion-neutron vertex cannot be treated separately from the interaction of the probing particle with the exchanged pion.

These studies contribute significantly to the knowledge of leading baryon production in high energy interactions, and the data will help focus further theoretical understanding in this complex field of study. The measurements cast new light on the understanding of the pion and further the understanding of the proton. It is an important input to the theory of QCD and its evolution, which is not yet able to predict the structure of hadrons and mesons completely. These studies are of importance to Regge theory and its role as a non-perturbative theory to explain the leading neutron production mechanism.

In the outlook to future experiments with more statistics, leading neutron production in charged current events is of interest, since flavor sensitivity can be tested. The $W^-$ exchanged in $e^-p \to \nu nX$ can couple to both the valence and the sea quarks. It couples to the valence quarks at high $x_\pi = x_{BJ}/(1-x_L)$, the momentum fraction carried by the pion, which means neutrons at high $x_L$. The $W^+$ exchanged in $e^+p \to \bar{\nu} nX$ can only couple to sea quarks, which have low $x_\pi$, meaning neutrons at low $x_L$. So in $e^+p \to \bar{\nu} nX$ there should be more neutrons at lower $x_L$ than in $e^-p \to \nu nX$. The actual $x_L$ distributions in the two cases would test parameterizations of the pion structure function.

Another interesting study would be to look at rapidity gap events with leading neutrons. HERA results [78] suggest that large rapidity gap events, which comprise only about 10% of the total cross section, are predominantly due to pomeron exhange. The

rap gap fraction is only about half this for neutron tagged events. OPE will make a contribution because the exchanged pion can scatter diffractively via a pomeron exchange with a resulting rapidity gap. A study with higher statistics would enhance the knowledge of the forward structure in deep inelastic diffraction.

For the next few years HERA will run with five times the previous luminosity, so further studies such as those just mentioned will be possible.

# Appendix A

# Glossary

**BCAL :** Barrel Calorimeter.

**BMUON :** Barrel Muon chambers.

**CAL :** Calorimeter.

**CC :** Charged Current.

**CTD :** Central Tracking Detector.

**DAQ :** Data Acquisition System.

**DESY :** Deutsches Elektronen Synchrotron, the German national high energy physics laboratory located in Hamburg, Germany.

**DIS :** Deep Inelastic Scattering.

**DST :** Data Summary Tape.

**EMC :** Electromagnetic section of the CAL.

**EVB :** Event Builder.

**FCAL :** Forward Calorimeter.

**FLT :** First Level Trigger.

**FNC :** Forward Neutron Calorimeter.

**FND :** Forward Neutron Detector.

**FNT :** Forward Neutron Tracker.

**GeV :** Giga electron Volt.

**GFLT :** Global First Level Trigger.

**HAC :** Hadronic section of the CAL.

**hadron :** Strongly interacting particle.

**HERA :** Hadron Elektron Ring Anlage.

**LPS :** Leading Proton Spectrometer

**lepton :** $e$, $\mu$, $\tau$, or neutrinos of these particles

**LUMIE :** Part of the luminosity monitor for measuring Electrons from the Bethe-Heitler process.

**LUMIG :** Part of the luminosity monitor for measuring Gammas from the Bethe-Heitler process.

**MC :** Monte Carlo.

**MeV :** Mega electron Volt.

**NC :** Neutral Current.

**PHP :** Photoproduction

**PMT :** Photomultiplier Tube.

**QCD :** Quantum Chromodynamics.

**RCAL :** Rear Calorimeter.

**RMUON :** Rear Muon chambers.

**RTD :** Rear Tracking Detector.

**SLT :** Second Level Trigger.

**TLT :** Third Level Trigger.

**UCAL :** Uranium Calorimeter.

**ZEUS :** High energy physics experiment located at DESY, Hamburg, Germany

# Bibliography


[1] R. Zoller. *Z. Phys.*, C53:443, 1992.

[2] H. Holtmann et. al. *Phys.Lett.*, B338:363, 1994.

[3] B. Kopeliovich. *Z.Phys.*, C73:125, 1996.

[4] M. Brkić. *A Study of Leading Neutrons in $\gamma p$ Collisions at HERA*. PhD thesis, University of Toronto, 1996.

[5] ZEUS Collab, M. Derrick et. al. *Phys. Lett.*, B384:388, 1995.

[6] J. Engler et al. Measurement of inclusive neutron spectra at ISR. *Nucl.Phys.*, B84:70–82, 1975.

[7] M. Khazad. *Measurement of Dijet Cross Sections with a Leading Neutron in Photoproduction at HERA*. PhD thesis, York University, 1999.

[8] ZEUS Collab, J. Breitweg et al. *Nucl. Phys.*, B596:3, 2000.

[9] C.-P. Fagerstroem. *Leading Neutron Production In Deep Inelastic Scattering at HERA*. PhD thesis, University of Toronto, 1999.

[10] ZEUS Collab, J. Breitweg et al. *Nucl. Phys*, B637:3, 2002.

[11] ZEUS Collab. The ZEUS Detector. *Technical Report*, 1986.

[12] ZEUS Collab. The ZEUS Detector. *Status Report*, 1993.

[13] N. Harnew et. al. *Nucl. Instrum. Methods*, A279:290, 1989.

[14] B. Foster et. al. *Nucl. Phys. (Proc. Suppl.)*, 32:181, 1993.

[15] B. Foster et. al. *Nucl. Instrum. Methods*, A338:254, 1994.

[16] J. Breitweg and others. Measurement of high-$q^2$ charged-current $e^+p$ deep inelastic scattering cross sections at HERA. *Eur. Phys. J.*, C12:411, 2000.

[17] Paul de Jong. *The Measurement of the Hadronic Energy Flow and Jet Production with the ZEUS Calorimeter in Deep Inelastic Scattering Events at HERA*. PhD thesis, University of Amsterdam, 1993.

[18] M. Derrick et. al. *Nucl. Inst. Methods*, A309:77, 1991.

[19] A. Bernstein et. al. *Nucl. Inst. Methods*, A336:254, 1994.

[20] A. Caldwell et. al. *Nucl. Instrum. Methods*, A321:356, 1992.

[21] H. Bethe and W. Heitler. *Proc. Roy. Soc.*, A146:83, 1934.

[22] M. Derrick et. al. *Z. Phys.*, C63:391, 1994.

[23] LPS Group. Lps alignement, calibration and reconstruction for 1994 data. *ZN-96-59*.

[24] K.O'Shaughnessy et al. *NIM*, A342:260, 1994.

[25] TYVEK is a product of DuPont. DuPont Corporate Information Center Chestnut Run Plaza 705/GS38 Wilmington, DE 19880-0705, USA.

[26] S. Bhadra et al. Design and test of a forward neutron calorimeter for the zeus experiment. *Nucl. Instr. and Meth.*, A394:121, 1997.

[27] U. Behrens et al. Quality control and calibration of the zeus forward and rear calorimeters with $60^{co}$ sources.

[28] R.P. Feynman. *Phys. Rev. Lett.*, 23:1415, 1969.

[29] J.D. Bjorken. *Phys. Rev.*, 179:1547, 1969.

[30] E.D. Bloom et al. *Phys.Rev.Lett*, 23:930, 1969.

[31] T. Eichten. *Phys. Lett.*, B46:274, 1973.

[32] TASSO Collab., R. Bradelik et al. *Phys. Lett.*, B86:243, 1979.

[33] J.C. Collins, D.E. Soper and G. Sterman. Perturbative Quantum Chromodynamics.

[34] T. Regge. *Nuovo Cimento Ser.*, 14:10, 1959.

[35] M. L. Perl. High Energy Hadron Physics. John Wiley and Sons, Toronto.

[36] P. D. B. Collins. Regge Theory and High Energy Physics. Cambridge University Press, New York.

[37] Donald M. Perkins. Introduction to High Energy Physics. Addison-Wesley Publishing, Don Mills, Ontario, first edition.

[38] R. J. Eden. *Rep. Prog. Phys.*, 34:995, 1971.

[39] M. Bishari. *Phys.Lett.*, B38:510, 1972.

[40] I. Potashnikova B. Kopeliovich, B. Povh. *Zeit. Phys.*, C73:125, 1996.

[41] N.N. Nikolaev, W. Schaefer, A. Szczurek, J. Speth. Do the E886 Drell Yan data change our picture of the chiral structure of the nucleon? *hep-ph/9812266*, 1998.

[42] B. Robinson et al. *Phys. Rev. Lett.*, 34:1475, 1975.

[43] R.D. Field and G.C. Fox. *Nucl. Phys.*, B80:367, 1974.

[44] NA27 Collab., M. Aguilar-Benitez et al. *Zeit. Phys.*, C50:405, 1991.

[45] E666/NuSea Collab., E.A. Hawker et al. *Phys. Rev. Lett.*, 80:3715, 1998.

[46] L.L. Frankfurt, L. Maniewicz , M.I. Strikman. *Zeit. Phys.*, A334:343, 1989.

[47] K. Golec-Biernat, J. Kwiecinski, A. Szczurek. *Phys. Rev.*, D56:3955, 1997.

[48] M. Przybycien, A. Szczurek, G. Ingelman. *Zeit. Phys.*, C74:509, 1997.

[49] A.W. Thomas. *Phys. Lett.*, B126:97, 1983.

[50] A. Szczurek, N.N. Nikolaev, J. Speth. *Phys. Lett.*, B428:383, 1998.

[51] A.S. Ito et al. *Phys. Rev.*, D23:604, 1981.

[52] CCFR Collab., C. Foudas et al. Neutrino production of charm at FNAL E-744.

[53] H. Holtmann, A. Szczurek, J. Speth. *Nucl. Phys*, A569:631, 1996.

[54] A. Donnachie, P.V. Landshoff. *Phys. Lett.*, B296:227, 1992.

[55] W. Melnitchouk, J.Speth, A.W. Thomas. *Phys.Rev.*, D59:14033, 1998.

[56] A. Szczurek, N.N. Nikolaev, J. Speth. *Phys.Lett.*, B428:383, 1998.

[57] G. Wolf. *DESY 94-022.*

[58] U. D'Alesio and H.J. Pirner. Target fragmentation in $pp$, $ep$ and $\gamma p$ collisions at high energies. *EPJ*, A7:109, 2000.

[59] V.R. Zoller. *Z. Phys.*, C53:443, 1992.

[60] A. Holtmann, A. Szczurek and J. Speth. *Nucl. Phys.*, A596:631, 1996.

[61] W. Koepf, L.L. Frankfurt and M. Strikman. *Phys. Rev.*, D53:2586, 1996.

[62] G. Holzwarth and R. Machleidt. *Phys. Rev.*, C55:1088, 1997.

[63] R.J. Fries and A. Schafer. *hep-ph/9801358.*

[64] N.N. Nikolaev, J. Speth and B.G. Zakharov. Absorptive corrections to the one pion exchange and measurability of the small-$x$ pion structure function at HERA. *KFA-IKP(TH)-1997-17*, 1997.

[65] A.H. Mueller. *Phys. Rev.*, D2:2963, 1970.

[66] K.J.M. Moriarty, J.H. Tabor and A. Ungkichanukit. *Phys. Rev.*, D16:130, 1977.

[67] B.G. Zakharov, V.N. Sergeev. *Sov. J. Nucl. Phys.*, 28:689, 1978.

[68] A.G. Azcarate. *Phys. Rev.*, D17:3022, 1978.

[69] B.G. Zakharov, V.N. Sergeev. *Sov. J. Nucl. Phys.*, 38:801, 1983.

[70] F. Jacquet and A. Blondel. Proceedings of the Study for an *ep* facility in Europe. *DESY-79/48*, 1979.

[71] S. Bentvelsen, J. Engelen and P. Kooijman. Proceedings of Workshop on Physics at HERA. 1991.

[72] The ZEUS Collaboration, J. Breitweg et al. Measurement of Dijet Cross Sections for Events with a Leading Neutron in Photoproduction at HERA. *NP*, B596:3, 2000.

[73] Garry Levman. *Private Comunications.*

[74] ZEUS Collab, S. Chekanov et al. *Nucl. Phys*, B658:3, 2003.

[75] H. Abramowicz et al. *Nucl. Phys.*, B166:62, 1980.

[76] H. Hanlon et al. *Phys. Rev.*, D20:20, 1979.

[77] W. Flauger, F. Monnig. *Nucl. Phys.*, B109:347, 1976.

[78] ZEUS Collab, M. Derrick et al. *Phys.Lett.*, B315:481, 1993.